UPC **CTTC**

On the development of Direct Numerical Simulations for falling films.

Centre Tecnològic de Transferència de Calor
Departament de Màquines i Motors Tèrmics
Universitat Politècnica de Catalunya

Nicolás Valle Marchante
Doctoral Thesis

On the development of Direct Numerical Simulations for falling films.

Nicolás Valle Marchante

TESI DOCTORAL

presentada al

Departament de Màquines i Motors Tèrmics
E.S.E.I.A.A.T.
Universitat Politècnica de Catalunya

per a l'obtenció del grau de

Doctor per la Universitat Politècnica de Catalunya

Terrassa, December 2020

On the development of Direct Numerical Simulations for falling films.

Nicolás Valle Marchante

Directors de la Tesi

Dr. Jesús Castro González

Dr. Assensi Oliva Llena

Tutor

Dr. Francesc Xavier Trias Miquel

Tribunal Qualificador

Prof. Dr. Arthur E. P. Veldman
Rijksuniversiteit Groningen

Univ.-Prof. Dr.-Ing. Markus Klein
Universität der Bundeswehr München

Dr. F. Javier Rey Martínez
Universidad de Valladolid

Dr. José Fernández Seara
Universidade de Vigo

Dr. Carlos D. Pérez-Segarra
Universitat Politècnica de Catalunya

A la Glòria.

Al Nicolau.

Contents

Agraïments **xi**

Acknowledgements **xv**

Abstract **xix**

1 Introduction **1**
1.1 Motivation . . . 1
1.2 Background . . . 3
1.2.1 High Performance Computing . . . 3
1.2.2 Discrete Calculus . . . 4
1.2.3 Multiphase flows . . . 5
1.3 Outline of this thesis . . . 7
References . . . 7

2 An energy-preserving level set method for multiphase flows. **15**
2.1 Introduction . . . 15
2.2 Topological model . . . 17
2.2.1 Mesh . . . 18
2.2.2 Interface . . . 19
2.3 Symmetry-preserving discretization of single-phase flows . . . 22
2.3.1 Energy conservation . . . 23
2.3.2 Symmetry-preserving discretization . . . 23
2.3.3 Analysis . . . 25
2.4 Energy-preserving discretization of multiphase flows . . . 25
2.4.1 Energy conservation . . . 26
2.4.2 Energy-preserving discretization . . . 27
2.4.3 Analysis . . . 30
2.5 Results . . . 31
2.5.1 Cylindrical column . . . 32
2.5.2 Oscillating ellipsoidal column . . . 38
2.5.3 Capillary wave . . . 44
2.6 Concluding Remarks . . . 49
2.7 Acknowledgements . . . 50
References . . . 51

3 Vectorial implementation of flux limiters for HPC. 57
3.1 Introduction . . . 58
3.2 Algebraic Topology . . . 59
3.3 Flux Limiters . . . 63
3.3.1 Algebraic Formulation . . . 64
3.3.2 Algebraic Implementation . . . 68
3.3.3 Comparison with the stencil-based approach . . . 70
3.4 Numerical Results . . . 72
3.5 Conclusions and Future Work . . . 74
3.6 Acknowledgments . . . 75
References . . . 75

4 DNS methods for vertical falling films. 79
4.1 Introduction . . . 80
4.2 Mathematical model . . . 82
4.3 Numerical Method . . . 84
4.3.1 Regularization . . . 84
4.3.2 Discretization . . . 88
4.3.3 Integration . . . 91
4.4 Preliminary results . . . 94
4.5 Conclusions . . . 100
References . . . 100

5 Conclusions 107
References . . . 110

A Inner products 111

B Modified Nusselt Flat Film scaling 113
References . . . 115

Agraïments

Si bé les tesis només tenen un autor, el cert és que hi ha hagut moltes persones que durant el temps de desenvolupament d'aquesta, m'han ajudat a dur-la a terme. Aquest és un reconeixement a totes elles.

Voldria començar agraint la tasca del professor Assensi Oliva al capdavant del Centre Tecnològic de Transferència de Calor (CTTC). Ja abans de començar la meva tesi doctoral, mentre estudiava Enginyeria Industrial, vaig sospitar que era una professor diferent. Recordo amb especial estima el dia que es va presentar a la classe de Transferència de Calor i, després d'una breu salutació, va fer uns gargots a la pissarra, va agafar una cadira, va asseure's de cara a nosaltres i, amb un braç repenjat al respatller, ens va explicar que allò eren les equacions de Navier-Stokes per, acte seguit, començar una apassionada divagació sobre la seva rellevància científica i tecnològica, les dificultats de la seva resolució i l'ús de mètodes numèrics per tal de resoldre-les. La seva energia es contagiava i he de reconèixer que, encara que no començaria el doctorat fins a uns anys més tard, aquell dia em va convèncer. A part d'haver sembrat en mi, i en molts altres, la llavor de la recerca, li he d'agrair molt especialment el seu suport durant la meva estada al CTTC com a estudiant de doctorat. Així mateix, i molt especialment, vull agrair la seva empenta per crear un grup de treball ambiciós i ple de talents. D'aquest aquest grup, que ha estat com una altra família per a mi en els últims anys, voldria agrair especialment a les següents persones:

Al meu director de tesi, el Jesús Castro, per haver-me introduït al món de la refrigeració per absorció. Per haver aterrat els reptes tecnològics que presenta aquesta tècnica de refrigeració en problemes especifics, plantejant reptes estimulants, i per donar-me suport i escalf en els moments més complicats de la tesi.

El Francesc Xavier Trias, el meu tutor de tesi, mereix una especial consideració, i es que hi ha companys de feina que acaben esdevenint amics, i ell és un d'ells. Amb ell ja vaig veure que ens entendríem des del primer moment, car ambdós compartíem una curiositat per les mateixes coses i una pulsió Cruyffista per fer fàcil allò difícil. Forjat en incomptables discussions al voltant d'una tassa de cafè, o, depenent de les hores, una cervesa, a ell li dec el mètode i el rigor matemàtic que he intentat seguir en aquest treball. Més enllà de l'admiració científica que li tinc, a en Xavi també li agraeixo la seva mentoria durant tota la tesi i haver esdevingut un referent professional.

A en Xavier Àlvarez li vull agrair haver estat un fantàstic company de sala, així com el seu suport en tots aquells temes relacionats amb la computació d'alt rendiment (HPC, per les seves sigles en anglès). Tot i tractar temes de tesi tant diferents, crec que la nostra relació mostra l'ambient pluridisciplinar que regna al CTTC.

A l'Aleix Bàez li vull agrair les moltes i bones discussions acadèmiques (i potser encara més les no acadèmiques) que vam mantenir durant el temps que hem coincidit al CTTC. L'Aleix ha estat durant tot aquest temps una font de sabiesa inesgotable i li estic molt agraït per això. A l'Arnau Pont, l'Enrique Gutiérrez, l'Eduard Bartrons, l'Imanol Aizpurua, el Jesús Ruano, la Nina Morozova, el Dani Martínez i el Joan Calafell, amb els que hem compartit el temps de la tesi doctoral i sempre han estat disposats a ajudar o debatre el que calgués. A l'Octavi Pavón, el Ramiro Alba, el Jordi Chiva i el Guillem Colomer, per tot el seu suport tècnic durant tot aquest temps. La seva capacitat de donar resposta a qualsevol problema que es pogués plantejar ha estat imprescindible. Voldria també recordar la figura del Manuel Ordoño, per el seu particular caràcter però també per la seva camaraderia en els meus inicis al taller. No voldria oblidar als membres de la Termosecta, l'equip de futbol del laboratori, per haver proporcionat una estona de pausa setmanal per gaudir junts del futbol. Voldria tancar els agraïments als companys del CTTC mencionant tots els companys que han passat pel laboratori, així com els que m'han precedit, per haver contribuït al prestigi del CTTC i a crear un ambient de treball distés i agradable.

De la meva estada a Universitat de Groningen, als Països Baixos, voldria començar agraint al professor Roel Verstappen per haver-me acollit al seu grup de treball. El temps que vaig poder compartir allà amb ell em va ajudar molt a consolidar i incorporar nous conceptes al meu treball. A part del professor Verstappen, també vull agrair al professor emèrit Arthur Veldmann, per tenir sempre la porta oberta a enraonar en qualsevol moment sobre la nostra recerca i per ser un exemple d'una vida dedicada a la recerca. A en Ronald Remmerswaal i en Paolo Cifani, pels debats que vam tenir durant la meva estada acompanyats d'un stroopwaffel. A en Maurtis Silvis per haver-me ajudat a instal·lar-me a Groningen i ensenyar-me la ciutat i a la resta dels companys de per fer la meva estada no només profitosa, sinó també molt agradable.

De l'estada a TU Delft vull agrair especialment al professor Marc Gerritsma, per haver-me introduït al mètode dels elements espectrals i per tenir sempre plena disposició per aclarir qualsevol dubte que em pogués sorgir al respecte. També al Varun Jain i el Yi Zhang, per haver compartit amb mi el seu temps i haver-me ajudat durant la meva estada.

Tot això no hagués estat possible sense el finançament econòmic de la beca FI-AGAUR de la Generalitat de Catalunya sota el contracte 2017FIB00616.

Finalment, vull fer una especial menció a tota la meva família i amics pels seu suport durant tot aquests anys.

A la meva àvia Palmira, per encomanar-me la seva passió pels llibres i per saber que et poden portar lluny.

Al meu pare, per el dia que, sent un marrec, em va donar una espremedora de taronges espatllada dient-me: "Nico, desmunta-la i a veure si tu la pots arreglar". Tot

i que l'espremedora no tenia solució, és el primer record que tinc d'obrir alguna cosa i preguntar-me "com funciona, això?". També per aquells diumenges que anàvem a rentar el cotxe amb el meu germà al túnel de rentat. De vegades aparcava en un carreró abans d'arribar a casa i obria el capó per netejar el motor del cotxe. Jo m'hi atansava i li preguntava com funcionava tot allò: que on estava el clàxon o què feia aquella corretja. Gràcies a les seves respostes (i la seva paciència) vaig decidir dedicar-me a respondre a la pregunta "com funciona, això?".

A la Glòria Oliete, la meva dona, no tinc paraules per agraïr el seu incodicional suport durant tot aquest temps, per haver estat sempre al meu costat i haver confiant en mi en tot moment. Per haver-me tret del laboratori el cap de setmana i fer que la vida fos molt més que la recerca. Per haver decidit compartir la vida junts i formar part de les aventures que hem viscut, que estem vivint i que ens queden per viure.

Finalment, al Nicolau Valle i Oliete, que ha arribat a les acaballes d'aquesta tesi, però que m'ha donat l'energia, l'alegria i la determinació necessària per acabar-la.

A totes elles, gràcies de tot cor.

Acknowledgements

While thesis have only one author, there has been many people that have played a role in my way here. This is in appreciation to all of them.

I would like to start by acknowledging the task of Assensi Oliva as head of the Centre Tecnològic de Transferència de Calor (CTTC). Even before I started my PhD, while studying mechanical engineering, I could notice that he was different from other professors. I remember with special fondess the day he showed up at a Heat Transfer lecture and, after a brief introduction, scribbled on the blackboard, grabbed a chair, sat down in front of us, and, with one arm resting on its back, he told us that these were the Navier-Stokes equations and began a passionate digression on their scientific and technological relevance, the difficulties arising from trying to solve them, and the use of numerical methods to do it. His energy was contagious and I have to admit that, even though I would not start my PhD until a few years later, that day he got me. Aside from sowing in me, and many others, the seed of research, I must especially thank him for his support during my time at the CTTC as a PhD student. Also, and most especially, I want to thank his determination to create an ambitious and talented working group. I would like thank the following people from the lab, which has been like another family for me in the last years:

To my advisor, Jesús Castro, for introducing me to the world of absorption cooling. For bringing the technological challenges presented by this cooling technique down to specific problems, posing stimulating challenges, and for his support and warmth in the most complicated moments of the thesis.

To Francesc Xavier Trias, my thesis tutor, deserves special consideration. There are co-workers who end up becoming friends, and he is one of them. We had a connection from the very first moment, because we both shared a curiosity for the same things and a Cruyffist drive to get the easy out of the the difficult. Forged into countless discussions over a cup of coffee, or, depending on the hours, a beer, I owe him the method and mathematical rigor I have tried to follow in this work. In addition to the scientific admiration I have for him, I also thank Xavi for his mentoring throughout his thesis and for becoming a professional reference.

I would like to thank Xavier Àlvarez for being a great roommate, as well as his support in all those issues related to High Performance Computing. Despite dealing with so many different thesis topics, I think our relationship shows the multidisciplinary atmosphere that prevails at the CTTC.

I want to thank Aleix Bàez for the many good academic discussions (and perhaps even more so the non-academic ones) that we had during the time we met at the CTTC. Aleix has been an endless source of wisdom all this time and I am very grateful to him for that. To Arnau Pont, Enrique Gutiérrez, Eduard Bartrons,

Imanol Aizpurua, Jesús Ruano, Nina Morozova, Dani Martínez and Joan Calafell, with whom we shared the time of the doctoral thesis and have always been willing to help or discuss whatever was needed. To Octavi Pavón, Ramiro Alba, Jordi Chiva and Guillem Colomer, for their technical support during all this time. Their ability to solve any problems that may arise has been essential. I would also like to remember Manuel Ordoño, for his particular character but also for his fellowship during my early days in the workshop. I do not want to forget the members of Termosecta, the lab's football team, for providing a weekly break to enjoy football together.

I would like to finish my acknowledgements to the CTTC by mentioning all its present and former members, for their contribution to the prestige of the center and for creating a relaxed and pleasant work environment.

From my stay at the University of Groningen, in the Netherlands, I would like to thank Professor Roel Verstappen for taking me in his research group. The time I shared with him helped me a lot in strenghten and incorporating new concepts into my work. Aside from Professor Verstappen, I would also like to thank Emeritus Professor Arthur Veldmann, for his willingness to discuss at any time about our research and for being an example of a life dedicated to research. To Ronald Remmerswaal and Paolo Cifani, for the discussions we had during my stay accompanied by a stroopwaffel. To Maurtis Silvis for helping me settle in Groningen and showing me the city and the rest of the lab mates to make my stay not only profitable, but also very enjoyable.

From my time at TU Delft, I would like to thank Professor Marc Gerritsma for introducing me to the method of spectral elements and for always being willing to clarify any doubts that may arise in this regard. Also to Varun Jain and Yi Zhang, for sharing their time with me and helping me during my stage.

All this would not have been possible without the financial financing of the FI-AGAUR grant from the Generalitat de Catalunya under contract 2017FIB00616.

Finally, I want to make a special mention to all my family and friends for their support throughout these years.

To my grandmother Palmira, for pass her passion for books on to me and for knowing that they can take you far.

To my father, for the day when, being a kid, he gave me a broken orange juicer, saying to me: "Nico, take it apart and see if you can fix it." Although the juicer had no solution, it's the first memory I have of opening something and asking myself "how does it work?". Also for those Sundays we used to go to the car wash with my brother. Sometimes he would park in an alley before getting home and open the hood to clean the car's engine. I used to ask him how it all worked: where the horn was or what that strap was doing. Thanks to his answers (and his patience) I decided to dedicate myself to answering "how does it work".

To Glòria Oliete, my wife, I have no words to thank her for her unwavering sup-

port all this time, for always being by my side and trusting me at all times. For taking me out of the lab over the weekend and making life so much more than research. For having decided to share life together and be part of the adventures to come.

Finally, to Nicolau Valle i Oliete, who has arrived by the end of this thesis, but who has given me the energy, joy and determination to finish it.

To all of them, thank you from the bottom of my heart.

Abstract

Multiphase flows present a rich variety of physical instabilities, which may turn into a set of interesting techonological features. In the particular case of vertical fallings films, these features provide with short residence times, good heat transfer coefficients and low pressure drop, which make them good candidates for the heat and mass transfer demands of absorption chillers, amid many other thermal and chemical applications.

The adoption of a discrete vector calculus approach for the numerical treatment of such flows present with two synergistic advantages: on the one side, the deployment of numerical methods into massive supercomputing systems is favourished while, on the the other hand, the mathematical properties of the resulting algorithms can be conveniently revealed.

Similarly to the symmtery-preserving ideas in place for the Direct Numerical Simulation of single phase turbulent flows, and equipped with the aforementioned mathematical machinery, a novel physics-compatible discretization for the numerical computation of multiphase flows is presented which, similarly to its single phase counterpart, preserves energy at the discrete level.

The new method introduces the first variation of area in the context of a the Conservative Level Set method to match the kinetic energy contribution due to the capillary forces with the potential energy variation due to the interface deformation. This requires for the re-formulation of the high ressolution scheme used for the transport of the marker function from an algebraic perspective, which ultimatelly yields to the design of a novel curvature interpolator. In addition, the adoption of a consistent mass and momentum discretization is presented in terms of the aforementioned algebraic approach, resulting in the anounced energy-preserving level set method.

xx

1

Introduction

1.1 Motivation

Falling films are a family of particularly interesting multiphase flows. They are characterized by narrow sheets of a viscous fluid flowing down a plate. This kind of flows are present in many industrial applications and natural phenomena and exhibit many particularities of mathematical, physical and technological interest.

The tears of wine phenomena, steam condensing on and falling down the bathroom mirror or he formation of rivulets down a pouring glass are everyday examples of film flows.

Its captivating beauty caught the attention of many scientist at the turn of the 20th century, who made a significant effort in understanding such flow dynamics.

C.G.M. Marangoni was the first to provide a rigorous explanation to the tears of wine phenomena [1] and also theorized on the onset of a convective flow due to a surface tension gradient, a phenomena named after him [2].

In 1916 E.K.W. Nusselt provided with a laminar solution to the vapor condensation over a flat film [3]. This is nowadays know as the Nusselt flat film solution and provides the most fundamental solution to this particular flow.

Later on, P.L. Kapitza, deprived of his Nobel Prize awarded investigations on low temperature physics, performed outstanding experiments on falling film instabilities and introduced innovative ideas that set the ground for further development of the topic [1, 4].

The charm of such flows is matched by their complexity: on top of the already know Navier-Stokes equations, a free boundary problem is in place along which the capillary force produce a stress discontinuity. This results in a number of know instabilities even at low Reynolds numbers.

Falling films exhibit a range of favorable features which make them ideal candidates for its use in thermal and chemical equipment [1]. Most remarkably, falling

films present a small thermal resistance, low pressure drop and a large contact area per unit flow [5], which makes them ideal candidates for heat transfer applications where small temperature differences are available/required (e.g., for heat sensitive alimentary products [6]). They are also good candidates for process involving mass transfer as well (i.e. concentrating liquids) such as gas absorbers [7] and in general for heat exchangers with low available pressure drop, like the ones required for negative pressure absorption chillers [8].

In addition, its inherently unstable nature can be exploited to enhance its heat and mass transfer characteristics by means of both passive [9] or active techniques [10].

In the context of combined heat and mass transfer, falling films play a key role in the design of absorption chillers, which fit within the mission of the CTTC and are an active branch of research at CTTC [8, 11–15].

Absorption chillers obey a standard refrigeration cycle where the typical reciprocating compressor is replaced by a thermochemical one. Just like regular compressors, thermochemical compressors' mission is to take the saturated vapor produced at the evaporator and to deliver superheated vapour to the condenser. This way the evaporator keeps working at a low partial pressure, while the energy enclosed into the superheated gas can be released trough the condenser.

The thermochemical compressor splits its task in a three stages cycle. First, it absorbs the saturated vapor coming from the evaporator into a working liquid solution, which is consequently diluted. This occurs at the absorber, after which the entire cycle is named. Secondly a pump pressurizes the diluted solution and sends it to the generator, where, finally, heat is applied to separate the working liquid solution into a liquid and a vapor fraction. While the vapor fraction is delivered to the condenser, where the regular refrigeration cycle continues, the liquid fraction is flown to the absorber, where the cycle starts again [16].

This cycle presents several advantages, namely *i)* mechanical compression is performed over a liquid, which is much more efficient that over a gas; and *ii)* it uses heat as the main energy stream.

CTTC has long experience in the design and construction of absorption chiller prototypes. The center has targeted the development of air-cooled, low capacity, $H_2O - LiBr$ absorption chillers because of its lower installation cost and use of non-toxic working refrigerant/absorbent pair [12–15]. The requirements for low electric consumption on such air-cooled absorption chillers discourages the use of externally driven (i.e., an auxiliary pump) absorbers, and thus leads naturally to a gravity driven solution. Falling films arise then as a suitable choice under such design constrains [12].

Critical to the absorber performance assessment are its heat and mass transfer characteristics. As mentioned above, those can be intensified by promoting the films' inherent hydrodynamic instabilities [1]. While the use of active techniques, most no-

tably vibration, is well-known for falling film absorbers [10, 17], the use of passive techniques, most notably surfactants, is widespread and well reported in the literature [18–22]

Despite its popularity in absorption systems, the mechanics of such complex flows are not yet fully understood [22, 23]. As a matter of fact, even the plain hydrodynamic instabilities are far from a complete understanding [1]. In the particular case of a $H_2O - LiBr$ absorber, typical operating conditions include an absorption pressure of $1kPa$ in order to enable vaporization slightly above $10°C$. This implies a density ratio $\rho_{liq}/\rho_{vap} \approx 10^5$ and a viscosity ratio $\mu_{liq}/\mu_{vap} \approx 10^6$, which pose major challenges for the accurate numerical simulation of such flows.

This extreme operating conditions are not only difficult to attain in an experimental setup [24], but also present a rich variety of other physical effects, which complicate the isolation of the thermal dynamics from the fluid ones [25]. In this context, the use of numerical techniques to gain trustworthy insights into the complicated dynamics of the falling films appears as a promising technique [26, 27].

1.2 Background

This section aims at establishing the current state of the art of the technologies relative to this thesis. It also intends to establish the influences present at CTTC at the time of writing.

1.2.1 High Performance Computing

The development of increasingly powerful architectures has fostered the setup of ever growing massive parallel supercomputers. While the computational capacity has boomed in recent years, it also has the power consumption of such systems. In the context of the exascale challenge, novel architectures have proven useful at reducing the power consumption of such systems [28], increasing the heterogeneity of computational systems.

The increasing number of architectures comes with increasing programming, debugging and maintaining complexity. In addition, the diversity of architectures that the scientific computing community is witnessing produces a need for portability between different architectures [29].

In this context, a modular approach for the development of scientific computing software can benefit from simplified development, maintainability and portability. A typical example is the BLAS standard [30], where a minimalist set of basic operations, known as kernels, has been devised in order to simplify the computational codes.

In this regard, CTTC has advocated for and algebraic approach to the development of scientific computing software [29]. As Oyarzun et al. [31] showed, 90% of

the operations of a typical Direct Numerical Simulation (DNS) of an incompressible flow algorithm can be cast into three simple instructions, namely: *i)* Sparse Matrix-Vector product (SpMV), *ii)* generalized vector addition (axpy) and *iii)* dot product (DOT). This reduces enormously the effort required for portability, allowing to execute the exact same algorithm in different architectures [31–33] and eventually enabling petascale simulations [34, 35].

1.2.2 Discrete Calculus

As mentioned previously, the adoption of an algebraic approach to scientific computing in the context of massive parallel architectures may present several computational advantages.

Notwithstanding, a reformulation of the algorithms is required, most of the times, to convey the stream of operations that define a scientific computing code into the aforementioned basic algebraic operations.

The adoption of a fully algebraic formulation to the development of numerical algorithms may benefit as well from a higher degree of abstraction. Actually, this was also done by Verstappen and Veldmann [36, 37] and Trias et al. [38], even when the computations where performed without the explicit construction of the algebraic operators.

Long term advocated by Tonti [39, 40], mimetic methods [41] aims at preserving the inherent mathematical structures of space in order to ensure high-quality simulations. Depending on the mathematical backbone chosen for this approximation, this approach has also been called Discrete Exterior Calculus [42, 43] and Discrete Vector Calculus [44, 45] as well. In addition to fluid dynamics [46–49], mimetic methods have also been adopted in, and actually have also been enriched from, different contexts such as electromagnetism [50, 51]. Conversely, the adoption by Verstappen and Veldmann of symmetry preserving [36, 37] discretizations for turbulent flows focused on preserving physical quantities of interest by enforcing the mathematical structure of the space. Both approaches ensure a physics-compatible simulation and can be seen as two sides of the same coin.

Beyond its appealing mathematical niceness, symmetry preserving / mimetic schemes provide with enhanced numerical stability and reliability. As it will be seen in the coming section, the adoption of high fidelity numerical simulation is of paramount importance for the development of closure models for multiphase flows. In the context of bigger and, regardless all efforts, more expensive numerical simulations, the adoption of high fidelity numerical techniques is a smart strategy to increase the value of the numerical simulation.

This later approach has been long used at CTTC and adopted as a solid research line. Following this spirit, several developments on the simulation of turbulent flows have been conducted by Trias et al. [38, 52–54].

1.2.3 Multiphase flows

While simulation of turbulent single-phase flows has attained a considerable degree of maturity, the accurate modeling of multiphase flows is not as developed.

It is notwithstanding understandable given the mathematical and physical complexity that needs to be account for on top of the already challenging fluid dynamics, as the diversity of coexisting numerical techniques illustrates.

Analogous to the use of Reynolds-Averaged Navier-Stokes (RANS) averaging of the flow properties is possible in multiphase systems considering, the different physical properties of each phase [55]. Considering the evolution of mass, momentum and energy averaged equations for each phase, results into so-called two-fluid models [55, 56].

Nonetheless, averaged models require of closure relations that account for effects depending on the interface topology (e.g., surface tension, phase change), which is inherently overlooked in such models and its main weakness [55]. Such relations can be derived for simplified flow configurations, or otherwise rely on extensive experimental validation [57].

In this context is where interface-resolved schemes come into play. Its aim is to perform high quality simulations able to capture the interface dynamics to provide insight into interfacial physics. In this regard, due to the extraordinary complexity ruling multiphase flows, the adoption of high quality, physics-compatible and reliable numerical techniques is mandatory in order to replace actual experiment with numerical ones.

While many techniques have been developed so far, we may distinguish between two big families of methods: interface capturing techniques, in which the interface is represented implicitly by some sort of marker function; and interface tracking ones, in which the interface is actually tracked down in a Lagrangian fashion. The most popular methods within each family are briefly introduced next, while further details can be found in [55].

Generally speaking, all interface capturing method deal with transporting a marker (also named "color") function indicating the presence of one phase or the other. For a detailed review on different interface-capturing methods, the reader is referred to [58].

The Volume of Fluid (VOF) method was popularized by Hirt and Nichols [59] and use the volume fraction as marker function. Particular advection schemes are required in order to enforce a sharp transport resolution of the marker [55]. While mass conservation is inherent to the method, historically it suffers in computing interface curvature, a key quantity for surface tension driven flows.

The level-set method, later introduced by Osher and Sethian [60] and subsequently by Sussman et al. [61] adopted a different approach. Instead of transporting a volume fraction, they used a distance function, as marker function. While the

method handles flawlessly topological merging and breakup of the interfaces, mass conservation is not guaranteed.

The phase-field method was introduced to multiphase flows by Anderson [62] and later by Jacqmin [63], where, resembling the actual smooth physical potential observed at the vicinity of interfaces at the molecular level, they introduced a smooth marker function.

Finally, as a compromise solution between the VOF and the level set methods, the Conservative Level Set (CLS) method was introduced by Olsson and Kreiss [64]. In their approach, a convolution of the distance function with *tanh* is introduced such that it resembles a smoothed Heaviside step function, resulting into a smooth interface method which is much closer to their cousins phase-field methods than to traditional level set ones.

While interface-capturing method present all different pros and cons, they all suffer form a very fundamental numerical pathology: the unsuitability of discrete domains to transport sharp interfaces. This issue has fostered the development of a rich variety of advection schemes.

Front-tracking methods, on the other hand, rely on explicitly tracking the interface between phases. For such a purpose, Lagrangian particles are placed at the interface and it position evolved with the underlying velocity field. Surface reconstruction is then performed by reconnecting the isolated particles.

The Immersed Boundary (IB) methods developed by Peskin [65] is intended at the resolution of fluid-structure interactions. In this case, the regions of the domain belonging to the solid phase impose artificial forces to enforce the proper flow behavior at the solid wall.

The front-tracking method proposed by Unverdi and Tryggvason [66] was the first to employ a reconstruction of the interface separating two immiscible fluids in the context of the Navier-Stokes equations [55].

While front-tracking methods achieve inherently sharp interfaces, they do so at the expenses of higher computational costs associated with geometric reconstruction. They also require special treatments when it comes to simulating coalescence and breakup processes.

The use of two-fluid models has been in place at CTTC since 2009 [67–70], while made its entrance in interface-resolved simulations in 2004 with the formulation of VOF [18,71,72] and later on in 2014 with the inclusion of CLS [73–75] techniques.

This work has been influenced by the former research performed at the CTTC in this regard and has adopted as its interface-capturing scheme the CLS proposed by Olsson and Kreiss [64] and present at the lab since 2014 [76].

1.3 Outline of this thesis

This rest of this thesis is organized as follows: in chapter 2 we build upon the single phase symmetry preserving schemes to provide with a novel energy preserving level set method suitable for tracking multiphase flows. In chapter 3 we provide with a new formulation of a flux limiter in order which is suitable for the HPC^{2}framework. Finally in chapter 4 a DNS of a falling film is presented.

References

[1] S. Kalliadasis, C. Ruyer-Quil, B. Scheid, and M. G. Velarde. *Falling Liquid Films*, volume 176. Springer, London, 2012.

[2] J. T. Davies and E. K. Rideal. *Interfacial Phenomena*. Academic Press Inc., London, 1961.

[3] V. Isachenko, V. Osipova, and A. Sukomel. *Heat Transfer*. Mir Publishers, Moscow, 2nd edition, 1974.

[4] P.L. Kapitza and S.P. Kapitza. Wave flow of thin layers of a viscous fluid. In D. Ter Haar, editor, *Collect. Pap. P.L. Kapitza*, volume 2, pages 662–708. Pergamon, 1965.

[5] Fabian Denner, Marc Pradas, Alexandros Charogiannis, Christos N. Markides, Berend G. M. van Wachem, and Serafim Kalliadasis. Self-similarity of solitary waves on inertia-dominated falling liquid films. *Phys. Rev. E*, 93(3):033121, mar 2016.

[6] A. Akesjo. *Hydrodynamics and Heat Transfer in Vertical Falling Films with Smooth and Modified Heat-Transfer Surfaces – An Experimental and Numerical Investigation*. PhD thesis, Chalmers University of Technology, 2018.

[7] Akio Miyara, Tomoki Yamamoto, Toru Iemura, and Takashi Shimada. Gas absorption by wavy falling liquid film formed on inner surface of vertical tubes. *J. Therm. Sci.*, 12(1):57–61, 2003.

[8] Jesús Castro, C. Oliet, I. Rodríguez, and A. Oliva. Comparison of the performance of falling film and bubble absorbers for air-cooled absorption systems. *Int. J. Therm. Sci.*, 48(7):1355–1366, 2009.

[9] Georg F. Dietze. Effect of wall corrugations on scalar transfer to a wavy falling liquid film. *J. Fluid Mech.*, pages 1098–1128, 2018.

[10] Hirojuki Tsuda and Horacio Perez-Blanco. An experimental study of a vibrating screen as means of absorption enhancement. *Int. J. Heat Mass Transf.*, 44(21):4087–4094, 2001.

[11] J Castro. Craft-Joule Project: Air-Cooled water LiBr cooling machine of low capacity for air conditioning (ACABMA). In *MILLENIUM Sol. FORUM 2000*, 2000.

[12] Jesus Castro Gonzalez. Simulation of heat and mass transfer phenomena in the critical elements of H2O-LiBr absorption cooling machines. Experimental validation and application to design. 2005.

[13] J. Farnós, Jesús Castro, S. Morales, E. Garcia-Rivera, A. Oliva, and D. Kizildag. Preliminary results of a 7kW single-effect small capacity pre-industrial LiBr-H2O air-cooled absorption machine. In *EuroSun*, 2014.

[14] J Farnós. *Development of a prototype demonstration of a direct air-cooled LiBr-H2O absorption cooling machine*. PhD thesis, Universitat Politècnica de Catalunya, 2019.

[15] Assensi Oliva Llena, Carlos David Pérez-Segarra, Joaquim Rigola Serrano, Jesús Castro, Carles Oliet Casasayas, Ivette Rodríguez Pérez, Oriol Lehmkul Barba, F. Xavier Trias, Roser Capdevila Paramio, Ramiro Alba Queipo, Manuel Miguel Ordoño Martínez, and Joan Farnos Baulenas. Machine for air-cooled absorption, 2020.

[16] Keith E Herold, Reinhard Radermacher, and Sanford A Klein. *Absorption chillers and heat pumps*. CRC press, 2016.

[17] H. Garih, S. Julius, J. L. Estivalezes, and G. Casalis. Vibration-induced instability of a fluid film flowing down a vertically inclined plane: Experimental and theoretical comparison. *Phys. Fluids*, 29(10):104103, 2017.

[18] J. Castro, L. Leal, C.D. Pérez-Segarra, and P. Pozo. Numerical study of the enhancement produced in absorption processes using surfactants. *Int. J. Heat Mass Transf.*, 47(14-16):3463–3476, jul 2004.

[19] N. Atsushi, N. Hidemasa, and Y. Yamaka. Absorbing solution composition and operation method of absorption type water cooler-heater, 2008.

[20] S. Kulankara and K. E. Herold. Surface tension of aqueous lithium bromide with heat/mass transfer enhancement additives: The effect of additive vapor transport. *Int. J. Refrig.*, 25(3):383–389, 2002.

[21] Sung-bum Park and Huen Lee. Heat and Mass Transfer of the New LiBr-Based Working Fluids for Absorption Heat Pump. *Society*, pages 1378–1385, 2002.

[22] Carlos Amaris, Manel Vallès, and Mahmoud Bourouis. Vapour absorption enhancement using passive techniques for absorption cooling/heating technologies: A review. *Appl. Energy*, 231(September):826–853, 2018.

[23] Jesse D. Killion and Srinivas Garimella. A critical review of models of coupled heat and mass transfer in falling-film absorption. *Int. J. Refrig.*, 24(8):755–797, 2001.

[24] E. García-Rivera, J. Castro, J. Farnós, and A. Oliva. Numerical and experimental investigation of a vertical LiBr falling film absorber considering wave regimes and in presence of mist flow. *Int. J. Therm. Sci.*, 109:342–361, 2016.

[25] E. García-Rivera. Modelling and Experimental Validation of Water Vapor Absorption by Falling Films of LiBr Aqueous Solution Under Wave Regimes Conditions and Presence of Non-Absorbable Gases.

[26] Georg F. Dietze and Reinhold Kneer. Flow separation in falling liquid films. *Front. Heat Mass Transf.*, 2(3), 2011.

[27] Georg F. Dietze, W. Rohlfs, K. Nährich, R. Kneer, and B. Scheid. Three-dimensional flow structures in laminar falling liquid films. *J. Fluid Mech.*, 743:75–123, 2014.

[28] Jack Dongarra, Pete Beckman, Terry Moore, Patrick Aerts, Giovanni Aloisio, Jean Claude Andre, David Barkai, Jean Yves Berthou, Taisuke Boku, Bertrand Braunschweig, Franck Cappello, Barbara Chapman, Xuebin Chi, Alok Choudhary, Sudip Dosanjh, Thom Dunning, Sandro Fiore, Al Geist, Bill Gropp, Robert Harrison, Mark Hereld, Michael Heroux, Adolfy Hoisie, Koh Hotta, Zhong Jin, Yutaka Ishikawa, Fred Johnson, Sanjay Kale, Richard Kenway, David Keyes, Bill Kramer, Jesus Labarta, Alain Lichnewsky, Thomas Lippert, Bob Lucas, Barney MacCabe, Satoshi Matsuoka, Paul Messina, Peter Michielse, Bernd Mohr, Matthias S. Mueller, Wolfgang E. Nagel, Hiroshi Nakashima, Michael E. Papka, Dan Reed, Mitsuhisa Sato, Ed Seidel, John Shalf, David Skinner, Marc Snir, Thomas Sterling, Rick Stevens, Fred Streitz, Bob Sugar, Shinji Sumimoto, William Tang, John Taylor, Rajeev Thakur, Anne Trefethen, Mateo Valero, Aad Van Der Steen, Jeffrey Vetter, Peg Williams, Robert Wisniewski, and Kathy Yelick. The international exascale software project roadmap. *Int. J. High Perform. Comput. Appl.*, 25(1):3–60, 2011.

[29] X. Álvarez, A. Gorobets, F. X. Trias, R. Borrell, and G. Oyarzun. HPC2—A fully-portable, algebra-based framework for heterogeneous computing. Application to CFD. *Comput. Fluids*, 173:285–292, sep 2018.

[30] L. Susan Blackford, James Demmel, Jack Dongarra, Iain Duff, Sven Hammarling, Greg Henry, Michael Heroux, Linda Kaufman, Andrew Lumsdaine, Antoine Petitet, Roldan Pozo, Karin Remington, and R. Clint Whaley. An Updated Set of Basic Linear Algebra Subprograms (BLAS). *ACM Trans. Math. Softw.*, 28(2):135–151, 2002.

[31] Guillermo Oyarzun, Ricard Borrell, Andrey Gorobets, and Assensi Oliva. Portable implementation model for CFD simulations. Application to hybrid CPU/GPU supercomputers. *Int. J. Comut. Fluid Dyn.*, 31(9):396–411, 2017.

[32] Guillermo Oyarzun. *Heterogeneous parallel algorithms for Computational Fluid Dynamics on unstructured meshes*. PhD thesis, Universitat Politècnica de Catalunya, 2015.

[33] G. Oyarzun, R. Borrell, A. Gorobets, F. Mantovani, and A. Oliva. Efficient CFD code implementation for the ARM-based Mont-Blanc architecture. *Futur. Gener. Comput. Syst.*, 79:786–796, 2018.

[34] R. Borrell, J. Chiva, O. Lehmkuhl, I. Rodríguez, and A. Oliva. Evolving Termofluids CFD Code Towards Peta-Scale Simulations. In *27th Int. Conf. Parallel Comput. Fluid Dyn.*, pages 1–8, 2015.

[35] R. Borrell, J. Chiva, O. Lehmkuhl, G. Oyarzun, I. Rodríguez, and A. Oliva. Optimising the Termofluids CFD code for petascale simulations. *Int. J. Comut. Fluid Dyn.*, 2016.

[36] R. W. C. P. Verstappen and A. E. P. Veldman. Direct numerical simulation of turbulence at lower costs. *J. Eng. Math.*, (c):143–159, 1997.

[37] R. W. C. P. Verstappen and A. E. P. Veldman. Symmetry-preserving discretization of turbulent flow. *J. Comput. Phys.*, 187(1):343–368, 2003.

[38] F. X. Trias, O. Lehmkuhl, A. Oliva, C. D. Pérez-Segarra, and R. W. C. P. Verstappen. Symmetry-preserving discretization of Navier-Stokes equations on collocated unstructured grids. *J. Comput. Phys.*, 258:246–267, 2014.

[39] Enzo Tonti. On the formal structure of physical theories, 1975.

[40] Enzo Tonti. Why starting from differential equations for computational physics? *J. Comput. Phys.*, 257(PB):1260–1290, jan 2014.

[41] Konstantin Lipnikov, Gianmarco Manzini, and Mikhail Shashkov. Mimetic finite difference method. *J. Comput. Phys.*, 257(PB):1163–1227, 2014.

[42] Anil N. Hirani. *Discrete Exterior Calculus*. PhD thesis, California Institute of Technology, may 2003.

[43] Mathieu Desbrun, Anil N. Hirani, Melvin Leok, and Jerrold E. Marsden. Discrete Exterior Calculus. pages 1–53, 2005.

[44] J. Blair Perot. Discrete Conservation Properties of Unstructured Mesh Schemes. *Annu. Rev. Fluid Mech.*, 43(1):299–318, 2011.

[45] Nicolas Robidoux and Stanly Steinberg. A discrete vector calculus in tensor grids. *Comput. Methods Appl. Math.*, 11(1):23–66, 2011.

[46] Marc Gerritsma. Structure-preserving discretization for continuum models *. 2014.

[47] Varun Jain, Yi Zhang, Artur Palha, and Marc Gerritsma. Construction and application of algebraic dual polynomial representations for finite element methods. 2017.

[48] R. Beltman, M. J.H. Anthonissen, and B. Koren. Conservative polytopal mimetic discretization of the incompressible Navier–Stokes equations. *J. Comput. Appl. Math.*, 340:443–473, 2018.

[49] René Beltman, Martijn Anthonissen, and Barry Koren. Conservative mimetic cut-cell method for incompressible Navier-Stokes equations. *Lect. Notes Comput. Sci. Eng.*, 126:1035–1043, 2019.

[50] A. Bossavit. Whitney forms: a class of finite elements for three-dimensional computations in electromagnetism. *IEE Proc. A*, 135(8):493–500, 1988.

[51] A. Bossavit. 'Generalized finite differences' in computational electromagnetics. *Prog. Electromagn. Res.*, 32:45–64, 2001.

[52] F. X. Trias, A. Gorobets, and A. Oliva. A simple approach to discretize the viscous term with spatially varying (eddy-)viscosity. *J. Comput. Phys.*, 253:405–417, 2013.

[53] F. X. Trias, A. Gorobets, and A. Oliva. Turbulent flow around a square cylinder at Reynolds number 22,000: A DNS study. *Comput. Fluids*, 123:87–98, 2015.

[54] F. X. Trias, D. Folch, A. Gorobets, and A. Oliva. Spectrally-Consistent Regularization of Navier–Stokes Equations. *J. Sci. Comput. (published online)*, 2018.

[55] Andrea Prosperetti and Grétar Tryggvason. *Computational Methods for Multiphase Flow*. Cambridge University Press, Cambridge, 2007.

[56] Mamoru Ishii and Takashi Hibiki. *Thermo-Fluid Dynamics of Two-Phase Flow*. Springer US, Boston, MA, 2006.

[57] M. Ishii and K. Mishima. Two-fluid model and hydrodynamic constitutive relations. *Nucl. Eng. Des.*, 82(2-3):107–126, 1984.

[58] S Mirjalili, S S Jain, and M S Dodd. Interface-capturing methods for two-phase flows : An overview and recent developments. *Annu. Res. Briefs*, (1):117–135, 2017.

[59] C. W. Hirt and B. D. Nichols. Volume of fluid (VOF) method for the dynamics of free boundaries. *J. Comput. Phys.*, 39(1):201–225, 1981.

[60] Stanley Osher and James A. Sethian. Fronts propagating with curvature-dependent speed: Algorithms based on Hamilton-Jacobi formulations. *J. Comput. Phys.*, 79(1):12–49, 1988.

[61] Mark Sussman. *A Level Set Approach for Computing Solutions to Incompressible Two-Phase Flow*. PhD thesis, UCLA, 1994.

[62] D. M. Anderson, G. B. McFadden, and A. A. Wheeler. Diffuse-Interface Methods in Fluid Mechanics. *Annu. Rev. Fluid Mech.*, 30(1):139–165, 1998.

[63] David Jacqmin. Calculation of Two-Phase Navier–Stokes Flows Using Phase-Field Modeling. *J. Comput. Phys.*, 155(1):96–127, oct 1999.

[64] Elin Olsson and Gunilla Kreiss. A conservative level set method for two phase flow. *J. Comput. Phys.*, 210(1):225–246, nov 2005.

[65] Charles S. Peskin. Numerical analysis of blood flow in the heart. *J. Comput. Phys.*, 25(3):220–252, 1977.

[66] Salih Ozen Unverdi and Grétar Tryggvason. A front-tracking method for viscous, incompressible, multi-fluid flows. *J. Comput. Phys.*, 100(1):25–37, 1992.

[67] S. Morales-Ruiz. *Numerical Simulation of the Thermal and Fluid Dynamics Behaviour of Liquid-Vapour Two-Phase Flow in Evaporators and Condensers*. PhD thesis, 2009.

[68] S. Morales-Ruiz, J. Rigola, C. D. Pérez-Segarra, and O. García-Valladares. Numerical analysis of two-phase flow in condensers and evaporators with special emphasis on single-phase/two-phase transition zones. *Appl. Therm. Eng.*, 29(5-6):1032–1042, 2009.

[69] G. Raush, J. Rigola, S. Morales-Ruiz, A. Oliva, and C. D. Pérez-Segarra. Analysis of the heat transfer and friction factor correlations influence in the prediction of evaporating flows inside tubes. *Int. J. Refrig.*, 32(7):1744–1755, 2009.

[70] S. Morales-Ruiz, J. Rigola, I. Rodriguez, and A. Oliva. Numerical resolution of the liquid-vapour two-phase flow by means of the two-fluid model and a pressure based method. *Int. J. Multiph. Flow*, 43:118–130, 2012.

[71] Lluís Jofre. *Numerical simulation of multiphase immiscible flow on unstructured meshes*. PhD thesis, UPC, 2014.

[72] L. Jofre, O. Lehmkuhl, Néstor Balcázar, J. Castro, J. Rigola, and A. Oliva. Conservative discretization of multiphase flow with high density ratios. *WIT Trans. Eng. Sci.*, 82:153–164, 2014.

[73] Néstor Balcázar. *Numerical simulation of Multiphase Flows: Level-Set Techniques*. PhD thesis, Universitat Politècnica de Catalunya, 2014.

[74] E. Gutiérrez, N. Balcázar, E. Bartrons, and J. Rigola. Numerical study of Taylor bubbles rising in a stagnant liquid using a level-set/moving-mesh method. *Chem. Eng. Sci.*, 164:158–177, 2017.

[75] Ahmad Amani, Néstor Balcázar, Enrique Gutiérrez, and Assensi Oliva. Numerical study of binary droplets collision in the main collision regimes. *Chem. Eng. J.*, 370(September 2018):477–498, 2019.

[76] N. Balcázar, L. Jofre, O. Lehmkuhl, J. Castro, and J. Rigola. A finite-volume/level-set method for simulating two-phase flows on unstructured grids. *Int. J. Multiph. Flow*, 64:55–72, may 2014.

2

An energy-preserving level set method for multiphase flows.

Contents of this chapter are published in:

N. Valle, F.X. Trias, J. Castro. An energy-preserving level set method for multiphase flows. *J. Comput. Phys., 400 108991*, 2020

And provided here self-contained.

Abstract. The computation of multiphase flows presents a subtle energetic equilibrium between potential (i.e., surface) and kinetic energies. The use of traditional interface-capturing schemes provides no control over such a dynamic balance. In the spirit of the well-known symmetry-preserving and mimetic schemes, whose physics-compatible discretizations rely upon preserving the underlying mathematical structures of the space, we identify the corresponding structure and propose a new discretization strategy for curvature. The new scheme ensures conservation of mechanical energy (i.e., surface plus kinetic) up to temporal integration. Inviscid numerical simulations are performed to show the robustness of such a method.

2.1 Introduction

Multiphase flows are ubiquitous in industrial applications. They are present in a rich variety of physical phenomena such as vaporization [1], atomization [2], electrohydrodynamics [3] or boiling [4], among others [5, 6].

The use of interface-capturing schemes is widespread for the computation of multiphase flows due to its computational efficiency. The Volume-Of-Fluid (VOF) by Hirt and Nichols [7], the Level Set method developed by Osher and Sethian [8] and most recently phase field methods, introduced by Anderson et al. [9], are the most popular interface capturing schemes for multiphase flows. An overview of these can be found in [10] and references therein. Despite the pros and cons that each method presents, we made our development concrete on the Conservative Level Set (CLS) initially developed by Olsson and Kreiss [11] and Olsson et al. [12] due to its good conservation properties, curvature accuracy and ease of handling topological changes. This was extended to unstructured collocated meshes in [13].

Of particular interest are the incompressible Navier-Stokes equations,

$$\rho\left(\frac{\partial \vec{u}}{\partial t} + (\vec{u}\cdot\nabla)\vec{u}\right) = \nabla\cdot\sigma \qquad\qquad \nabla\cdot\vec{u} = 0 \tag{2.1}$$

where the stress tensor σ is composed of the hydrostatic and the deviatoric ones ($\sigma = -p\mathbb{I} + \tau$). In turn, τ is defined by Stokes constitutive equation $\tau = 2\mu S$, while the strain tensor is given by $S = 1/2\left(\nabla\vec{u} + (\nabla\vec{u})^T\right)$.

The proper solution of equations (2.1) requires an appropriate decoupling of pressure and velocity. In this regard, the Fractional Step Method (FSM) [14] is an excellent tool which properly enforces the incompressibility constraint. However, the FSM results in a Poisson equation which needs to be solved, which takes most of the computational time in a typical simulation.

The construction of discrete differential operators in the seminal work of Verstappen and Veldman [15, 16] aims at preserving physical quantities of interest, namely momentum and kinetic energy, by preserving several mathematical properties at the discrete level. This merges with the conception of mimetic finite difference methods [17], where the discretization is performed to satisfy the inherent mathematical structure of the space, naturally producing a physics-compatible discretization. The present work is motivated by such an appealing idea. This has been named mimetic [17] or discrete vector calculus [18], among others [19, 20]. Mimetic methods delve into the construction of discrete differential operators by producing discrete counterparts of more fundamental mathematical concepts, making extensive use of exterior calculus. This approach results in the algebraic concatenation of elementary operators, namely matrices and vectors. Such an approach can be seen as the mathematical dual of the physics-motivated work on symmetry-preserving schemes and provides with a different point of view which fortifies the analysis of this family of methods, which have been used in both academic [21] and industrial problems [22, 23], among others. However, to our knowledge, there is no a straightforward extension of these ideas into the multiphase flow community yet.

While Direct Numerical Simulation (DNS) of single-phase flows has reached substantial maturity, multiphase flows lag behind due to its increased complexity, namely

due to two main issues: *i)* surface tension and *ii)* differences in physical properties. The former results in a dynamic equilibrium between kinetic and potential energies, which are exchanged through the capillary term. Indeed this is the reason why symmetry-preserving discretizations [15, 16], despite conserving flawlessly kinetic (and thus total) energy in single-phase flows, do not suffice to preserve mechanical energy in multiphase flows, as this transfer needs to be taken into account explicitly. The later poses challenges regarding how interpolations need to be done without breaking physical laws. In the framework of VOF, Fuster [24] proposed a discretization that preserves the (skew-)symmetries of the momentum equation, preserving kinetic energy up to surface tension, which is regarded as an energy source. However, as far as surface tension is not included into the analysis, this is a necessary, but not a sufficient condition for preserving mechanical energy. Regarding the viscous term, the work of Sussman et al. [25] provided with a conservative discretization. The interested reader is referred to [26] and references therein for a comparison between different discretization strategies for the viscous term. Despite the impressive progress done so far, none of the above have included surface tension, and thus potential energy, in the analysis of conservation of energy. It is well-known, however, that the imbalances in the surface tension term may lead to spurious currents and, eventually, unstable solutions [27]. In the framework of phase field methods, the impact of surface tension on the energy balance has been included in the works of Jacqmin [28] for the Cahn-Hilliard equation, and Jamet et al. [29] and Jamet and Misbah [30] for the Allen-Cahn formulation. This chapter aims to dig into a discretization including surface tension which, without recompression, preserves mechanical energy for level set schemes.

The rest of the chapter is arranged as follows: in Section 2.2 a glimpse of algebraic topology is provided. This sets the foundations to review the well-known symmetry-preserving discretization for single-phase flows in Section 2.3 and, inspired by this, develop a new energy-preserving scheme for multiphase flows in Section 2.4. Comparative results between current techniques and the newly developed methods are presented in Section 3.4. Finally, conclusions and future insights are outlined in Section 3.5.

2.2 Topological model

Any numerical approach requires a finite-dimensional representation of the spaces under consideration. This implies a discrete representation of the domains involved in the setup of the problem. Single-phase flows fit well into a fixed frame, typically discretized on a fixed grid. On the other hand, multiphase flows require to account for a moving interface which splits the domain at question into two regions. This interface needs to be properly discretized in order to preserve several inherent topo-

logical properties. The way this is accomplished has led to a diversity of multiphase methods [10].

2.2.1 Mesh

Let Ω be the working domain bounded by $\partial\Omega$ and assume that M is a partition of Ω into a non-overlapping mesh. An illustrative example is given in Figure 2.1. Although we stick to structured meshes for computational simplicity, the formulation presented here is independent of the mesh structure and thus can be extended into unstructured meshes. Incidence matrices are used to account for the connectivity

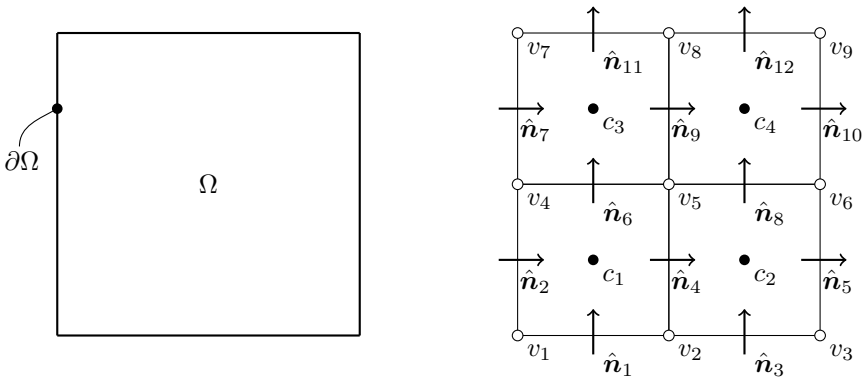

Figure 2.1: Left: Domain Ω and its boundary $\partial\Omega$. Right: Mesh M. c_i corresponds with the *ith* cell, $\hat{\boldsymbol{n}}_i$ corresponds with the normal vector to the *jth* face (i.e., f_j) and v_k corresponds with the *kth* vertex. Its incidence matrix is stated in equation (2.2).

within geometric entities. An example for $\mathsf{E_{FC}}$, the incidence matrix relating faces with cells according to the orientation of the mesh given in Figure 2.1 is shown next

$$\mathsf{E_{FC}} = \begin{array}{c} \\ c_1 \\ c_2 \\ c_3 \\ c_4 \end{array} \begin{array}{c} \begin{array}{cccccccccccc} f_1 & f_2 & f_3 & f_4 & f_5 & f_6 & f_7 & f_8 & f_9 & f_{10} & f_{11} & f_{12} \end{array} \\ \begin{pmatrix} -1 & -1 & 0 & +1 & 0 & +1 & 0 & 0 & 0 & 0 & 0 & 0 \\ 0 & 0 & -1 & -1 & +1 & 0 & 0 & +1 & -1 & 0 & 0 & 0 \\ 0 & 0 & 0 & 0 & 0 & -1 & -1 & 0 & +1 & 0 & +1 & 0 \\ 0 & 0 & 0 & 0 & 0 & 0 & 0 & -1 & -1 & +1 & 0 & +1 \end{pmatrix} \end{array} \tag{2.2}$$

They replace usual neighboring relations such as $\phi_c = \sum_{f \in c} \phi_f$ for the sum of face values related to cell c. In addition, its transpose provides with an explicit form

for $\Delta_f \phi = \phi_+ - \phi_-$ for the difference across face f, among others. Basic geometric properties such as edge lengths ($\mathsf{W_E}$), face surfaces ($\mathsf{A_F}$) and cell volumes ($\mathsf{V_C}$) are arranged as diagonal matrices. This matrix perspective presents several advantages: *i)* mesh independence , *ii)* computational simplicity and *iii)* readily accessible algebraic analysis. While we restrain ourselves from digging into the first two, the later is useful both for reviewing the classical symmetry-preserving scheme and the development of the novel technique described here. Hereafter, lowercase letters correspond with vectors, whose subscript indicates the geometric entity to which they are linked (e.g., $\mathbf{p_c}$ corresponds to pressure located at cells). Capital letters correspond with matrices, whose subscript(s) identify rows and (if different) columns (e.g. $\mathsf{E_{FC}}$ is the face-to-cell incidence matrix).

2.2.2 Interface

Interfaces imply a moving topology along the working domain, which implies a Lagrangian frame of reference. Interface tracking schemes track such a frame explicitly, at the expenses of numerical complexity [31]. On the other hand, interface capturing schemes preserve a fully Eulerian approach, by mapping quantities expressed in the Lagrangian frame back into the Eulerian one [7, 32, 33]. This results in a simpler implementation of the interface at the cost of an implicit representation. At this point we split the presentation between the techniques used to actually capture the evolution of the interface and the ones used to obtain explicit geometric information out of the implicit form.

Interface Capturing

Let's assume now that the domain Ω presents an interface at Γ, which splits Ω into Ω^+ and Ω^-. We note that the volume of a single phase Ω^+ can be defined as

$$\int_{\Omega^+} dV = \int_{\Omega} H(r) dV \tag{2.3}$$

where r corresponds with the signed shorter distance from an arbitrary point to the interface, as can be seen in Figure 2.2, while $H(r)$ is its corresponding Heaviside step function, which is valued 1 at phase Ω^+ and 0 otherwise. Note that this function is the key to map a Lagrangian frame (Ω^+) back into an Eulerian one (Ω). Specific tracking of such a quantity is the basis of the Volume of Fluid (VOF) method [7], which yields to the concept of volume fraction or, more generally, marker function. Despite being formally neat, the implementation of specific convection schemes is required, eventually requiring full geometric reconstruction, resulting in an intricate implementation. A different approach is to capture the interface with a CLS [11, 12]. This captures the interface as the isosurface of a continuous and smooth function θ.

The level set marker function, θ, results in a smoothed Heaviside step function that preserves $\int_\Omega \theta dV = \int_\Omega H(r)dV$. It is constructed as the convolution of the distance function r as follows

$$H(r) \approx \theta(r) = \frac{1}{2}\left(tanh\left(\frac{r}{2\epsilon}\right) + 1\right) \tag{2.4}$$

where ϵ corresponds with a smoothing factor. Note that $\theta(r) \to H(r)$ as $\epsilon \to 0$. Further details can be found in [13, 34].

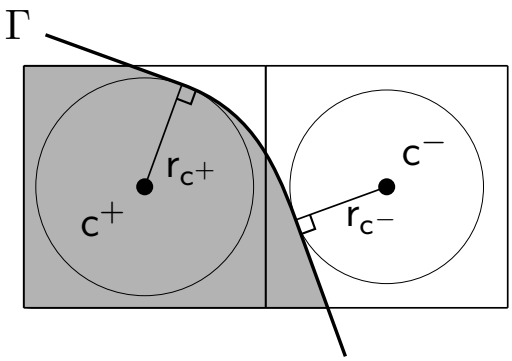

Figure 2.2: Distances $\mathbf{r}_{\mathbf{c}^\pm}$ are defined as the shorter distances of the interface to the cell. These are then normal to the interface and correspond with the minimum radius of the tangent sphere.

By imposing the conservation of the marker function, we can advect such a marker in an incompressible flow as [11–13]:

$$\frac{\partial \theta}{\partial t} + (\vec{u} \cdot \nabla)\theta = 0 \tag{2.5}$$

where particular advection schemes and recompression stages can be added in order to obtain a sharper profile. The interested reader is referred to [11, 13] and references therein.

Interface Reconstruction

Surface reconstruction may start by defining the interface normal. It is computed as [11]

$$\hat{\eta}_i = \frac{\nabla\theta}{|\nabla\theta|} \tag{2.6}$$

Which implies, by definition, that the gradient of the marker function θ is parallel to the normal. On the other hand, curvature is computed as

$$\kappa = -\nabla \cdot \hat{\eta}_i \tag{2.7}$$

Now, the surface area of Γ can be computed in any of the following forms

$$A = \int_\Gamma dA = \int_\Omega \delta(r) dV = \int_\Omega \nabla H(r) \cdot \hat{\eta}_i dV \tag{2.8}$$

where $\delta(r)$ is Dirac's delta function, which formally is the distributional derivative of the Heaviside step function. This is the basis of the celebrated continuum surface force of Brackbill et al. [35] for surface tension and, in general, of other smoothed interface methods. Regardless of the reconstruction method of choice, surface needs to satisfy first variation of area formula, which relates surface and volume variations through curvature and velocity as

$$\frac{d}{dt} \int_\Gamma dA = -\int_\Gamma \kappa \vec{u} \cdot \hat{\eta}_i dA \tag{2.9}$$

This is a fundamental identity, and the ultimate responsible of the correct conversion between kinetic and surface energy, as it will be shown in Section 2.4.1. A detailed proof of this can be found in chapter 8.4 of Frankel [36]. As an illustrative example, let us consider the surface variation of a spherical surface. If we analyze how $A = 4\pi r^2$ evolves under the action of the normal velocity, $\dot{r}$, we obtain that $\frac{dA}{dt} = 8\pi r \dot{r}$, which can be rearranged as $\frac{dA}{dt} = \frac{2}{r} A \dot{r}$, where we identify $\kappa = \frac{2}{r}$, the mean curvature of sphere. We are now going to prove that the use of a smooth marker function as in equation (4.12) leads to a consistent modeling of the interface by reconstructing surface area with its smooth counterpart $\tilde{A}$ as

$$A \overset{(2.8)}{=} \int_\Omega \nabla H(r) \cdot \hat{\eta}_i dV \overset{(4.12)}{\approx} \int_\Omega \nabla \theta \cdot \hat{\eta}_i dV \overset{(2.6)}{=} \int_\Omega |\nabla \theta| dV = \tilde{A} \tag{2.10}$$

We now show that equation (2.10) is a compatible approximation of A. In particular, we prove that equation (2.9) is still valid when we replace A by $\tilde{A}$, which is defined over the volumes and thus much more convenient to compute. First, as a preliminary stage, we take the gradient of the transport equation (2.5) in the pursue of a relation between the marker function and the smoothed surface

$$\frac{\partial \nabla \theta}{\partial t} + \nabla \left((\vec{u} \cdot \nabla) \theta \right) = 0 \tag{2.11}$$

Finally, before moving on to the announced proof, let us introduce the inner product notation $(\cdot, \cdot)$, which simplifies bi-linear integrals as $\int f g dS = (f, g)$. In addition,

concepts such as orthogonality, duality or (skew-)symmetry are naturally expressed in this framework. Further details can be found in A. With this in mind, we can proceed to approximate the left hand side of equation (2.9) via equation (2.10), to yield the following

$$\begin{aligned}\frac{d}{dt}\int_\Gamma dA \overset{(2.10)}{\approx} \frac{d\tilde{A}}{dt} &= \frac{d}{dt}\left(\nabla\theta, \hat{\eta}_i\right) = \left(\frac{d\nabla\theta}{dt}, \hat{\eta}_i\right) + \left(\nabla\theta, \frac{d\hat{\eta}_i}{dt}\right) \\ &= \left(\frac{\partial\nabla\theta}{\partial t}, \hat{\eta}_i\right) + \cancel{\left((\vec{u}\cdot\nabla)\nabla\theta, \hat{\eta}_i\right)} + \left(\nabla\theta, \frac{\partial\hat{\eta}_i}{\partial t}\right) + \cancel{\left(\nabla\theta, (\vec{u}\cdot\nabla)\hat{\eta}_i\right)} \\ &= \left(\frac{\partial\nabla\theta}{\partial t}, \hat{\eta}_i\right) + \cancel{\left(\nabla\theta, \frac{\partial\hat{\eta}_i}{\partial t}\right)} \overset{(2.11)}{=} -\left(\nabla\left(\left(\vec{u}\cdot\nabla\right)\theta\right), \hat{\eta}_i\right) \\ &= \left(\nabla\cdot\hat{\eta}_i, \vec{u}\cdot\nabla\theta\right) \quad \square\end{aligned} \tag{2.12}$$

where we exploit the skew-symmetry of the convective operator in the second row of eq. (2.12), benefit form $\frac{\partial\hat{\eta}_i}{\partial t} \perp \nabla\theta$ in the third one and the duality between gradient and divergence in the last one.

Regarding the approximation of the right hand side of equation (2.9), we can proceed by including equation (2.7) and then using equation (2.10) to move from surface to volume integrals as

$$-\int_\Gamma \kappa\vec{u}\cdot\hat{\eta}_i dA \overset{(2.7)}{=} \int_\Gamma (\nabla\cdot\hat{\eta}_i)\vec{u}\cdot\hat{\eta}_i dA \overset{(2.10)}{\approx} \left(\nabla\cdot\hat{\eta}_i, \vec{u}\cdot\nabla\theta\right) \tag{2.13}$$

We finally obtain:

$$\frac{d}{dt}\int_\Gamma d\tilde{A} = \left(\left(\vec{u}\cdot\nabla\right)\theta, \nabla\cdot\hat{\eta}_i\right) = -\int_\Gamma \kappa\vec{u}\cdot\hat{\eta}_i dA \tag{2.14}$$

We conclude that, from a continuum point of view, the use of a marker function together with the surface reconstruction strategy stated in equation (2.10) results in a consistent capture of both the interface and its geometric features, namely the first variation of area equation (2.9). Notice that this analysis is not exclusive to level sets, but rather extensible to other interface capturing schemes as far as the surface can be cast into a potential form as in equation (2.10).

2.3 Symmetry-preserving discretization of single-phase flows

In an incompressible flow, in the absence of external forces, the net balance of mechanical energy is due to the viscous term of the Navier-Stokes equation solely.

This is a relevant property for the simulation of turbulent flows, particularly for the computation of DNS. In this section, the well-known finite volume, staggered, symmetry-preserving discretization of Verstappen and Veldman [15,16] is briefly reviewed. This sets the ground of the newly developed energy-preserving scheme presented in section 2.4. Assuming constant physical properties, Navier-Stokes equations (2.1) can be rearranged to yield

$$\rho\left(\frac{\partial \vec{u}}{\partial t} + (\vec{u}\cdot\nabla)\,\vec{u}\right) = -\nabla p + \mu\nabla^2\vec{u} \qquad\qquad \nabla\cdot\vec{u} = 0 \tag{2.15}$$

which is the most common form of the Navier-Stokes equations for incompressible single-phase flows.

2.3.1 Energy conservation

The evolution of kinetic energy, $E_k = (\vec{u}, \rho\vec{u})$, in a single-phase flow is obtained by taking the inner product of $\vec{u}$ and equation (2.15), which, in the absence of external forces and without contributions from the boundaries, yields:

$$\frac{dE_k}{dt} = -\rho(\vec{u}, (\vec{u}\cdot\nabla)\vec{u}) - (\vec{u}, \nabla p) + \mu(\vec{u}, \nabla^2\vec{u}) = -\mu\left\|\nabla\vec{u}\right\|^2 \leq 0 \tag{2.16}$$

Due to the skew-symmetry of the convective operator (i.e., $(\vec{u}\cdot\nabla) = -(\vec{u}\cdot\nabla)^*$), the contribution of this term to kinetic energy is null. Duality of the gradient operator with divergence (i.e., $\nabla^* = -\nabla\cdot$) together with the incompressible constrain of the velocity ($\nabla\cdot\vec{u} = 0$) results in a null contribution of the pressure term to kinetic energy [16]. Finally, by exploiting again the duality between gradient and divergence in the viscous term, this results in a negative-definite operator, $\mu(\vec{u}, \nabla^2\vec{u}) = -\mu(\nabla\vec{u}, \nabla\vec{u}) = -\mu\left\|\nabla\vec{u}\right\|^2$, which, as expected, dumps kinetic energy.

2.3.2 Symmetry-preserving discretization

We are now going to review the well-know symmetry-preserving, second-order, staggered, finite volume discretization introduced by Verstappen and Veldman in [15], which was subsequently extended to fourth order in [16], from the algebraic perspective by means of the tools introduced in Section 2.2.1. This lays the foundation of the newly developments introduced in Section 2.4. The discretization in a staggered grid starts by defining the discrete divergence operator, D, directly from the Gauss-Ostrogradsky theorem

$$\int_\Omega \nabla\cdot\vec{u}dV = \int_{\partial\Omega} \vec{u}\cdot\vec{n}dS \approx -\mathsf{E_{FC}A_F}\mathbf{u_f} = \mathsf{M_C D}\mathbf{u_f}, \tag{2.17}$$

where $\mathsf{M_C} \in \mathbb{R}^{|C|\times|C|}$ stands for the metric of the cells, which is a diagonal matrix containing cells volume. $\mathsf{E_{FC}} \in \mathbb{R}^{|C|\times|F|}$ takes care of the appropriate sum of fluxes over the faces and $\mathsf{A_F} \in \mathbb{R}^{|F|\times|F|}$ is the diagonal matrix containing the surface of all faces. Finally $\mathbf{u_f}$ stands for the staggered velocities. We can rearrange equation (2.17) to yield

$$\mathsf{D} = -{\mathsf{M_C}}^{-1}\mathsf{E_{FC}}\mathsf{A_F}, \tag{2.18}$$

this leads to $\mathsf{D} \in \mathbb{R}^{|C|\times|F|}$, as expected for a staggered grid arrangement. Next, the discrete gradient operator, G, is constructed to preserve duality

$$(\mathbf{u_f}, \mathsf{G}\mathbf{p_c})_\mathsf{F} = -\left(\mathsf{D}\mathbf{u_f}, \mathbf{p_c}\right)_\mathsf{C}, \tag{2.19}$$

where $(\mathbf{a_c}, \mathbf{b_c})_\mathsf{C} = \mathbf{a}^\mathbf{T}{}_\mathbf{c}\mathsf{M_C}\mathbf{b_c}$ stands for the weighted inner product in the cell space, $\mathbf{C}$. It can be defined conversely for the face space, $\mathbf{F}$. Further details on inner products can be found in A.

In the context of Navier-Stokes equations, preserving this duality at the discrete level results into a null contribution of the pressure term to kinetic energy [16]

$$\mathsf{G} = -{\mathsf{M_F}}^{-1}\mathsf{D}^\mathsf{T}\mathsf{M_C} \tag{2.20}$$

where $\mathsf{M_F} \in \mathbb{R}^{|F|\times|F|}$ corresponds to the metric of the face space, and thus the definition of such a metric induces the proper construction of G. This is nothing but the definition of the staggered control volume. Notice that $\mathsf{G} \in \mathbb{R}^{|F|\times|C|}$. Again, this locates gradients at faces, as expected for a staggered discretization. $\mathsf{M_F}$ is defined as

$$\mathsf{M_F} = \Delta\mathbf{x_F}\mathsf{A_F} \tag{2.21}$$

Note that $\Delta\mathbf{x_F} \in \mathbb{R}^{|F|\times|F|}$ is the diagonal arrangement of the distance between cell centers across the face, while $\mathsf{A_F} \in \mathbb{R}^{|F|\times|F|}$ is also diagonal and contains face surfaces. The final form of G results in

$$\mathsf{G} = (\Delta\mathbf{x_F})^{-1}\mathsf{E_{CF}} \tag{2.22}$$

where the standard second-order approximation of the gradient arises naturally from the definition of the staggered control volume (i.e., one induces the other).

By concatenation, the discretization of the scalar Laplacian operator, L, the essential element of the FSM, can be defined as follows

$$\int_\Omega \nabla^2 p dV \approx \mathsf{M_C}\mathsf{L}\mathbf{p_c} = \mathsf{M_C}\mathsf{D}\mathsf{G}\mathbf{p_c} \tag{2.23}$$

As expected, $\mathsf{L} \in \mathbb{R}^{|C|\times|C|}$. We can expand the final integrated form of the discrete Laplacian as

$$\mathsf{M_C}\mathsf{L} = -\mathsf{E_{FC}}\mathsf{A_F}(\Delta\mathbf{x_F})^{-1}\mathsf{E_{CF}} \tag{2.24}$$

where such a discretization results in a negative-definite operator since $\mathsf{A_F}$ and $\Delta\mathbf{x_F}$ are positive-definite, and $\mathsf{E_{FC}} = \mathsf{E_{CF}}^\mathsf{T}$. This is the ultimate responsible of the diffusive character of viscosity in the context of Navier-Stokes equations.

Finally, the convective term can proceed as in Hicken et al. [37] in order to construct a skew-symmetric discretization. Even when dedicated convective operators may be constructed for Cartesian meshes, this provides with a more flexible approach. The idea is to construct proper face-to-cell and cell-to-face shift operators in order to exploit the collocated convective operator as

$$\mathsf{C}(\mathbf{u_f})_\mathsf{F} = \Gamma_{f\to c}\left(\mathsf{I_d} \otimes \mathsf{C}(\mathbf{u_f})_\mathsf{C}\right)\Gamma_{c\to f} \tag{2.25}$$

which guarantees skew-symmetry as far as the vector-valued shift operators are transpose (i.e., $\Gamma_{f\to c} = \Gamma_{c\to f}^\mathsf{T}$), as it is the case. Further details can be found in [15, 16, 37, 38] and references therein.

2.3.3 Analysis

By preserving (skew-)symmetries of the operators, as it was described above, the conservation of kinetic energy is guaranteed in the semi-discrete setup (i.e., up to temporal integration [39]), mimicking then the continuous behavior of the system. In particular, the semi-discretized energy balance equation reads

$$\frac{d\mathbf{E_k}}{dt} = -\left(\mathbf{u_f}, \mathsf{C}(\mathbf{u_f})_\mathsf{F}\mathbf{u_f}\right)_\mathsf{F} - \left(\mathbf{u_f}, \mathsf{G}\mathbf{p_c}\right)_\mathsf{F} + \mu\left(\mathbf{u_f}, \mathsf{L_F}\mathbf{u_f}\right)_\mathsf{F} \leq 0, \tag{2.26}$$

which is the discrete counterpart of equation (2.16). As expected, the only term contributing to kinetic energy is the viscous one, i.e., $\mu\left(\mathbf{u_f}, \mathsf{L_F}\mathbf{u_f}\right)_\mathsf{F}$, where $\mathsf{L_F}$ is the standard, negative-definite, staggered diffusive operator [16]. Note that this holds thanks to the specific construction of the operators involved and if the incompressibility constrain of velocity is satisfied at the discrete level as well (i.e., $\mathsf{D}\mathbf{u_f} = 0_c$).

2.4 Energy-preserving discretization of multiphase flows

Multiphase flows present discontinuities at the interface due to the difference of physical properties and the existence of interfacial phenomena, namely, surface tension. This section develops, on top of the symmetry-preserving scheme reviewed in the previous section, a novel energy-preserving scheme for the discretization of curvature. Curvature plays a key role in the development of discontinuities, $[\cdot]$, across the interface as

$$[\sigma]\,\hat{\eta}_i = -\gamma\kappa\hat{\eta}_i \tag{2.27}$$

where γ states for the surface tension coefficient, which we assume constant. This configures the resulting surface tension force, which acts at the interface by imposing a jump condition into the stress tensor which "pulls" the interface towards a lower free energy state. The original governing equations (2.1) can then be reformulated as

$$\rho\left(\frac{\partial \vec{u}}{\partial t} + (\vec{u}\cdot\nabla)\vec{u}\right) = -\nabla p + \nabla\cdot\tau \qquad \nabla\cdot\vec{u} = 0 \tag{2.28}$$

$$[p] = \hat{\eta}_i^T\,[\tau]\,\hat{\eta}_i - \gamma\kappa \tag{2.29}$$

where $\sigma = -p\mathbb{I} + \tau$ is split into hydrostatic and deviatoric. The discussion about the discretization of τ is out of the scope of this work, so the interested reader is refereed to Lalanne et al. [26] for a thoughtful discussion on this topic. At this point, it is assumed that τ presents a prescribed discontinuity at the interface.

2.4.1 Energy conservation

Regardless of viscous dissipation, incompressible, multiphase flows, do not preserve kinetic energy. Instead, surface ($E_p = \gamma A$) and kinetic ($E_k = (\vec{u}, \rho\vec{u})$) energy are exchanged through the pressure term [28] such that, except for the aforementioned viscous term, mechanical energy is conserved. Interface deformation results then in a transfer, through the pressure jump, between surface and kinetic energy. In order to analyze such a transfer, we start by analyzing the evolution of kinetic energy for multiphase flows, which is obtained by taking the inner product of $\vec{u}$ and, this time, the general formulation of an incompressible, Newtonian fluid given in equation (2.28)

$$\frac{dE_k}{dt} = -\left(\vec{u}, (\rho\vec{u}\cdot\nabla)\,\vec{u}\right) - (\vec{u}, \nabla p) + (\vec{u}, \nabla\cdot\tau) \tag{2.30}$$

As stated in Section 2.3.1, the skew-symmetry of the convective term results in a null contribution to kinetic energy, while the stress term includes an extra contribution due to the discontinuity at the interface stated in equation (2.27).

$$-(\vec{u}, \nabla p) + (\vec{u}, \nabla\cdot\tau) = (\nabla\cdot\vec{u}, p) - (\nabla\vec{u}, \tau) - \int_\Gamma [p]\,\vec{u}\cdot\hat{\eta}_i dS + \int_\Gamma [\tau]\,\vec{u}\cdot\hat{\eta}_i dS \tag{2.31}$$

Further details on the treatment of discontinuities within the inner product can be found in A.

Next, by considering an incompressible flow ($\nabla\cdot\vec{u} = 0$), taking the pressure jump as stated in equation (2.29) and splitting $\nabla\vec{u}$ into symmetric (S) and skew-

symmetric (W) parts we obtain

$$\begin{aligned}\frac{dE_k}{dt} &= -\left(\vec{u}, \nabla p\right) + \left(\vec{u}, \nabla \cdot \tau\right) = -\left(\nabla \vec{u}, \tau\right) - \int_\Gamma \vec{u}\,[p]\,\hat{\eta}_i dA + \int_\Gamma \vec{u}\,[\tau]\,\hat{\eta}_i dA \\ &= -\left(\nabla \vec{u}, \tau\right) + \gamma \int_\Gamma \kappa \vec{u} \cdot \hat{\eta}_i dA \\ &= -\left(S + W, 2\mu S\right) + \gamma \int_\Gamma \kappa \vec{u} \cdot \hat{\eta}_i dA \\ &= -2\left(S, \mu S\right) + \gamma \int_\Gamma \kappa \vec{u} \cdot \hat{\eta}_i dA \\ &= -2\left\|\sqrt{\mu} S\right\|^2 + \gamma \int_\Gamma \kappa \vec{u} \cdot \hat{\eta}_i dA \quad \square \end{aligned} \tag{2.32}$$

As expected, viscosity results in a negative contribution to kinetic energy, whereas surface tension can take any sign depending on whether the interface is expanding or contracting.

On the other hand, the evolution of surface energy is related to the evolution of the interfacial area. By considering Helmholtz's free energy [40]

$$dF = \gamma dA, \tag{2.33}$$

and plugging it in equation (2.9), we state that

$$\frac{dE_p}{dt} = \int_\Gamma \frac{d}{dt} dF = \gamma \int_\Gamma \frac{d}{dt} dA = -\gamma \int_\Gamma \kappa \vec{u} \cdot \hat{\eta}_i dA \tag{2.34}$$

Finally, performing a global balance of energy by combining equations (2.32) and (2.34), we obtain

$$\frac{dE_m}{dt} = \frac{dE_k}{dt} + \frac{dE_p}{dt} = -2\left\|\sqrt{\mu} S\right\|^2 \tag{2.35}$$

As expected, surface tension does not play a role in the dissipation of energy, but rather produce a dynamic exchange between kinetic and surface ones of magnitude $\gamma \int_\Gamma \kappa \vec{u} \cdot \hat{\eta}_i dA$.

2.4.2 Energy-preserving discretization

In the same spirit that symmetry-preserving methods aim at ensuring a null contribution of both pressure and convective terms in equation (2.16) at the discrete level, the task in a multiphase flow simulation adds to the requirements to preserve the proper transfer between kinetic and potential energies as

$$\frac{d\mathbf{E_m}}{dt} = \frac{d\mathbf{E_k}}{dt} + \frac{d\mathbf{E_p}}{dt} \tag{2.36}$$

Namely, if symmetry-preserving schemes were constructed to satisfy at a discrete level equation (2.19), energy-preserving methods also satisfy the discrete version of equation (2.9) in order to properly capture energetic exchanges between kinetic and surface energies. This requires the reformulation of the convective term for variable density flows to preserve skew-symmetry, as proposed by Rozema et al. [41], which however is out of the scope of this work. Nonetheless, the transfer between kinetic and surface energy occurs trough the surface tension term as

$$\frac{d}{dt}\left(\mathsf{G}\theta_{\mathbf{c}}, \hat{\mathbf{n}}_{\mathbf{f}}\right)_{\mathsf{F}} = -\left(\mathsf{U}\mathsf{G}\theta_{\mathbf{c}}, \mathbf{k}_{\mathbf{f}}\right)_{\mathsf{F}} \tag{2.37}$$

where $\mathsf{U} = \mathsf{diag}(\mathbf{u}_{\mathbf{f}}) \in \mathbb{R}^{|F|\times|F|}$ is the diagonal arrangement of face velocities, $\theta_{\mathbf{c}} \in \mathbb{R}^{|C|}$ is the cell-centered marker function vector and $\mathbf{k}_{\mathbf{f}} \in \mathbb{R}^{|F|}$ is the staggered curvature vector. We consider the advection of the marker function in terms of the discretized equation (2.5)

$$\frac{d\theta_{\mathbf{c}}}{dt} = -\mathsf{C}(\mathbf{u}_{\mathbf{f}})_{\mathsf{C}}\theta_{\mathbf{c}} \tag{2.38}$$

where $\mathsf{C}(\mathbf{u}_{\mathbf{f}})_{\mathsf{C}} \in \mathbb{R}^{|C|\times|C|}$ stands for the convective term of the marker function. It may usually include a high-resolution scheme, as we shall see later, but so far we consider it as a single operator. We disregard the role of recompression stages in time derivatives but rather consider them as correction steps, which is discussed later on this section. As previously exposed for the continuum case, we can proceed by constructing the discrete counterpart of equation (2.14) as

$$\left(\mathsf{G}\frac{d\theta_{\mathbf{c}}}{dt}, \hat{\mathbf{n}}_{\mathbf{f}}\right)_{\mathsf{F}} = -\left(\mathsf{U}\mathsf{G}\theta_{\mathbf{c}}, \mathsf{Y}\mathsf{D}\hat{\mathbf{n}}_{\mathbf{f}}\right)_{\mathsf{F}} \tag{2.39}$$

where a new shift operator, $\mathsf{Y} \in \mathbb{R}^{|F|\times|C|}$, is introduced in order to map the curvature from cells to faces. Exploiting the duality of the discrete gradient and divergence operators, equation (2.19), we obtain

$$-\left(\frac{d\theta_{\mathbf{c}}}{dt}, \mathsf{D}\hat{\mathbf{n}}_{\mathbf{f}}\right)_{\mathsf{C}} = -\left(\mathsf{U}\mathsf{G}\theta_{\mathbf{c}}, \mathsf{Y}\mathsf{D}\hat{\mathbf{n}}_{\mathbf{f}}\right)_{\mathsf{F}} \tag{2.40}$$

By subsequently expanding the inner products, we obtain

$$-\left(\frac{d\theta_{\mathbf{c}}}{dt}\right)^{\mathsf{T}}\mathsf{M}_{\mathsf{C}}\mathsf{D}\hat{\mathbf{n}}_{\mathbf{f}} = -\left(\mathsf{U}\mathsf{G}\theta_{\mathbf{c}}\right)^{\mathsf{T}}\mathsf{M}_{\mathsf{F}}\mathsf{Y}\mathsf{D}\hat{\mathbf{n}}_{\mathbf{f}} \quad \forall\hat{\mathbf{n}}_{\mathbf{f}} \tag{2.41}$$

which must hold regardless of the interface normal, $\hat{\mathbf{n}}_{\mathbf{f}}$, and consequently independently of the cell-centered curvature, $\mathsf{D}\hat{\mathbf{n}}_{\mathbf{f}}$. This implies that

$$-\left(\frac{d\theta_{\mathbf{c}}}{dt}\right)^{\mathsf{T}}\mathsf{M}_{\mathsf{C}} = -\left(\mathsf{U}\mathsf{G}\theta_{\mathbf{c}}\right)^{\mathsf{T}}\mathsf{M}_{\mathsf{F}}\mathsf{Y} \tag{2.42}$$

must hold at any time, while releasing a degree of freedom regarding the definition of the normal. We can now plug equation (2.38) in for the time derivative and expand the transpose terms

$$-\left(\frac{d\theta_{\mathbf{c}}}{dt}\right)^{\mathsf{T}} \mathsf{M_C} = \left(\mathsf{C}(\mathbf{u_f})_{\mathsf{C}}\theta_{\mathbf{c}}\right)^{\mathsf{T}} \mathsf{M_C} = \theta_{\mathbf{c}}{}^{\mathsf{T}}\mathsf{C}(\mathbf{u_f})_{\mathsf{C}}^{\mathsf{T}}\mathsf{M_C} = -\theta_{\mathbf{c}}{}^{\mathsf{T}}\mathsf{G}^{\mathsf{T}}\mathsf{U}^{\mathsf{T}}\mathsf{M_F}\mathsf{Y} \quad \forall\theta_{\mathbf{c}} \tag{2.43}$$

which should hold for any $\theta_{\mathbf{c}}$. This leads to

$$\mathsf{C}(\mathbf{u_f})_{\mathsf{C}}^{\mathsf{T}}\mathsf{M_C} = -\mathsf{G}^{\mathsf{T}}\mathsf{U}^{\mathsf{T}}\mathsf{M_F}\mathsf{Y} \tag{2.44}$$

where, exploiting the diagonal arrangement of both U and $\mathsf{M_F}$ to cast $\mathsf{G}^{\mathsf{T}}\mathsf{U}^{\mathsf{T}}\mathsf{M_F}$ into $\mathsf{G}^{\mathsf{T}}\mathsf{M_F}\mathsf{U}$, we can use equation (2.20) to obtain the final condition as

$$-\left(\mathsf{M_C}\mathsf{C}(\mathbf{u_f})_{\mathsf{C}}\right)^{T} = \mathsf{M_C}\mathsf{D}\mathsf{U}\mathsf{Y} \tag{2.45}$$

From where we can infer that the convective scheme of the marker function determines the curvature shift operator. This identity guarantees that energy transfers are balanced and thus total mechanical energy, $\mathbf{E_m}$, is preserved up to temporal integration, in the same way that kinetic energy, $\mathbf{E_k}$, is preserved in the symmetry-preserving discretization presented in Section 2.3.2 for the single-phase case.

Regarding the construction of $\mathsf{C}(\mathbf{u_f})_{\mathsf{C}}$, any high-resolution scheme can be embedded into the algebraic form $\mathsf{C}(\mathbf{u_f})_{\mathsf{C}} = \mathsf{D}\mathsf{U}\Psi$, where $\Psi \in \mathbb{R}^{|F|\times|C|}$ is the actual high-resolution cell-to-face interpolator. For the CLS, this typically corresponds with SUPERBEE [11]. We can split Ψ as $\Psi = \Pi + \Lambda$ [42], to produce

$$\mathsf{C}(\mathbf{u_f})_{\mathsf{C}} = \mathsf{D}\mathsf{U}\left(\Pi + \Lambda\right) \tag{2.46}$$

This represents the symmetric ($\mathsf{D}\mathsf{U}\Pi$) and skew-symmetric ($\mathsf{D}\mathsf{U}\Lambda$) components of $\mathsf{C}(\mathbf{u_f})_{\mathsf{C}}$. The extension to VOF schemes, nicely summarized by Patel et al. [43], requires a previous casting of the advection scheme into the same framework introduced in [42]. Plugging equation (2.46) into equation (2.45) results in the final form of the dedicated cell-to-face interpolation for curvature

$$\mathsf{Y} = \Pi - \Lambda \tag{2.47}$$

which guarantees a proper potential and kinetic energy transfer. An illustrative example can be seen in Figure 2.3. In short, any upwind-like component used for the advection of $\theta_{\mathbf{c}}$ turns into a downwind-like component for the interpolation of $\mathbf{k_f}$. This can be compared with the second-order midpoint rule used by Olsson and Kreiss where $\mathsf{Y} = \Pi$ [11].

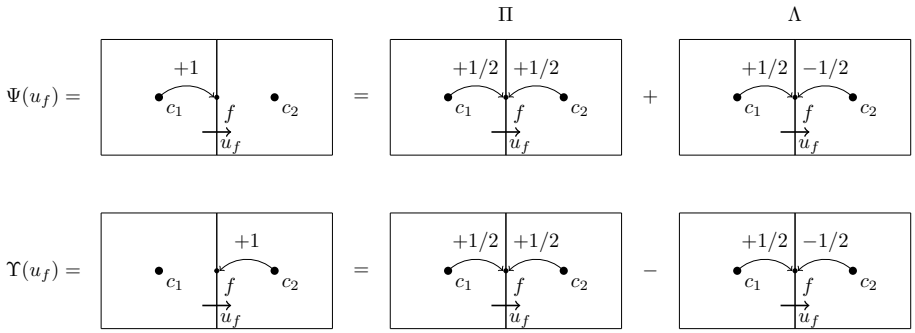

Figure 2.3: Example of a particular high-resolution scheme Ψ for the advection of $\theta_{\mathbf{c}}$ (in this example, the well-known upwind scheme) and the corresponding dedicated curvature interpolator, Y. In this case, the interpolation scheme for curvature is downwind.

2.4.3 Analysis

By mimicking equations (2.30) and (2.32) we obtain the discrete counterpart of kinetic energy as

$$\frac{d\mathbf{E_k}}{dt} = \gamma\left(\mathsf{UG}\theta_{\mathbf{c}}, \mathsf{Y}\mathbf{k_c}\right) + \mu\left(\mathbf{u_f}, \mathsf{L_F}\mathbf{u_f}\right), \tag{2.48}$$

which assumes a proper discretization of all other terms described in Section 2.3. We proceed similarly for potential energy by mimicking equation (2.34) to define discrete potential energy as

$$\frac{d\mathbf{E_p}}{dt} = \gamma\left(\mathsf{G}\frac{d\theta_{\mathbf{c}}}{dt}, \hat{\mathbf{n}}_{\mathbf{f}}\right) \tag{2.49}$$

We obtain the semi-discretized total energy equation by combining equations (2.48) and (2.49), which, in combination with equation (2.39) yields

$$\frac{d\mathbf{E_m}}{dt} = \frac{d\mathbf{E_k}}{dt} + \frac{d\mathbf{E_p}}{dt} = \gamma\left(\mathsf{UG}\theta_{\mathbf{c}}, \mathsf{Y}\mathbf{k_c}\right) + \mu\left(\mathbf{u_f}, \mathsf{L_F}\mathbf{u_f}\right) + \gamma\left(\mathsf{G}\frac{d\theta_{\mathbf{c}}}{dt}, \hat{\mathbf{n}}_{\mathbf{f}}\right) = \mu\left(\mathbf{u_f}, \mathsf{L_F}\mathbf{u_f}\right) \leq 0 \tag{2.50}$$

Which can be compared with equation (2.35) to check that (in the absence of viscosity) the proposed numerical setup satisfies energy conservation up to temporal

integration. Note that, as in the single-phase flow, this holds for any incompressible flow at the discrete level as well (i.e., $\mathsf{D}\mathbf{u_f} = 0_c$).

The role of interface recompression deserves a special remark. Customarily included in the level set literature [11, 32], its role is to recover the interface sharpness that may have been deteriorated by the convective schemes by taking additional, correcting steps after an initial advection stage. Nonetheless, even when performed conserving mass, as in [11, 12], the nature of recompression results in a non-null contribution to potential energy, which violates the conservation of mechanical energy. For this reason, the energy-preserving method presented here disregards recompression to focus on the physical coupling between marker advection and momentum transport. Similarly, other interface capturing schemes may consider additional steps aimed at recovering interface quality and/or mass conservation [44]. While the results presented here allow to adopt this formulation into the momentum equation, including additional correcting steps require an individualized analysis.

2.5 Results

Equipped with the discretization described in Section 2.4, we assess its performance for canonical tests for multiphase flow systems. We focus on inviscid simulations in order to isolate the performance of our newly developed discretization. Equations (2.1) and (2.5) are discretized according to the above-mentioned discretization. These read as

$$\frac{d\mathbf{u_f}}{dt} = -\mathsf{C}(\mathbf{u_f})_\mathsf{F}\mathbf{u_f} - \mathsf{G}\mathbf{p_c} + \gamma\mathsf{K}_\mathsf{F}\mathsf{G}\theta_\mathbf{c} \tag{2.51}$$

$$\frac{d\theta_\mathbf{c}}{dt} = -\mathsf{C}(\mathbf{u_f})_\mathsf{C}\theta_\mathbf{c} \tag{2.52}$$

where $\mathsf{K}_\mathsf{F} = \mathsf{diag}\left(\mathsf{Y}\mathbf{k_c}\right)$ is the diagonal arrangement of the staggered curvature.

Density ratio has been fixed to 1 in order to isolate the surface tension term, simplify the discretization of the convective term and facilitate the solution of the pressure-velocity decoupling. Nonetheless, as far as the convective term preserves skew-symmetry and the Poisson equation is solved exactly, ratios different than 1 may be included flawlessly. Surface tension forces are included as mentioned in Section 2.4

The system is integrated in time with a second-order Adams-Bashforth scheme while the pressure-velocity decoupling is achieved with a classical FSM [14]. An efficient FFT decomposition in the periodic direction coupled with a Cholesky solver is used to ensure divergence-free velocity fields to machine accuracy.

All simulations are carried on a $\Omega = [2H \times 2H]$ square domain, where H is both the semi-width and semi-height of the cavity. Top and bottom faces present periodic

boundary conditions, while at the sides no-flux boundary conditions is imposed for the marker function (i.e., $\nabla\theta \cdot \hat{n}_{wall} = 0$) while free slip is set for velocity (i.e., $\vec{u} \cdot \hat{n}_{wall} = 0$). This enforces conservation of all physical quantities.

Linear perturbation theory is used to obtain reference values for time, velocity and pressure. Note that linear perturbation assumes small interfacial deformation, while the cases presented here do not necessarily satisfy such a condition, it still provides with a reference value. Energy levels are scaled by and referenced to the initial observed mechanical energy. Because all simulations start with a fluid at rest and an elongated interface, kinetic energy evolves in the positive region (i.e., velocity is higher than or equal to the initial one) while potential energy evolves in the negative region (i.e., elongation is less than or equal to the initial one).

Tests are carried in order to compare the standard midpoint rule used for the interpolation of curvature proposed by Olsson and Kreiss [11] with the newly developed interpolation scheme. Recompression has been initially set aside in order to evaluate its impact on both schemes in a subsequent analysis. It is computed as

$$\frac{d\theta_{\mathbf{c}}}{d\tau} + \mathsf{D}\Gamma_{f\to c}\mathbf{N}_{\mathbf{C}}\left(\mathsf{I}_{\mathsf{C}} - \blacksquare_{\mathbf{C}}\right)\theta_{\mathbf{c}} = \mathsf{D}\mathbf{E}_{\mathbf{F}}\mathsf{G}\theta_{\mathbf{c}}, \tag{2.53}$$

where τ stands for pseudo-time, $\Gamma_{f\to c}$ is vector-valued shift operator, $\mathbf{N}_{\mathbf{C}} \in \mathbb{R}^{|\partial C|\times|C|}$ maps scalars to vector fields aligned with the interface normal, while $\blacksquare_{\mathbf{C}} = \mathsf{diag}(\theta_{\mathbf{c}})$ and $\mathbf{E}_{\mathbf{F}} = \mathsf{diag}(\epsilon_{\mathbf{f}})$ are the diagonal arrangements of, respectively, $\theta_{\mathbf{c}}$ and ϵ; where ϵ is the face-centered smoothing factor defined in Section 2.2.2. Further details can be found in Olsson and Kreiss [11] for the CLS and in Trias et al. [38] for the construction of the operators.

2.5.1 Cylindrical column

The classical setup of a zero gravity cylindrical column of liquid is tested in order to show the impact of the newly proposed method into spurious currents. The section of the column is located at the center of the domain and is given a radius of $R_0 = 0.3H$. Velocity is initially stagnant and that is how it should remain throughout the simulation; however, spurious currents are expected to appear due to errors in the calculation of curvature [27]. The initial setup is depicted in Figure 2.4.

Linear perturbation theory provides with the time period for an initially cylindrical interface perturbed as $r(\theta) = R_0 + r_p cos(s\theta)$, where $s = 2, 3, 4, \ldots$ corresponding to ellipsoidal, triangular of rectangular deformations, respectively [45]. Because linear theory predicts perfect equilibrium for both $s = 0$ and $s = 1$, we arbitrarily assume an ellipsoidal perturbation (i.e., $s = 2$) in order to obtain a reference state. The oscillation period can be computed for any s as $T = 2\pi/\sqrt{2\rho R_0^3/\gamma s(s^2-1)}$ [46], while the characteristic length scale is $L = 2\pi R_0$, which leads a characteristic speed

of $c = L/T = \sqrt{\gamma s(s^2-1)/2\rho R_0^3}$, while pressure is referenced to ρc^2. Integration is carried over $5T$.

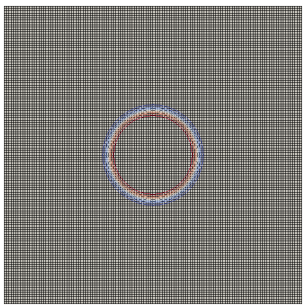

Figure 2.4: Initial setup of the marker function for cylindrical column test case in a 128×128 mesh. Contour lines are plotted for $\Delta\theta = 0.1$.

Results in Figure 2.5 show how the newly proposed method (right column) results in an energy stable simulation by counterbalancing the numerical increase in kinetic energy with a decrease of potential energy. This yields to a stagnant situation in which both kinetic and potential energy restore their initial values (i.e., $E_k = 0$ and $E_p = 0$). On the other hand, the standard midpoint rule interpolation for curvature (left column) results in an increase in total energy .

In Figure 2.6 it can be seen how the newly developed curvature interpolation scheme (right) provides, first of all, an order of magnitude smaller oscillations that the standard one produces (left). In addition, there is a dramatic increase in the flow quality within the interface, extending the benefits of the high resolution advection scheme for the marker into the velocity field. On the other hand, the use of the standard midpoint rule for updating curvature pollutes the flow within both phases.

It is remarkable how, despite initializing the interface to a theoretical minimum energy situation (i.e., cylindrical cross-section), numerical imbalances when computing curvature does not reflect such a situation [27]. Nonetheless, the use of an energy-preserving scheme acts in order to keep energy constant, and so counterbalances such an artificial movement by modifying the curvature accordingly. This results in a robust method which eventually is perturbation-proof.

In comparison with Figure 2.5, Figure 2.7 shows the impact of recompression in both schemes. As can be seen, the newly developed interpolation method can do little in terms of energy, as the recompression stage increases the energy of the system. Actually, we see how the increase in kinetic energy is even higher than in

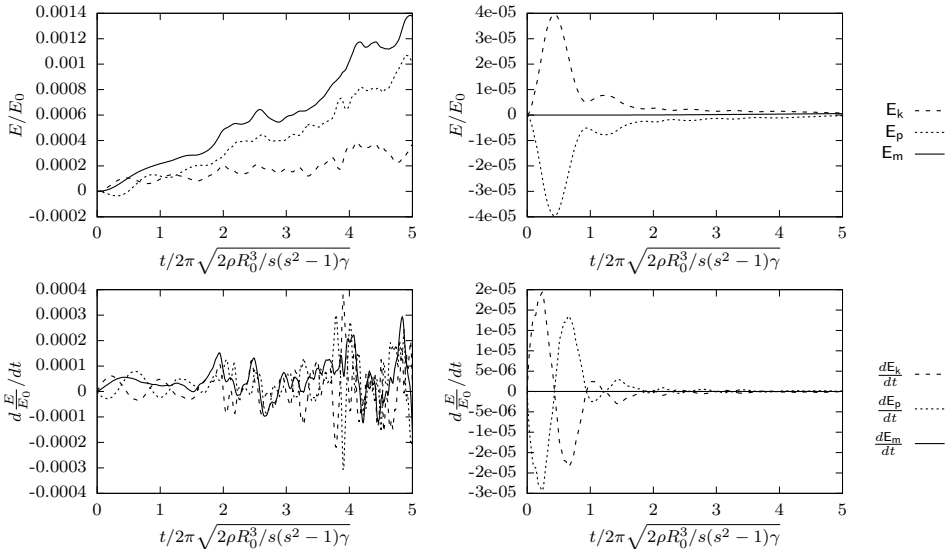

Figure 2.5: Energy evolution of the cylindrical section for a pure advection case (i.e., no recompression) with the standard interpolation of Olsson and Kreiss [11] for the curvature (left) and the newly proposed method (right) in a 128×128 mesh. Top rows show the discrete values of kinetic ($\mathbf{E_k}$), potential ($\mathbf{E_p}$) and total ($\mathbf{E_m}$) energy. Bottom rows show their semi-discretized time derivative according to equations (2.48), (2.49) and (2.50), respectively.

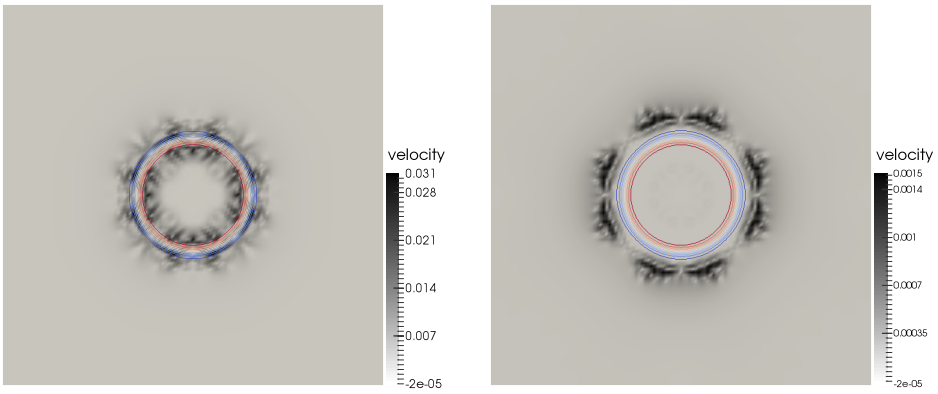

Figure 2.6: Velocity magnitude and interface location at $t = 5T$ for a cylindrical column in a 128×128 mesh advected without recompression. Left figure uses the standard midpoint rule while the right one uses the newly developed energy-preserving one. Contour lines are plotted for $\Delta\theta = 0.1$.

the previous case, with no recompression associated.

On the other hand, Figure 2.8 shows how the velocity field is clearly distorted in both cases, degrading the solution with respect to the pure advection algorithm one and two orders of magnitude with respect to the midpoint and the energy-preserving interpolation schemes, respectively. Noticeably, we still retain, even by including the recompression scheme, a higher quality of the velocity field within the bounded region for the newly developed interpolation scheme. The impact of recompression in the overall quality of the solution is discussed in Section 3.5.

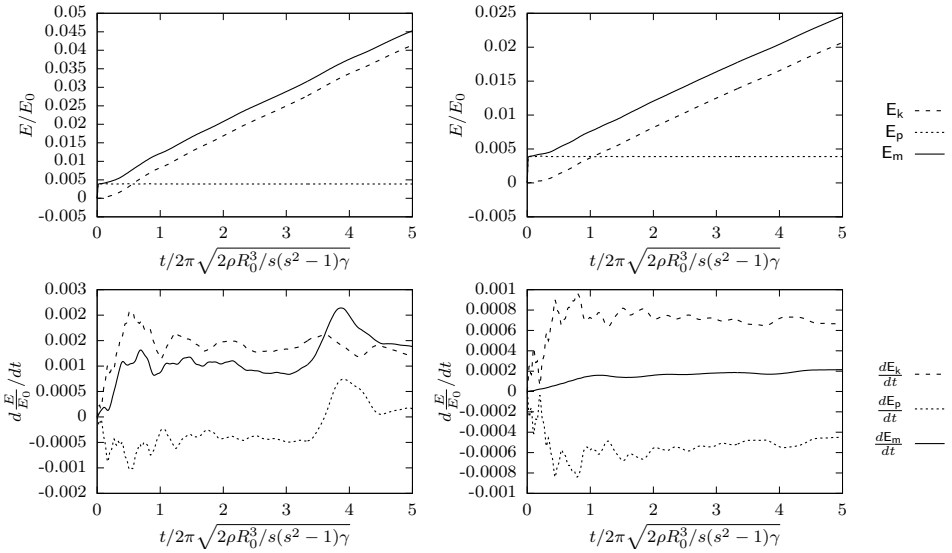

Figure 2.7: Energy evolution of cylindrical column with the complete Olsson and Kreiss method [11] with a single recompression stage (left), and the same method including the modified curvature interpolation (right) in a 128×128 mesh. Top rows show the discrete values of kinetic ($\mathbf{E_k}$), potential ($\mathbf{E_p}$) and total ($\mathbf{E_m}$) energy. Bottom rows show their semi-discretized time derivative according to equations (2.48), (2.49) and (2.50), respectively.

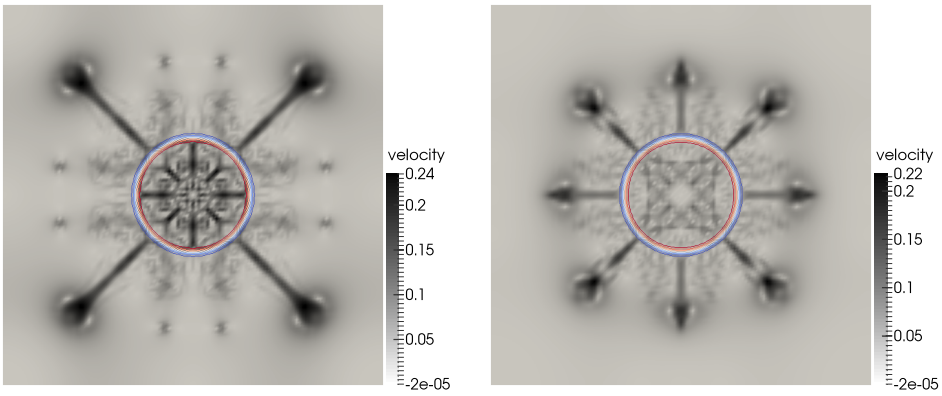

Figure 2.8: Velocity magnitude and interface location at $t = 5T$ for a cylindrical column in a 128×128 mesh advected with a single recompression step. Left figure uses the standard 2nd order shift operator while the right one uses the newly developed energy-preserving one. Contour lines are plotted for $\Delta\theta = 0.1$.

2.5.2 Oscillating ellipsoidal column

In order to stretch the previous result to a dynamic equilibrium situation, an ellipsoidal section is set by distorting the initially cylindrical case. As in the cylindrical water column, spurious currents may appear, while this time they accompany legitimate currents as a result of regions with a moderate non-constant curvature. The ellipse is centered in the domain and is defined by $x = 0.5cos(\alpha)$ and $y = 0.3sin(\alpha)$, where $\alpha \in [0, 2\pi)$. Velocity field is initialized at rest and should follow to the oscillation of the ellipsoid throughout the simulation. The initial setup is depicted in Figure 2.9.

In the same fashion that in the cylindrical water column described above, linear perturbation theory is employed in order to obtain a reference state. Characteristic length is set to $L = 2\pi R_0$, where $R_0 = 0.3$. Time, velocity and pressure scales used are the same than those for the cylindrical section case.

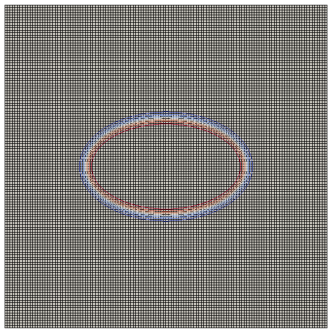

Figure 2.9: Initial setup of the marker function for the oscillating ellipse test case in a 128×128 mesh. Contour lines are plotted for $\Delta\theta = 0.1$.

Figure 2.10 shows how, while the standard midpoint interpolation (left) clearly increases the mechanical energy of the system, the newly proposed energy-preserving interpolation scheme for curvature (right) preserves mechanical energy, which yields physically consistent results and numerically stable simulations. There is, however, both positive and negative offsets for kinetic and potential energies. While kinetic and potential energy are supposed to oscillate between 0 and its maximum or minimum for an ideal harmonic oscillator, we observe that this is not the case. This is explained by an imbalance in the momentum equation, which provides an artificial acceleration in the fluid, resulting in an increase of the kinetic energy base state [47]. By virtue of the energy-preserving scheme the oscillation gap for potential energy is reduced accordingly, resulting in a decrease of the elongation amplitude. This plays

a relevant role in the next case presented, the capillary wave, which is further discussed in the next subsection. Despite this well-known issue results still show the expected oscillatory behavior of the ellipsoid. This can be checked from the bottom row of Figure 2.10, where the magnitude of the energy transfers remains approximately constant throughout the simulation. In terms of the oscillating behavior, the increase in mechanical energy for the naive interpolation results not only in artificially higher values of kinetic energy, but also in a phase difference with respect to the energy-preserving one.

Figure 2.11 presents the marker and velocity fields after $t = 5T$ with a pure advection scheme. Results for the energy-preserving scheme (right) show a shift in phase with respect to the midpoint interpolation scheme (left). Velocity is not only higher for the naive approach, but also the shape of the interface provides with non-physical curvature, as it can be observed by the kink appearing along the horizontal centerline of the ellipsoid (left), which can be compared with the smoother profile present in the energy-preserving approach (right).

In summary, the use of the energy-preserving scheme provides a higher degree of reliability, by preserving mechanical energy also in a dynamical equilibrium situation. Despite the numerical errors in which the discretization of momentum may occur, the method is robust and still preserves mechanical energy.

The results obtained by including a single recompression step into the algorithm are presented in Figure 2.12. They show how, irrespective of the use of an energy-preserving scheme into the advection scheme, the amount of energy included into the system in order to keep a sharper profile results in a small, but non-physical, increase of mechanical energy. Compared with Figure 2.10, it can be seen how the difference is not as much in mechanical energy but rather in the nature of the oscillations. While results without recompression still preserve to some extent the oscillating nature of the physical system, recompression produces an enhanced smoothing, resulting in a flat profile in terms of both kinetic and potential energy.

The claim stated above can be clearly seen in Figure 2.13, where the initial ellipsoid, expected to present a dynamical equilibrium, results in a fully rounded shape. Besides, Figure 2.13 shows how the resulting fields, in both cases, are irrespective of the interpolation scheme for curvature used for the advection scheme. Further discussion on the impact of recompression in the final result is discussed in Section 3.5.

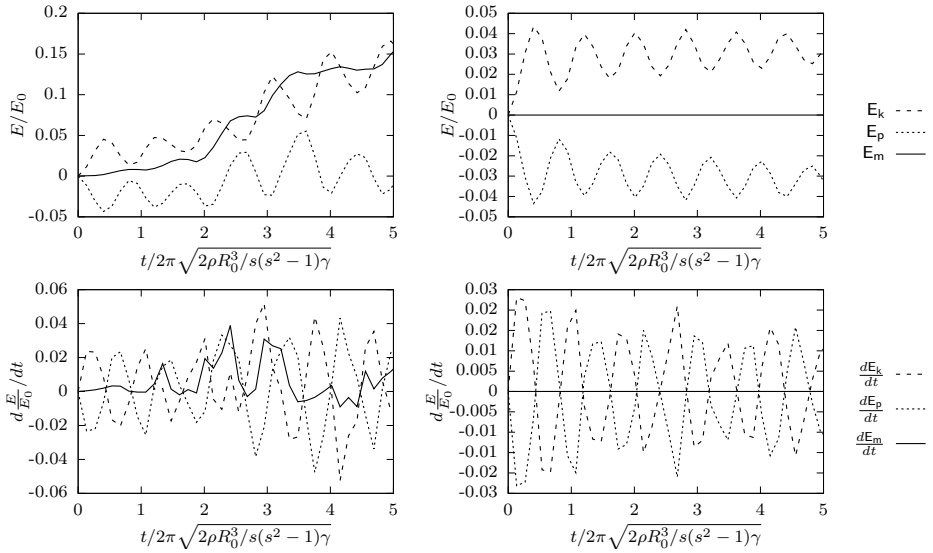

Figure 2.10: Energy evolution of the ellipsoidal section for a pure advection case (i.e., no recompression) with the standard interpolation of Olsson and Kreiss [11] for the curvature (left) and the newly proposed method (right) in a 128×128 mesh. Top rows show the discrete values of kinetic ($\mathbf{E_k}$), potential ($\mathbf{E_p}$) and total ($\mathbf{E_m}$) energy. Bottom rows show their semi-discretized time derivative according to equations (2.48), (2.49) and (2.50), respectively.

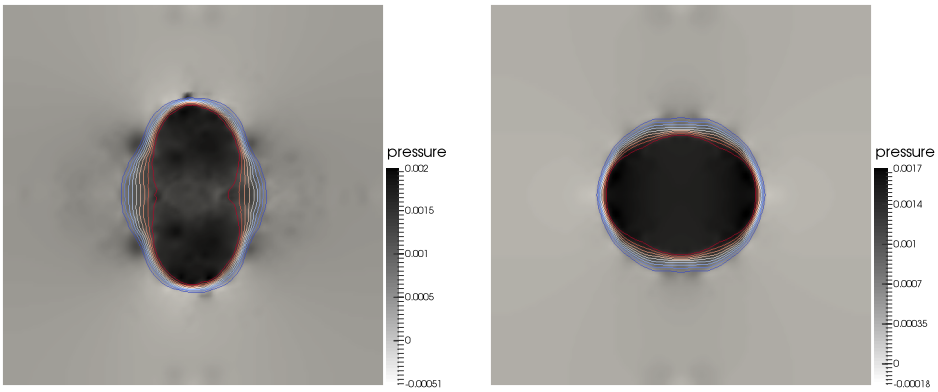

Figure 2.11: Pressure field and interface location at $t = 5T$ for the oscillating ellipse in a 128×128 mesh advected without recompression. Left figure uses the standard 2nd order shift operator while the right one uses the newly developed energy-preserving one. Contour lines are plotted for $\Delta\theta = 0.1$.

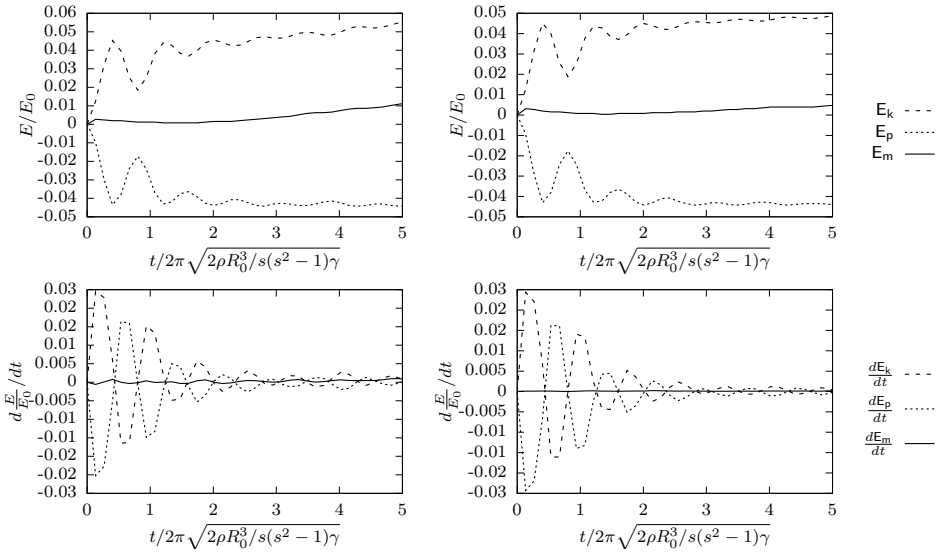

Figure 2.12: Energy evolution of the oscillating ellipse with the complete Olsson and Kreiss method [11] with a single recompression stage (left), and the same method including the modified curvature interpolation (right) in a 128×128 mesh. Top rows show the discrete values of kinetic ($\mathbf{E_k}$), potential ($\mathbf{E_p}$) and total ($\mathbf{E_m}$) energy. Bottom rows show their semi-discretized time derivative according to equations (2.48), (2.49) and (2.50), respectively.

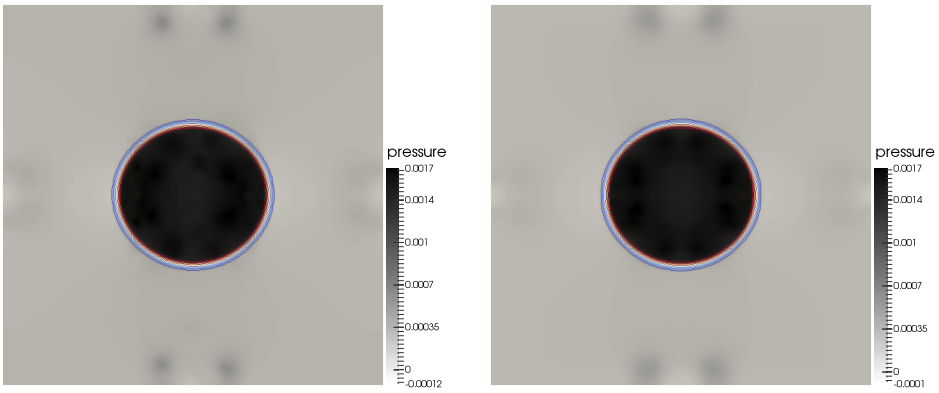

Figure 2.13: Pressure field and interface location at $t = 5T$ for the oscillating ellipse in a 128×128 mesh advected with a single recompression step. Left figure uses the standard 2nd order shift operator while the right one uses the newly developed energy-preserving one. Contour lines are plotted for $\Delta\theta = 0.1$.

2.5.3 Capillary wave

A pure capillary wave is set by originally locating the interface at $x = 0.2sin(ky)$, producing an initial wave along the vertical center line of wavelength $2\pi/k$. We set $k = \pi/H$, so that a single oscillating period is contained within the domain. Velocity is initially at rest. With the mentioned boundary and initial conditions, the wave is expected to oscillate indefinitely, alternating states of maximum potential energy (i.e., maximum elongation) and minimum kinetic energy (i.e., fluid at rest) and vice-versa. Initial setup is presented in Figure 2.14.

As is well known from linear perturbation theory [45], the oscillation of the given setup present a characteristic period of $T = 2\pi\sqrt{2\rho/\gamma k^3 tanh(kH)}$, which is used as the reference value for time. On the other hand, the characteristic length scale is $L = 2\pi/k$, the wavelength of the perturbation. This yields a characteristic velocity of $c = L/T = \sqrt{\gamma\, k\, tanh(kH)/2\rho}$, while pressure is referenced to ρc^2, where ρ stands for the average. Integration in time is set to $2T$.

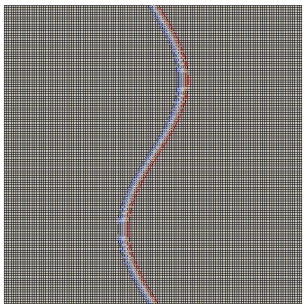

Figure 2.14: Initial setup of the marker function in a 128×128 mesh. Contour lines are plotted for $\Delta\theta = 0.1$.

Results in Figure 2.15 show how the energy preserving discretization proposed in the present work preserves mechanical energy (top row, solid line) by balancing the resulting energy transfers (bottom row, solid line). While the standard midpoint interpolation of curvature results in a non-physical increase of mechanical energy, which ultimately leads to instabilities, the novel proposed method provides a stable discretization.

Even when mechanical energy is conserved in the newly proposed method, both the amplitude of kinetic and potential oscillations (Figure 2.15, top row, right) and the magnitude of the energy transfers (Figure 2.15, bottom row, right) exhibit a significant damping. The reason behind such a damping is the non-null contribution of

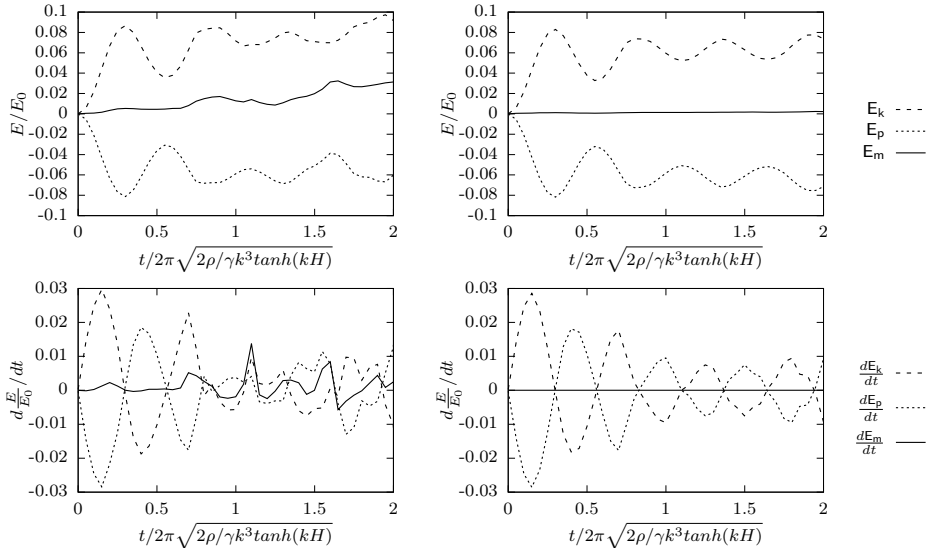

Figure 2.15: Energy evolution of the capillary wave for a pure advection case (i.e., no recompression) with the standard interpolation of Olsson and Kreiss [11] for the curvature (left) and the newly proposed method (right) in a 128×128 mesh. Top rows show the discrete values of kinetic ($\mathbf{E_k}$), potential ($\mathbf{E_p}$) and total ($\mathbf{E_m}$) energy. Bottom rows show their semi-discretized time derivative according to equations (2.48), (2.49) and (2.50), respectively.

surface tension to the momentum equation (the desired result for a closed surface) which produces an artificial acceleration of the fluid. The origin of such artificial acceleration lies in the discretization of curvature, particularly the computation of normals, which is at the origin of the errors that propagate to the momentum equation. This non-physical increase in kinetic energy manifests itself as an increase of the base level of kinetic energy at off-peaks, as can be seen in the top row of Figure 2.15. While naive interpolation techniques are unresponsive to such energy increments, the new energy-preserving method adjusts the transfers between kinetic and potential energies through surface tension to keep mechanical energy constant. As a result, the artificial and progressive increase in the kinetic energy level leaves no room to capillary oscillations, driving the system to a stagnant, but stable, situation.

Figure 2.17, on the other hand, includes a recompression step into the evolution of the wave. Results show clearly how, despite its known advantages [11], the resulting solution does not preserve energetic balances but rather increase total en-

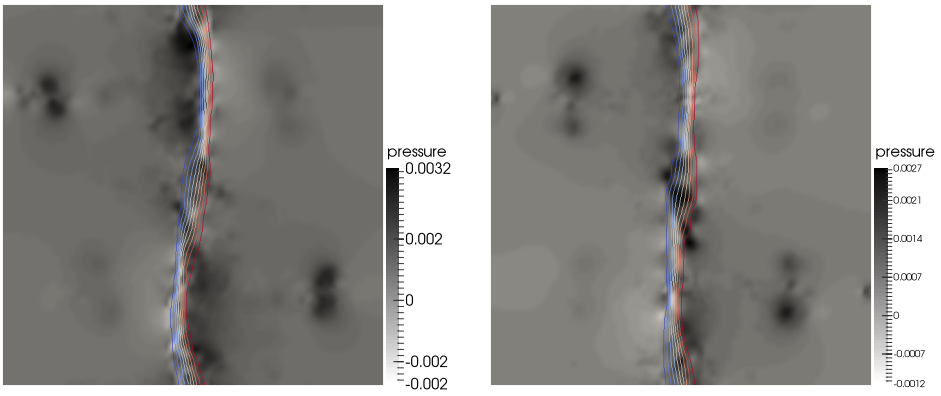

Figure 2.16: Pressure field and interface location at $t = 2T$ for a pure capillary wave in a 128×128 mesh advected without recompression. Left figure uses the standard 2nd order shift operator while the right one uses the newly developed energy-preserving one. Contour lines are plotted for $\Delta\theta = 0.1$.

ergy of the system, leading to eventual instabilities. It can be seen how the gain in sharpness introduced by recompression schemes is at the expenses of destroying the advantages of the energy-preserving discretization. Results in Figure 2.18 can be compared with those of Figure 2.16, which shows how recompression increases the total energy of the system. Namely, the scale in Figure 2.18 shows how velocity magnitudes are clearly higher regardless of the advective step is energy-preserving or not. Among them, the energy-preserving scheme shows milder velocity fields. This role of recompression is analyzed in Section 3.5.

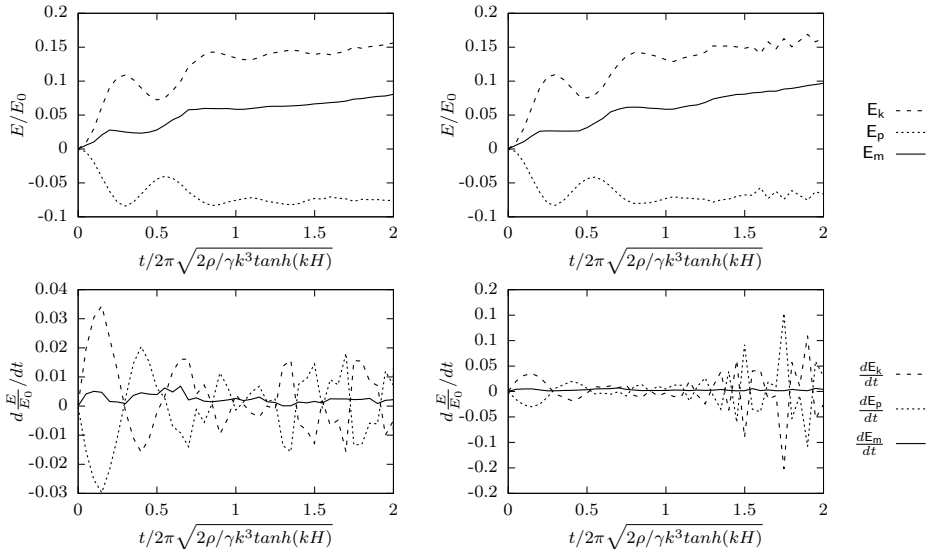

Figure 2.17: Energy evolution of the capillary wave with the complete Olsson and Kreiss method [11] with a single recompression stage (left), and the same method including the modified curvature interpolation (right) in a 128×128 mesh. Top rows show the discrete values of kinetic ($\mathbf{E_k}$), potential ($\mathbf{E_p}$) and total ($\mathbf{E_m}$) energy. Bottom rows show their semi-discretized time derivative according to equations (2.48), (2.49) and (2.50), respectively.

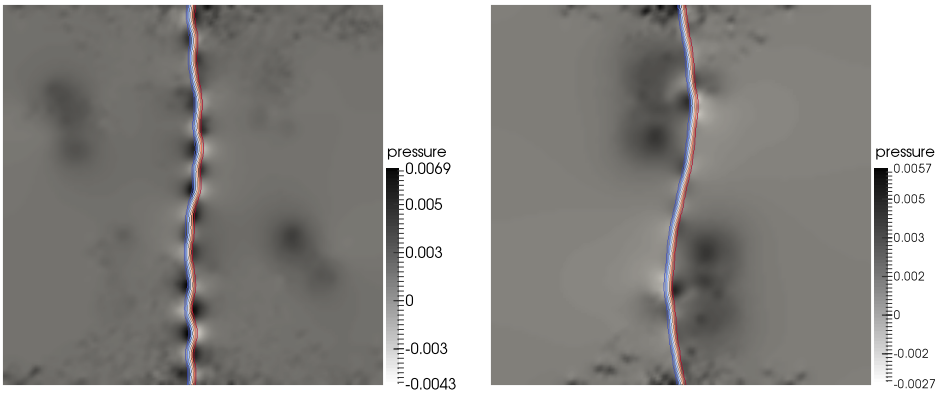

Figure 2.18: Pressure field and interface location at $t = 2T$ for a capillary wave in a 128×128 mesh advected with a single recompression step. Left figure uses the standard 2nd order shift operator while the right one uses the newly developed energy-preserving one. Contour lines are plotted for $\Delta\theta = 0.1$.

2.6 Concluding Remarks

By incorporating the first variation of area, equation (2.9), into the continuum formulation we have explicitly imposed a novel condition to the system. Equation (2.14) shows that the use of a smooth marker function is compatible with such a condition. This condition is implicitly incorporated into the discretized system by means of a newly developed curvature cell-to-face shift operator, Y, defined in equation (2.47). Analytical and numerical assessments provide evidence that, in the absence of recompression, the novel interpolation scheme preserves mechanical energy up to temporal integration by balancing kinetic and potential energy transfers to machine accuracy.

The exact value of both kinetic and potential energy is not achieved due to the lack of conservation of linear momentum. This implies that, while the transfers between surface and kinetic energy are equal and of opposite sign, its magnitude is not necessarily the correct one..

In this regard, the adoption of a fully conservative momentum formulation, along with proper discretization techniques for the convective operator, as already announced in Section 2.4.2, should be considered in a general case. However, the formulation of the surface tension is the most challenging term. Not being cast into a conservative form, it relies on the accurate capturing of the interface to produce a closed, and thus conservative, force field. In summary, the use of a finite grid prevents us from resolving the finest scales of the interface, represented by the marker function θ. This under-resolution of θ, either induced both by the mesh and the advection scheme, induces subsequent errors in the computation of both $\hat{\eta}_i$ and κ, as stated by Magnini et al. [27]. These errors spread into the momentum equation, which can be seen as a back-scatter of energy from the finest, unresolved, surface representation scales into larger kinematic ones, manifesting itself as an inappropriate momentum balance, which ultimately leads to an inaccurate kinetic energy level. This is a well-known issue in multiphase flows and the object of ongoing research [48, 49].

Nevertheless, despite the lack of linear momentum conservation, mechanical energy is conserved and thus the stability of the system is guaranteed up to temporal integration. From this perspective, the novel technique may provide extra reliability for surface energy governed phenomena, particularly those involving surface breakup or coalesce, as it may occur in atomization processes or Plateau-Rayleigh instabilities, among others.

Recompression schemes, despite producing an energetic imbalance, as has been shown in Section 3.4, are common in the level-set community. They preserve a coherent marker field at the expenses of introducing non-physical energy to the system. Even when the proposed method enforces the energetic consistency between marker and momentum transport equations, the inclusion of recompression prevents us

from obtaining a fully energy-preserving scheme. Following the spirit described in Section 2.4, a first approach may be to modify the recompression step to produce not only a conservative, but an energetically neutral resharpening. Enforcing a null contribution to potential energy of equation (2.53), if possible, would allow an arbitrary number of recompression steps, avoiding any penalty in terms of energetic balances. Although this would be desirable, it requires to re-formulate a mass- and energy- conservative recompression scheme which effectively moves the interface irrespective of advection, which is definitively not obvious.

Others have tried to include recompression within the advection step to yield a single-step method. After all, recompression is included to fix the distortion produced by interface advection. This leads to phase-field-like methods [50, 51]. Interpreting this idea as a custom-made high resolution scheme, these approaches can eventually be cast into a convective form like that in equations (2.46) and proceed to obtain the equivalent curvature interpolation as in equation (2.47). A variant of this model may be to approach the advection of the marker function as a regularization problem [52].

Lastly, both a review of the well-known symmetry-preserving scheme and the development of the energy-preserving scheme have been approached from an algebraic point of view. Aside from the advantages in terms of algebraic analysis, the use of an algebra-based discretization provides an opportunity for High Performance Computing (HPC) optimization, parallelization and portability [53]. By casting differential forms into algebraic ones, (i.e., matrices and vectors), it has been shown in [53] that nearly 90% of the operations comprised in a typical FSM algorithm for the solution of incompressible Navier-Stokes equations can be reduced to Sparse Matrix-Vector multiplication (SpMV), generalized vector addition (AXPY) and dot product (DOT). In this regard, the present formulation falls within a smart strategy towards portable, heterogeneous, HPC.

2.7 Acknowledgements

This work has been financially supported by the Ministerio de Economía y Competitividad, Spain (ENE2017-88697-R and ENE2015-70672-P) as well as an FI AGAUR-Generalitat de Catalunya fellowship (2017FI_B_00616) and a Ramón y Cajal postdoctoral contract (RYC-2012-11996). The authors are grateful to Prof. Roel Verstappen, Prof. Arthur Veldman and MSc Ronald Remmerswaal for their enriching discussions.

References

[1] Sébastien Tanguy, Thibaut Ménard, and Alain Berlemont. A Level Set Method for vaporizing two-phase flows. *J. Comput. Phys.*, 221(2):837–853, 2007.

[2] Olivier Desjardins, Vincent Moureau, and Heinz Pitsch. An accurate conservative level set/ghost fluid method for simulating turbulent atomization. *J. Comput. Phys.*, 227(18):8395–8416, 2008.

[3] B. P. Van Poppel, O. Desjardins, and J. W. Daily. A ghost fluid, level set methodology for simulating multiphase electrohydrodynamic flows with application to liquid fuel injection. *J. Comput. Phys.*, 229(20):7977–7996, 2010.

[4] Sébastien Tanguy, Michaël Sagan, Benjamin Lalanne, Frédéric Couderc, and Catherine Colin. Benchmarks and numerical methods for the simulation of boiling flows. *J. Comput. Phys.*, 264:1–22, 2014.

[5] Mathieu Lepilliez, Elena Roxana Popescu, Frédéric Gibou, and Sébastien Tanguy. On two-phase flow solvers in irregular domains with contact line. *J. Comput. Phys.*, 321(August):1217–1251, 2016.

[6] E. Gutiérrez, N. Balcázar, E. Bartrons, and J. Rigola. Numerical study of Taylor bubbles rising in a stagnant liquid using a level-set/moving-mesh method. *Chem. Eng. Sci.*, 164:158–177, 2017.

[7] C. W. Hirt and B. D. Nichols. Volume of fluid (VOF) method for the dynamics of free boundaries. *J. Comput. Phys.*, 39(1):201–225, 1981.

[8] Stanley Osher and James A. Sethian. Fronts propagating with curvature-dependent speed: Algorithms based on Hamilton-Jacobi formulations. *J. Comput. Phys.*, 79(1):12–49, 1988.

[9] D. M. Anderson, G. B. McFadden, and A. A. Wheeler. Diffuse-Interface Methods in Fluid Mechanics. *Annu. Rev. Fluid Mech.*, 30(1):139–165, 1998.

[10] S Mirjalili, S S Jain, and M S Dodd. Interface-capturing methods for two-phase flows : An overview and recent developments. *Annu. Res. Briefs*, (1):117–135, 2017.

[11] Elin Olsson and Gunilla Kreiss. A conservative level set method for two phase flow. *J. Comput. Phys.*, 210(1):225–246, nov 2005.

[12] Elin Olsson, Gunilla Kreiss, and Sara Zahedi. A conservative level set method for two phase flow II. *J. Comput. Phys.*, 225(1):785–807, 2007.

[13] N. Balcázar, L. Jofre, O. Lehmkuhl, J. Castro, and J. Rigola. A finite-volume/level-set method for simulating two-phase flows on unstructured grids. *Int. J. Multiph. Flow*, 64:55–72, may 2014.

[14] Alexandre Joel Chorin. Numerical solution of the Navier-Stokes equations. *Math. Comput.*, 22:745–762, 1968.

[15] R. W. C. P. Verstappen and A. E. P. Veldman. Direct numerical simulation of turbulence at lower costs. *J. Eng. Math.*, (c):143–159, 1997.

[16] R. W. C. P. Verstappen and A. E. P. Veldman. Symmetry-preserving discretization of turbulent flow. *J. Comput. Phys.*, 187(1):343–368, 2003.

[17] Konstantin Lipnikov, Gianmarco Manzini, and Mikhail Shashkov. Mimetic finite difference method. *J. Comput. Phys.*, 257(PB):1163–1227, 2014.

[18] Nicolas Robidoux and Stanly Steinberg. A discrete vector calculus in tensor grids. *Comput. Methods Appl. Math.*, 11(1):23–66, 2011.

[19] Enzo Tonti. Why starting from differential equations for computational physics? *J. Comput. Phys.*, 257(PB):1260–1290, jan 2014.

[20] J. Blair Perot. Discrete Conservation Properties of Unstructured Mesh Schemes. *Annu. Rev. Fluid Mech.*, 43(1):299–318, 2011.

[21] F. X. Trias, A. Gorobets, and A. Oliva. Turbulent flow around a square cylinder at Reynolds number 22,000: A DNS study. *Comput. Fluids*, 123:87–98, 2015.

[22] L. Paniagua, O. Lehmkuhl, C. Oliet, and C. D. Pérez-Segarra. Large eddy simulations (LES) on the flow and heat transfer in a wall-bounded pin matrix. *Numer. Heat Transf. Part B Fundam.*, 65(2):103–128, 2014.

[23] H. Giráldez, C. D. Pérez Segarra, C. Oliet, and A. Oliva. Heat and moisture insulation by means of air curtains: Application to refrigerated chambers. *Int. J. Refrig.*, 68:1–14, 2016.

[24] D. Fuster. An energy preserving formulation for the simulation of multiphase turbulent flows. *J. Comput. Phys.*, 235:114–128, 2013.

[25] M. Sussman, K. M. Smith, M. Y. Hussaini, M. Ohta, and R. Zhi-Wei. A sharp interface method for incompressible two-phase flows. *J. Comput. Phys.*, 221(2):469–505, 2007.

[26] Benjamin Lalanne, Lucia Rueda Villegas, Sébastien Tanguy, and Frédéric Risso. On the computation of viscous terms for incompressible two-phase flows with Level Set/Ghost Fluid Method. *J. Comput. Phys.*, 301:289–307, 2015.

[27] M. Magnini, B. Pulvirenti, and J. R. Thome. Characterization of the velocity fields generated by flow initialization in the CFD simulation of multiphase flows. *Appl. Math. Model.*, 40(15-16):6811–6830, 2016.

[28] David Jacqmin. Calculation of Two-Phase Navier–Stokes Flows Using Phase-Field Modeling. *J. Comput. Phys.*, 155(1):96–127, oct 1999.

[29] Didier Jamet, David Torres, and J U Brackbill. On the Theory and Computation of Surface Tension: The Elimination of Parasitic Currents through Energy Conservation in the Second-Gradient Method. *J. Comput. Phys.*, 182:262–276, 2002.

[30] D. Jamet and C. Misbah. Toward a thermodynamically consistent picture of the phase-field model of vesicles: Curvature energy. *Phys. Rev. E - Stat. Nonlinear, Soft Matter Phys.*, 78(3):1–8, 2008.

[31] G. Tryggvason, B. Bunner, a. Esmaeeli, D. Juric, N. Al-Rawahi, W. Tauber, J. Han, S. Nas, and Y.-J. Jan. A Front-Tracking Method for the Computations of Multiphase Flow. *J. Comput. Phys.*, 169(2):708–759, 2001.

[32] Mark Sussman. *A Level Set Approach for Computing Solutions to Incompressible Two-Phase Flow*. PhD thesis, UCLA, 1994.

[33] S. Chen, B. Merriman, S. Osher, and P. Smereka. A Simple Level Set Method for Solving Stefan Problems. *J. Comput. Phys.*, 135(1):8–29, 1997.

[34] Tomasz Wacławczyk. A consistent solution of the re-initialization equation in the conservative level-set method. *J. Comput. Phys.*, 299:487–525, 2015.

[35] J.U Brackbill, D.B Kothe, and C Zemach. A continuum method for modeling surface tension. *J. Comput. Phys.*, 100(2):335–354, jun 1992.

[36] Theodore Frankel. *The Geometry of Physics*. Cambridge University Press, Cambridge, 3 edition, 2012.

[37] J. E. Hicken, F. E. Ham, J. Militzer, and M. Koksal. A shift transformation for fully conservative methods: Turbulence simulation on complex, unstructured grids. *J. Comput. Phys.*, 208(2):704–734, 2005.

[38] F. X. Trias, O. Lehmkuhl, A. Oliva, C. D. Pérez-Segarra, and R. W. C. P. Verstappen. Symmetry-preserving discretization of Navier–Stokes equations on collocated unstructured grids. *J. Comput. Phys.*, 258:246–267, feb 2014.

[39] F. Capuano, G. Coppola, L. Rández, and L. de Luca. Explicit Runge–Kutta schemes for incompressible flow with improved energy-conservation properties. *J. Comput. Phys.*, 328:86–94, 2017.

[40] J. T. Davies and E. K. Rideal. *Interfacial Phenomena*. Academic Press Inc., London, 1961.

[41] W. Rozema, J. C. Kok, R. W. C. P. Verstappen, and A. E. P. Veldman. A symmetry-preserving discretisation and regularisation model for compressible flow with application to turbulent channel flow. *J. Turbul.*, 15(6):386–410, 2014.

[42] N. Valle, X. Álvarez, F. X. Trias, J. Castro, and A. Oliva. Algebraic implementation of a flux limiter for heterogeneous computing. In *Tenth Int. Conf. Comput. Fluid Dyn.*, Barcelona, July, 2018.

[43] Jitendra Kumar Patel and Ganesh Natarajan. A generic framework for design of interface capturing schemes for multi-fluid flows. *Comput. Fluids*, 106:108–118, 2015.

[44] O. Ubbink and R.I. Issa. A Method for Capturing Sharp Fluid Interfaces on Arbitrary Meshes. *J. Comput. Phys.*, 153(1):26–50, 1999.

[45] Sir Horace Lamb. *Hydrodynamics*. Dover Publications, Inc., New York, NY, 1945.

[46] D.E Fyfe, E.S Oran, and M.J Fritts. Surface tension and viscosity with lagrangian hydrodynamics on a triangular mesh. *J. Comput. Phys.*, 76(2):349–384, jun 1988.

[47] Stéphane Popinet. Numerical Models of Surface Tension. *Annu. Rev. Fluid Mech.*, 50(1):49–75, 2017.

[48] Junseok Kim. A continuous surface tension force formulation for diffuse-interface models. *J. Comput. Phys.*, 204(2):784–804, 2005.

[49] Moataz O. Abu-Al-Saud, Stéphane Popinet, and Hamdi A. Tchelepi. A conservative and well-balanced surface tension model. *J. Comput. Phys.*, 371:896–913, 2018.

[50] Jean Luc Guermond, Manuel Quezada de Luna, and Travis Thompson. An conservative anti-diffusion technique for the level set method. *J. Comput. Appl. Math.*, 321:448–468, 2017.

[51] Shahab Mirjalili, Christopher B. Ivey, and Ali Mani. A conservative diffuse interface method for two-phase flows with provable boundedness properties. mar 2018.

[52] F. X. Trias, D. Folch, A. Gorobets, and A. Oliva. Spectrally-Consistent Regularization of Navier–Stokes Equations. *J. Sci. Comput. (published online)*, 2018.

[53] X. Álvarez, A. Gorobets, F. X. Trias, R. Borrell, and G. Oyarzun. HPC2—A fully-portable, algebra-based framework for heterogeneous computing. Application to CFD. *Comput. Fluids*, 173:285–292, sep 2018.

3

Vectorial implementation of flux limiters for HPC.

Contents of this chapter are partially published in:

N. Valle, X. Álvarez, F.X. Trias, J. Castro, A. Oliva. Algebraic implementation of a flux limiter for heterogeneous computing. *Tenth Int. Conf. Comput. Fluid Dyn., 2018*

X. Álvarez, N. Valle, A. Gorobets, F.X. Trias. Implementation of a flux-limiter into a fully-portable, algebra-based framework for heterogeneous computing. *Tenth Int. Conf. Comput. Fluid Dyn., 2018*

And provided here self-contained.

Abstract. The use of flux limiters is widespread within the scientific computing community to capture shock discontinuities and are of paramount importance for the temporal integration of high-speed aerodynamics and multiphase flows, among others.

However, the breakthrough of new heterogeneous architectures in supercomputing facilities pose a huge portability challenge, particularly for legacy codes, since the computing subroutines that form the algorithms, so-called kernels, must be adapted to complex parallel programming paradigms. From this perspective, the research for innovative implementation approaches relying on minimalist sets of kernels simplifies the deployment of scientific computing software in massive supercomputers.

Equipped with basic algebraic topology and graph theory underlying the classical mesh concept, a new flux limiter formulation is conceived which is based on the adoption of algebraic data structures and kernels. As a result, traditional flux limiters are cast into a stream of two types of computing kernels: sparse matrix-vector multiplication and generalized point-wise binary operators. The newly proposed formulation eases the deployment of such a numerical technique in parallel, potentially heterogeneous, computational systems.

3.1 Introduction

Sharp discontinuities are present in many industrial applications. Such discontinuities appear in both compressible and multiphase flows, among others. In the context of hyperbolic systems, discontinuities develop as shock waves, which present a challenge for numerical calculations. Traditionally, high speed aerodynamics has focused on the appropriate treatment of such discontinuities by developing shock capturing schemes [1].

As a consequence of Godunov's theorem [1] (after [2]) the treatment of shock discontinuities with linear schemes is limited to first order approximations. Higher order linear schemes will result in an unstable discretization and the onset of wiggles. The construction of stable, second order (and higher) discretizations, then, requires the adoption of high resolution non-linear schemes which exhibit a total variation diminishing (TVD) [3] behavior. Among them, flux limiters are a mature and robust method, which has been adopted in a diversity of applications. Sweby [4] generalized several limiters and stated the conditions for 2nd order TVD schemes in a 1D homogeneous mesh in its well known *Sweby diagram*. Despite the known inconsistencies that arise when departing from the 1D homogeneous case [5, 6] these techniques have been ported to non-homogeneous Cartesian [6] and unstructured [7] meshes as well. Advances in this field have been also exploited by the multiphase flow community, particularly for the advection of the marker function [8, 9].

Traditionally, both the analysis and the implementation of flux limiters are performed from a stencil-based perspective. However, the growing interest of the community in mimetic methods [10, 11], which inherently preserve the spatial structure of the solution, demands a new approach to flux limiters. Such a family of methods construct discrete operators directly from the inherent incidence matrices that define the mesh. This presents an important advantage both from theoretical and practical points of view, as it is discussed below.

On the one hand, this allows for a flawless discrete mimicking of the continuum operators. In particular, it allows for the exact conservation of important secondary properties, such as kinetic energy [12, 13], among others. On the other hand, the adoption of an algebraic topology approach provides, directly, with a set of algebraic operations which are better suited for both algebraic analysis [14] and computational implementation than its stencil-based counterpart, as it is discussed next.

The advent of parallel heterogeneous architectures has motivated a new demand for portability. From this perspective, the use of a unified approach is desired in order to simplify architecture-oriented implementations to portable ones without a significant lack of performance.

By casting discrete operators into algebraic forms (i.e., matrices and vectors) it has been shown that nearly 90% of the calculations in a typical CFD algorithm for the direct numerical simulation (DNS) and large eddy simulations (LES) of incom-

pressible turbulent flows are comprised of the following: sparse matrix-vector multiplication (`SpMV`), linear combination of vectors (`axpy`) and dot product (`dot`) [15]. This reduces the implementation of numerical codes to the right combination of a few basic operations and provides an opportunity for high-performance computing (HPC) optimization, parallelization and portability [16].

Oyarzun et al. [17] have implemented a conjugate gradient (CG) method following such an operator-based approach. Borrell et al. [18] showed the potential of such approach with the aim of pursuing petascale simulations. In all cases the use of an operator-based formulation has provided with robust, portable and optimized implementations. Consequently, the design of operator-based algorithms for its use in massively parallel architectures is a smart strategy towards the efficient solution of both industrial and academic scale problems [19].

In this paper a flux limiter formulation based on algebraic operations is detailed and its implementation tested on the CPU-based MareNostrum 4 supercomputer at Barcelona Supercomputing Center.

The rest of the paper is organized as follows: In section 3.2 a review of basic chain and graph theory is briefly summarized in order to provide some context. Section 3.3 develops a generalization of flux limiters from an algebraic perspective. Finally, section 3.4 highlights the capabilities of the method in both structured and unstructured meshes.

3.2 Algebraic Topology

By using concepts from algebraic topology, mimetic methods preserve the inherent structure of the space, leading to stable and robust discretizations [11, 20]. However, the development of such techniques is out of the scope of this paper, where we rather focus on exploiting the relationships between the different entities of the mesh for the construction of flux limiters. The interested reader is referred to [10] and references therein.

For whatever space of interest Ω, we can equip it with a partition of unity, namely a mesh M, by bounding the group of cells, C, with faces, F; those with the set of edges, E, and finally those with the set of vertices, V. In this sequence, groups are related to the next element of the sequence by means of the boundary operator ∂. This is know as a chain complex [20, 21]. A 2D example can be seen in Figure 3.1, where face and edges collapse into the same entity.

The relationship between the bounding elements of a geometric entity can be cast in oriented incidence matrices, $T_{E\to V}$, $T_{F\to E}$ and $T_{C\to F}$, corresponding to edge-to-vertex, face-to-edge and cell-to-face, respectively. Conversely, we can define $T_{F\to C}$, $T_{E\to F}$ and $T_{V\to E}$, for the face-to-cell, edge-to-face and vertex-to-edge incidence matrix. In addition, the converse incidence matrices can be seen by transposing such

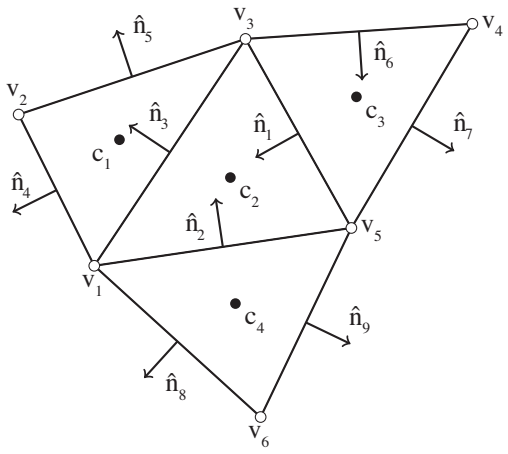

Figure 3.1: 2D mesh composed of cells c_i, which are bounded by faces f_j oriented in the direction $\hat{\boldsymbol{n}}_j$. Faces, which collapse to the same entities as edges, are bounded by the set of vertices v_k.

matrices. The corresponding incidence matrices for the mesh depicted in Figure 3.1 read:

$$T_{F\to V} = \begin{pmatrix} 0 & +1 & +1 & +1 & 0 & 0 & 0 & -1 & 0 \\ 0 & 0 & 0 & -1 & +1 & 0 & 0 & 0 & 0 \\ -1 & 0 & -1 & 0 & -1 & -1 & 0 & 0 & 0 \\ 0 & 0 & 0 & 0 & 0 & +1 & -1 & 0 & 0 \\ +1 & -1 & 0 & 0 & 0 & 0 & -1 & 0 & +1 \\ 0 & 0 & 0 & 0 & 0 & 0 & 0 & +1 & -1 \end{pmatrix}, \tag{3.1}$$

$$T_{C\to F} = \begin{pmatrix} 0 & -1 & +1 & 0 \\ 0 & -1 & 0 & +1 \\ -1 & +1 & 0 & 0 \\ +1 & 0 & 0 & 0 \\ +1 & 0 & 0 & 0 \\ 0 & 0 & -1 & 0 \\ 0 & 0 & +1 & 0 \\ 0 & 0 & 0 & +1 \\ 0 & 0 & 0 & +1 \end{pmatrix}. \tag{3.2}$$

Incidence matrices represent the boundary operator between one element of the chain and the next one. Following the example of Figure 3.1, $T_{F\to C}$ provides with

the orientation of the boundary faces f_j for cell c_i. On the other hand, $T_{V\to F}$ provides with the orientation of the bounding vertices v_k to every face f_j.

Incidence matrices play an essential role in preserving properties of the discrete space. In particular, they form an exact sequence. Exact sequences are those such that the application of the boundary operator twice results in 0. This can be verified by checking $T_{F\to V}T_{C\to F} = 0$. This property is shared by its continuum counterpart, the de Rahm cohomology [11], which is the ultimate responsible of the following vector calculus identities [20]:

$$\nabla \times \nabla \equiv 0, \tag{3.3}$$

$$\nabla \cdot \nabla \times \equiv 0. \tag{3.4}$$

These are powerful identities that mimetic methods preserve by construction. For an extended review of the relationship between the continuum and the discrete counterparts, the reader is referred to [11,20] and references therein.

In addition to provide a suitable platform for the construction of appropriate mimetic methods, the relations contained in incidence matrices can be studied from a graph theory perspective.

A straightforward use of incidence matrices allows to compute differences across faces. The fact that differences lie in a different space (faces) than variables (cells) is an inherent property of such an approach:

$$\Delta \mathbf{u_c} = T_{C\to F}\mathbf{u_c}. \tag{3.5}$$

Particularly useful is the construction of undirected incidence matrices ($B_{Q\to S}$), which are build by taking the absolute value of the elements of the directed ones ($T_{Q\to S}$). Considering the index notation between a generic space Q (e.g., cells, faces) and its boundary S (e.g., faces, edges), we could proceed as follows:

$$B_{Q\to S} = b_{sq} = |e_{sq}|. \tag{3.6}$$

Similarly, one can proceed to compute the degree matrix of the graph, which accounts for the number of connections that an entity has (e.g., the number of cells in contact with a face). Degree matrices are always diagonal and the value of the diagonal elements is obtained as follow:

$$diag(W_{QQ}) = B_{S\to Q}1_S = b_{qs}1_s. \tag{3.7}$$

In particular, undirected incidence matrices can be used to construct suitable shift operators [22]:

$$\Pi_{C\to F} = W_{FF}^{-1}B_{C\to F}. \tag{3.8}$$

This provides with a simple face-centered interpolation, weighted with the number of adjacent faces. Note that by taking this approach, boundaries are inherently included from the graph information.

The use of such $\Pi_{C\to F}$ is restricted to scalar fields. However, following [22], this can be readily extended to vector fields as follows. To do so we shall consider first the discretization of vector fields. First, the discretization of a continuum vector field $\vec{x} = (u, v, w)^T$ is arranged in a single vector as $\tilde{\mathbf{x}}_\mathbf{c} = (\mathbf{u_c}, \mathbf{v_c}, \mathbf{w_c})^T$, where $\mathbf{u_c}$, $\mathbf{v_c}$ and $\mathbf{w_c}$ represent the value of u, v and w at cell c. Note that all components are arranged in a single $\mathbb{R}^{|C|d\times 1}$ column vector, where $|C|$ is the number of cells and d is the number of dimensions of the problem. Next, the interpolator can be extended component-wise by applying the Kronecker product with the identity matrix of size $\mathbb{R}^{d\times d}$. The final ensemble is as follows:

$$\Gamma_{C\to F} = \mathbb{I}_d \otimes \Pi_{C\to F}. \tag{3.9}$$

Similarly, normal vectors can be arranged into a $\mathbb{R}^{|F|\times|F|d}$ matrix by arranging d diagonal matrices, corresponding to every component of the face vector, next to each other as $\mathsf{N}_F = (N_u|N_v|N_w)$ [22]. The N_F matrix corresponding to the mesh depicted in Figure 3.1 reads:

$$\mathsf{N}_F = \begin{pmatrix} n_{1x} & 0 & \dots & 0 & n_{1y} & 0 & \dots & 0 \\ 0 & n_{2x} & \dots & 0 & 0 & n_{2y} & \dots & \vdots \\ \vdots & 0 & \ddots & \vdots & \vdots & 0 & \ddots & \vdots \\ 0 & 0 & \dots & n_{9x} & 0 & 0 & \dots & n_{9y} \end{pmatrix}. \tag{3.10}$$

In such a way, it is straightforward to either project a discrete vector as $\mathsf{N}_F\tilde{\mathbf{x}}_\mathbf{f}$, or to vectorize a scalar quantity as $\mathsf{N}_F^T\mathbf{s_f}$, provided that both are stored at the faces. An accurate discussion about the construction of this matrix can be found in [22].

Other basic matrices derived from the graph are both the graph Laplacian (L_{CC}) and the adjacency matrix (A_{CC}):

$$L_{CC} = B_{F\to C}B_{C\to F}, \tag{3.11}$$

$$A_{CC} = W_{CC} - L_{CC}. \tag{3.12}$$

Both are constructed based on the incidence matrices and provide information about the propagation of information along the graph. They are constructed by connecting cells to its neighbors trough its bounding faces.

In summary, the constructor of such operators provides with tools able to relate different elements of the graph between each others. Equipped with such basic concepts, the development of higher level operators can proceed as in the following section.

3.3 Flux Limiters

The solution of hyperbolic problems in finite volume methods when sharp discontinuities are present requires the use of high resolution schemes in order to attain second order approximations. In turn, the construction of such schemes is reduced to the appropriate reconstruction of the flux at the faces. Prone to introduce numerical instabilities, such a reconstruction requires, in turn, an appropriate flux reconstruction strategy in order to guarantee TVD behavior (i.e., such that no new minima or maxima are introduced). This is attained by limiting the flux at cell's boundaries by means of a flux limiter function.

Typically, flux limited schemes are stated in the following form [4]:

$$\theta_f = \theta_C + \Psi(r)\left(\frac{\theta_D - \theta_C}{2}\right), \tag{3.13}$$

where θ_C and θ_D stand for the centered and downwind values of θ according to the velocity field u and $\Psi(r)$ is the flux limiter function. Figure 3.2 depicts this situation.

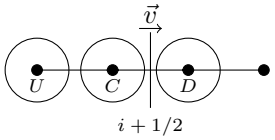

Figure 3.2: Classical stencil for the computation of the gradient ratio at face $i + 1/2$. U, C and D correspond to the upstream, centered and downstream nodes.

From a physical point of view, this is equivalent to the introduction of some sort of artificial diffusion which stabilizes the method at the expense of smearing out its profile. This can be easily seen by restating the classical stencil-based formulation stated in equation (3.13) into:

$$\theta_f = \frac{\theta_C + \theta_D}{2} + \frac{\Psi(r) - 1}{2}\left(\theta_D - \theta_C\right), \tag{3.14}$$

where $(\Psi(r) - 1)/2$ stands for the artificial diffusion added to a classical symmetry-preserving scheme.

The limiting approach has been used by several authors [1, 23], who over the years developed several discontinuity sensors in order to limit dissipation to the region near the shock. Among all discontinuity sensors, the most popular is the use of the gradient ratio. Following Figure 3.2 nomenclature, this is defined as follows [4]:

$$r_f = \frac{\Delta_U \theta}{\Delta_u \theta} = \frac{\theta_C - \theta_U}{\theta_D - \theta_C}, \tag{3.15}$$

where $\Delta_U \theta$ is the gradient of θ at the upwind face while $\Delta_u \theta$ correspond with the gradient at the face of interest. Both differences are taken as positive in the flow direction, defined by the velocity field $\mathbf{u_f}$.

This provides with an intuitive description of where discontinuities are and its order of magnitude, at the time that keeps a compact stencil. In addition, it allows to, after proper manipulation by the flux limiter itself, limit the flux in a way which can be interpreted as a diffusion-like term. This is known as "upwinding" as it has the same effect as recovering the 1st order upwind discretization near shocks.

TVD conditions in terms of the gradient ratio where stated by Harten in 1983 [3] for 1D homogeneous grids. These conditions where used by Sweby in 1984 [4] to state 2nd order *and* TVD conditions for different forms of flux limiters. This idea has been extended, with several degrees of accuracy, to multidimensional and irregular grids [5, 6], among others.

3.3.1 Algebraic Formulation

As stated previously, the discretization of equation (3.14) may benefit from the adoption of an algebraic approach. In this regard, it can be easily extended to the whole computational domain as:

$$\theta_{\mathbf{f}} = (\Pi_{C \to F} + F(r) S(u) \mathsf{E}_{\mathsf{C} \to \mathsf{F}})\, \theta_{\mathbf{c}}, \tag{3.16}$$

where $\theta_{\mathbf{f}} \in \mathbb{R}^{|F|}$ and $\theta_{\mathbf{c}} \in \mathbb{R}^{|C|}$ are the vectors holding all the values of θ_f and θ_c, $\Pi_{C \to F} \in \mathbb{R}^{C \times F}$ is the standard cell-to-face interpolation defined in equation (3.8), $F(r) \in \mathbb{R}^{C \times F}$ is the diagonal matrix absorbing the artificial diffusion introduced in equation (3.14), $S(u) \in \mathbb{R}^{F \times F}$ is the diagonal matrix taking the proper sign of the velocity at the faces and $\mathsf{E}_{\mathsf{C} \to \mathsf{F}}$ takes the difference across them as in equation (3.5).

At this point, we may be tempted to analyze the construction of new flux limiters by means of basic algebra concepts. In particular, to bound its spectrum by means of Gershgorin's theorem or to check its entropy conditions [24], among others. The interested reader is referred to Báez et al. [25], where a similar approach is taken for spatial filters.

While both $\Pi_{C \to F}$ and $\mathsf{E}_{\mathsf{C} \to \mathsf{F}}$ are readily available from the background stated in section 3.2, the construction of $F(r)$ by means of basic algebraic operations solely is addressed next.

Because flux limiter functions $F(r)$ depend only on the local value of $\mathbf{r_f}$ and we defer the details on the implementation of the pointwise operations to section 3.3.2,

the problem is turned into the accurate computation of $\mathbf{r_f}$ at faces. Notwithstanding, we introduce here SUPERBEE [4] as a prototypical flux limiter function.

$$[diag\,(F(r))]_i = \frac{max(0, max(min(1, 2[\mathbf{r_f}]_i), min([\mathbf{r_f}]_i, 2))) - 1}{2}. \tag{3.17}$$

There has been several approaches [5, 7] to the construction of $\mathbf{r_f}$ in terms of a least-squares reconstructed gradient. However, the implementation of such schemes can be cumbersome and may not, eventually, recover the 1D homogeneous solution when a homogeneous structured mesh is used.

The construction of the gradient ratio will proceed first by the separate calculation of both the numerator ($\Delta_U\theta$) and the denominator ($\Delta_u\theta$) of equation (3.15), then computed as:

$$[\mathbf{r_f}]_i = \frac{[\mathbf{d_u}\theta]_i}{[\mathbf{d_U}\theta]_i}, \tag{3.18}$$

where $\mathbf{d_u}\theta \in \mathbb{R}^{|F|}$ is the face-centered vector holding the difference across the face taken in the direction stated by $\mathbf{u_f}$, while $\mathbf{d_U}\theta \in \mathbb{R}^{|F|}$ holds the upstream differences according, again, to $\mathbf{u_f}$.

In this approach we propose to employ symmetry-preserving gradients (see [12]) into the calculation of both face-centered and upstream gradients in order to preserve, as much as possible, the mimetic properties of the approach. In addition, we aim at recovering the Cartesian formulation as in [9].

Before any calculation, the sign matrix ($S(u)$) is constructed by assigning to a $\mathbb{R}^{F\times F}$ diagonal matrix +1 for a positive velocity and -1 for a negative one.

$$[diag\,(S(u))]_i = sign([\mathbf{u_f}]_i). \tag{3.19}$$

This allows for a straightforward calculation of the velocity-oriented gradient at the face as follows:

$$\mathbf{d_u}\theta = S(u)T_{C\to F}\theta_\mathbf{c}, \tag{3.20}$$

where $S(u)$ is used to provide the right direction in which the difference is taken according to the velocity field.

The construction of the upwind difference $\mathbf{d_U}\theta$ is more involved. The idea is to construct a partial adjacency matrix which only considers upstream faces, namely the upstream adjacency matrix, $A^U_{FF}(u)$, which is responsible to garner upstream information and will be defined further in this paper.

We proceed as follows: $\mathsf{E}_{\mathsf{C}\to\mathsf{F}}$ is used to compute the difference across every face according to equation (3.5). In order to asses the contribution of every neighboring face to the face of interest, face differences are vectorized with its corresponding face

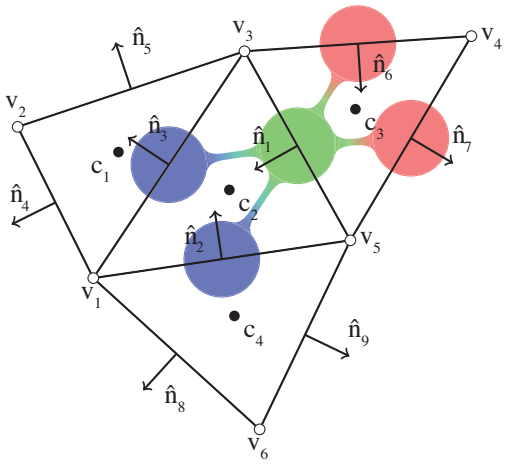

Figure 3.3: Upstream (red) and downstream (green) adjacent faces for face 1 with respect to the positive component of velocity at face 1. The selection of the right ones in $A^U_{FF}(u)$ will ultimately depend on $S(u)$.

normal using N_F^T and added all together with $A^U_{FF}(u)$. Finally, the resulting value is projected over the normal of the face of interest by means of N_F. The overall construction of the operator is then:

$$\mathbf{d_U}\theta = \mathsf{N}_F \left(\mathbb{I}_d \otimes A^U_{FF}(u) \right) \mathsf{N}_F^T \mathsf{E}_{\mathsf{C}\to\mathsf{F}} \theta_{\mathbf{c}}, \tag{3.21}$$

where, similarly to what we did in equation (3.9), we have reused the $A^U_{FF}(u)$ operator for all spatial dimensions. Face normal matrices N_F, defined as in equation (3.10), are used for both vectorization and projection of the neighboring differences. In this way, orthogonal meshes recover the original 1D formulation, whereas unstructured ones are handled inherently by the incidence matrix.

We are now left with construction of the upstream adjacency matrix, $A^U_{FF}(u)$, which may look, at a first glance, of high computational cost. However, it can be assembled from other simpler matrices:

$$A^U_{FF}(u) = \frac{1}{2}\left(A_{FF} - S(u) A^D_{FF} \right), \tag{3.22}$$

where A_{FF} is the face adjacency matrix, A^D_{FF} is a "directed adjacency matrix", which will be introduced below, and $S(u)$ is the already familiar velocity sign matrix. The strategy for the construction of $A^U_{FF}(u)$ is to add the contribution of all neighboring

faces irrespective of the flow direction and then use $S(u)A^D_{FF}$, to remove the downwind ones depending on the values of $S(u)$. Note that both A_{FF} and A^D_{FF} are constant matrices and that the only matrix that needs to be updated according to $\mathbf{u_f}$ is $S(u)$.

The construction of A_{FF} proceeds similarly to equation (3.12) as follows:

$$A_{FF} = W_{FF} - B_{C\to F}B_{F\to C}. \tag{3.23}$$

As seen in section 3.2, the adjacency matrix is symmetric and contains non-negative entries only. Following on the example depicted in Figure 3.3, the corresponding A_{FF} reads:

$$A_{FF} = \begin{pmatrix} 0 & +1 & +1 & 0 & 0 & +1 & +1 & 0 & 0 \\ +1 & 0 & +1 & 0 & 0 & 0 & 0 & +1 & +1 \\ +1 & +1 & 0 & +1 & +1 & 0 & 0 & 0 & 0 \\ 0 & 0 & +1 & 0 & +1 & 0 & 0 & 0 & 0 \\ 0 & 0 & +1 & +1 & 0 & 0 & 0 & 0 & 0 \\ +1 & 0 & 0 & 0 & 0 & 0 & +1 & 0 & 0 \\ +1 & 0 & 0 & 0 & 0 & +1 & 0 & 0 & 0 \\ 0 & +1 & 0 & 0 & 0 & 0 & 0 & 0 & +1 \\ 0 & +1 & 0 & 0 & 0 & 0 & 0 & +1 & 0 \end{pmatrix}. \tag{3.24}$$

On the other hand, the construction of A^D_{FF} allows us to distinguish neighboring faces which lie, according to the face normal, behind or ahead of the face in question. This requires the inclusion of the directed incidence matrix $T_{C\to F}$ into the calculation of the adjacency matrix as:

$$A^D_{FF} = T_{C\to F}B_{F\to C}, \tag{3.25}$$

which provides with the following matrix:

$$A^D_{FF} = \begin{pmatrix} 0 & +1 & +1 & 0 & 0 & -1 & -1 & 0 & 0 \\ +1 & 0 & +1 & 0 & 0 & 0 & 0 & -1 & -1 \\ -1 & -1 & 0 & +1 & +1 & 0 & 0 & 0 & 0 \\ 0 & 0 & -1 & 0 & -1 & 0 & 0 & 0 & 0 \\ 0 & 0 & -1 & -1 & 0 & 0 & 0 & 0 & 0 \\ +1 & 0 & 0 & 0 & 0 & 0 & +1 & 0 & 0 \\ -1 & 0 & 0 & 0 & 0 & -1 & 0 & 0 & 0 \\ 0 & -1 & 0 & 0 & 0 & 0 & 0 & 0 & -1 \\ 0 & -1 & 0 & 0 & 0 & 0 & 0 & -1 & 0 \end{pmatrix}. \tag{3.26}$$

Note that A^D_{FF} has the same pattern as A_{FF} but entries corresponding to faces located upstream (with respect to the face normal direction) contain -1 whereas those located downstream contain $+1$, as shown in Figure 3.3.

However, the choice of upstream/downstream faces should depend on the faces local velocity and not on its arbitrary choice of face normal. The product $S(u)A_{FF}^{D}$, corrects this by inverting the sign of the rows corresponding to the faces whose velocity component is not aligned with the face normal. The result is a correct choice of upstream and downstream faces according to the local face velocity.

Finally, the combination of A_{FF}^{D} and A_{FF} in equation (3.21) results in:

$$\mathbf{d_U}\theta = \mathsf{N}_F \left(\mathbb{I}_d \otimes \frac{1}{2} \left(S(u) A_{FF}^{D} - A_{FF} \right) \right) \mathsf{N}_F^T \mathsf{E}_{\mathsf{C}\to\mathsf{F}} \theta_{\mathbf{c}}. \tag{3.27}$$

3.3.2 Algebraic Implementation

While equation (3.27) succeeds at selecting the proper upstream faces, its direct implementation involves many redundant operations that may result in an unnecessary overhead. For this reason, the computation of $\mathbf{d_U}\theta$ is rearranged as follows:

$$\mathbf{d_U}\theta = \left(S(u)\mathsf{UUD}_{C\to F} + \mathsf{OUD}_{C\to F} \right) \theta_{\mathbf{c}}, \tag{3.28}$$

where we introduce the new matrices $\mathsf{UUD}_{C\to F} = \frac{1}{2}\mathsf{N}_F \left(\mathbb{I}_d \otimes A_{FF}^{D} \right) \mathsf{N}_F^T \mathsf{E}_{\mathsf{C}\to\mathsf{F}}$ and $\mathsf{OUD}_{C\to F} = \frac{1}{2}\mathsf{N}_F \left(\mathbb{I}_d \otimes A_{FF} \right) \mathsf{N}_F^T \mathsf{E}_{\mathsf{C}\to\mathsf{F}}$, which can be computed and stored before the start of the simulation and consequently reused.

Note that because we are actually interested in the evaluation of $\mathbf{d_U}\theta$ rather than in the construction of the operator itself, matrix-matrix products can be avoided if successive matrix-vector products are performed.

The final algorithm for the deployment of a flux limiter in the advection of a scalar within our algebra-based framework is described in Algorithm 1.

In previous works of Oyarzun et al. [15] and Álvarez et al. [26], a portable implementation model for DNS and LES of incompressible turbulent flows was proposed such that the time-integration algorithm reduces to a set of only three linear algebra operations: the sparse matrix-vector product, the linear combination of vectors and the dot product. However, a close look to Algorithm 1 reveals that this set is insufficient to fulfill the flux limiter implementation because it comprises non-linear operations (e.g., a pointwise division is required for computing the gradient ratio as in Step 4, or a reduction to get the minimum value for the CFL in Step 7).

Nevertheless, instead of being an inconvenience, this encourages us to demonstrate the high potential of our algebra-based implementation strategy again. On the one hand, the generalization of the `axpy` kernel via the introduction of a binary operator (i.e., an operator that combines two elements of a vector space to produce another element), `kbin`, that performs any given pointwise arithmetic calculation is sufficient to embed the algebraic flux limiter into our fully-portable, algebra-based

Algorithm 1 Algorithm for the advection of a scalar field using an algebraic implementation of the SUPERBEE flux limiter

1. Compute the matrix $S(u)$ as:
   $[diag\,(S(u))]_i = sign([\mathbf{u_f}]_i)$.
2. Compute the vector $\mathbf{d_u}\theta$ as:
   $\mathbf{d_u}\theta = S(u)\mathsf{E}_{\mathsf{C}\to\mathsf{F}}\theta_{\mathbf{c}}$.
3. Compute the vector $\mathbf{d_U}\theta$ as:
   $\mathbf{d_U}\theta = (S(u)\mathsf{UUD}_{C\to F} + \mathsf{OUD}_{C\to F})\,\theta_{\mathbf{c}}$.
4. Compute the vector $\mathbf{r_f}$ as:
   $[\mathbf{r_f}]_i = [\mathbf{d}\theta_{\mathbf{U}}]_i / [\mathbf{d}\theta_{\mathbf{u}}]_i$.
5. Compute the matrix $F(r)$ as:
   $[diag(F(r))]_i = 0.5\,(max(0, max(min(1, 2[\mathbf{r_f}]_i), min([\mathbf{r_f}]_i, 2))) - 1)$.
6. Compute the advected field $\mathsf{C}(\mathbf{u_f})\theta_c$ as:
   $\mathsf{C}(\mathbf{u_f})\theta_c = \mathsf{DU}_f\,(\Pi_{C\to F} + F(r)S(u)\mathsf{E}_{\mathsf{C}\to\mathsf{F}})\,\theta_{\mathbf{c}}$.
7. Calculate a dt satisfying the CFL condition:
   $dt = C\left(min\left(|[\mathbf{u_f}]_0| / [\mathbf{d_f}]_0, ..., |[\mathbf{u_f}]_{|F|}| / [\mathbf{d_f}]_{|F|}\right)\right)$.

framework. On the other hand, the substitution of the `dot` kernel by a generic reduction operator, `kred`, that calculates the specified reduced value (e.g., minimum, maximum, addition or product).

This generalization does not alter the computational behavior in comparison with the original `axpy` kernel as it still performs simple, pointwise arithmetic operations over the vector elements (i.e., there is no need for communications in distributed-memory parallelization) and provides uniform, aligned memory access with coalescing memory transactions which suit the stream processing paradigm perfectly. Therefore, having already efficient OpenMP, OpenCL and CUDA implementations of `axpy`, the implementation of `kbin` kernel is straightforward (e.g., it can be easily extended via including a function pointer as a parameter in the former).

On the other hand, the arithmetic intensity (AI) of this new kernel (*i.e.* the ratio of computing work in floating-point operations (FLOPs) to memory traffic in bytes) is not a fixed value anymore, as shown in Table 3.1. While the arithmetic intensity of the `axpy` was 1/12 FLOPs per byte (one product and one addition per three 8-byte values), than of the `kbin` will depend on the specific arithmetic calculation required by the function in each call. This allows us to significantly increase the arithmetic

intensity in our calls by means of kernel-fusion and thus reduce the time-to-solution.

Table 3.1: Analysis of the arithmetic intensity of the different functions given to `kbin` kernel during the execution of the Algorithm 1. The functions correspond to: 1) the linear combination of vectors, 2) the pointwise sign operator, 3) the pointwise division operator and 4) the pointwise SUPERBEE flux limiter operator.

Function	AI
$y = y + ax$	1/12
$y = x < 0? -1 : +1$	1/16
$y = ay/x$	1/12
$y = 0.5(max(0, max(min(1, 2x), min(x, 2))) - 1)$	7/16

In conclusion, the evaluation of the advection as in Algorithm 1 using our framework is comprised of only three computing kernels: `SpMV`, `kbin` and `kred`. The number of calls in each step of the algorithm is stated in Table 3.2. This results in a compact algorithm, which facilitates portability by reducing the number of computing kernels involved, and simplifying them. As it can be seen, the computation of several local quantities is required in order to construct the final algebraic scheme.

Table 3.2: Number of operations count for Algorithm 1.

Step	`SpMV`	`kbin`	`kred`
1. $S(u)$	0	1	0
2. $\mathbf{d_U}\theta$	3	1	0
3. $\mathbf{d_u}\theta$	2	0	0
4. $\mathbf{r_f}$	0	1	0
5. $F(r)$	0	1	0
5. $\mathsf{C}(\mathbf{u_f})\theta_c$	4	1	0
5. dt	0	1	1
total	9	6	1

Finally, note that the implementation of different flux limiter functions would only affect the values in the diagonal of $F(r)$.

3.3.3 Comparison with the stencil-based approach

The new approach for the proper construction of gradient ratios is now compared with the classical, stencil-based approach.

In a general, 1D case for a Cartesian homogeneous grid, the computation of the gradient ratio, r, involves the use of, at least, 3 nodes trough a face located at $i +$

1/2. Depending on whether the velocity is going in one direction or another, the definition of the upstream nodes will change accordingly. This can be exemplified in Figure 3.4.

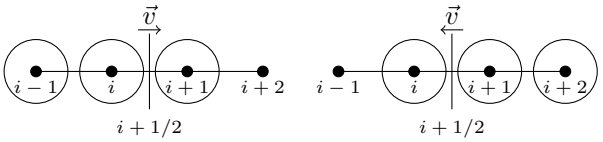

Figure 3.4: Example of stencils in 1D according to the classical flux limiter approach. The stencil topology is not constant and changes according to the sign of the velocity field $\vec{v}$.

The use of the proposed algebraic approach apparently involves a larger stencil, as it can be seen in Figure 3.5. However, the computation of the proper upstream adjacency matrix $A^U_{FF}(u)$ according to equation (3.22) will result in the appropriate stencil (i.e., the portrait of the sparse matrix) for $A^U_{FF}(u)$.

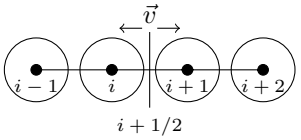

Figure 3.5: Equivalent stencils used in the computation of an algebraic flux limiter. In this case the adjacency matrices involve the operation with all neighboring nodes.

In comparison with the stencil-based, the algebra-based implementation is very similar regarding parallelization. The distributed-memory parallelization remains the same since the size of the *halo* (*i.e.,* the elements from other computing units which are coupled with the own elements [27]) depends directly on the partitioning of the computational domain. On the other hand, the stencil-based approach could appear to be slightly more efficient regarding the memory traffic in some numerical schemes as they can make use of specialized kernels that require less intermediate results, or discriminate some operations with conditional statements, for instance when locating upwind values. However, these specializations may harm the coalescence of memory transactions, which is very important in some parallel paradigms such as stream processing, and thus reduce the relative performance which, in our framework, is near the maximum theoretical performance given by the memory bound.

3.4 Numerical Results

Next, the application of this technique is applied to a canonical case. In particular, the advection of a sharp profile has been tested on unstructured, hex-dominant meshes of 373, 2,985, 23,887 and 80,621 thousand cells. The sharp profile is initialized in a physical domain of $[0,1] \times [0,1] \times [0,1]$ as a sphere of radius $r = 0.15$, located at $(0.35, 0.35, 0.35)$ and subject to a divergence free velocity field:

$$u = 2sin^2(\pi x)sin(2\pi y)sin(2\pi z)cos(\pi t/T), \tag{3.29}$$

$$v = -sin(2\pi x)sin^2(\pi y)sin(2\pi z)cos(\pi t/T), \tag{3.30}$$

$$w = -sin(2\pi x)sin(2\pi y)sin^2(\pi z)cos(\pi t/T), \tag{3.31}$$

$$\tag{3.32}$$

during 3.0 time-units, T. The results of the profile are shown in Figure 3.6 for the slices in $x = 0.35$, $y = 0.35$ and $z = 0.35$ planes.

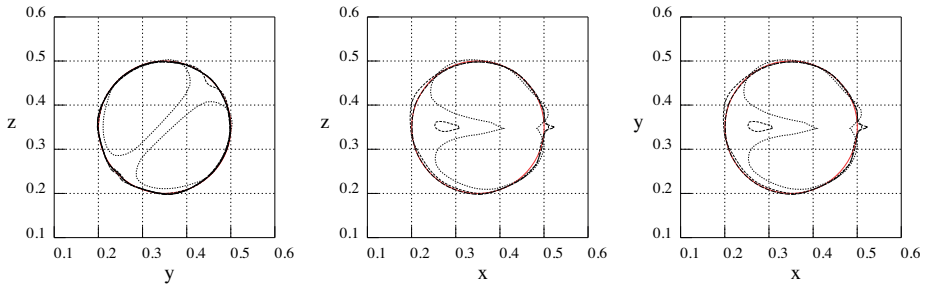

Figure 3.6: Contours for $\theta = 0.5$ in $x = 0.35$, $y = 0.35$ and $z = 0.35$ planes after 3.0 time-units. For meshes of 373, 2,985, 23,887 and 80,621 thousand cells.

Computations are performed on up to 3,072 cores of the CPU-based MareNostrum 4 supercomputer at the Barcelona Supercomputing Center. Its nodes with two Intel Xeon 8160 CPUs (24 cores, 2.1 GHz, 6 DDR4-2666 memory channels, 128 GB/s memory bandwidth, 33 MB L3 cache) are interconnected through the Intel Omni-Path network (12.5 GB/s). The HPC^2 [19], our numerical framework designed for the efficient computation of basic algebraic operations in modern supercomputers, achieves a sustained performance of up to 1.6 TFLOPS, which corresponds to nearly 80% of the maximum theoretical performance (recall that this algorithm is memory bound). Details of the implementation and a detailed performance and scalability analysis on different types of supercomputing facilities can be found in Álvarez et al. [27].

In Figure 3.7, the temporal evolution of the sphere is shown. In this case, a mesh of 191,102 thousand cells has been chosen. The entire execution of the Algorithm 1 relies on three computing kernels as described in Section 3.3. The share of the computational cost among these kernels during the solution of the algorithm on MareNostrum 4 supercomputer is shown in Figure 3.8: sparse matrix-vector product, pointwise binary kernel and reduction kernel take 71.1%, 26.3% and 2.6% of the time, respectively.

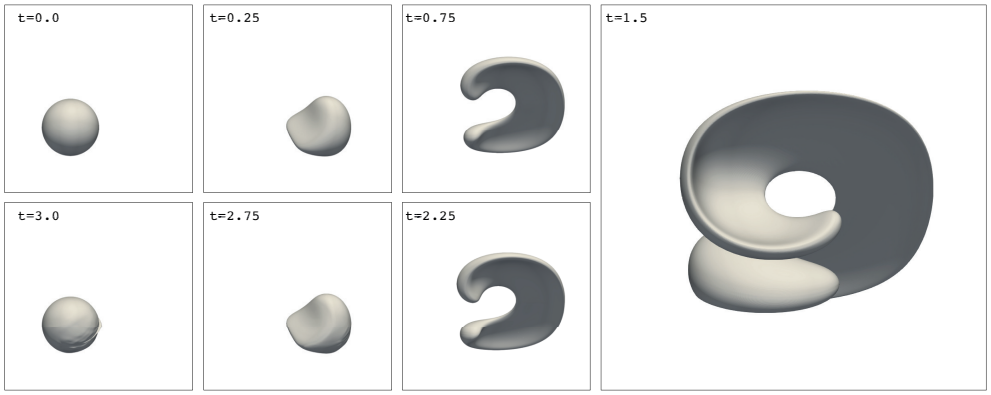

Figure 3.7: Time evolution of the $\theta = 0.5$ contour for $t = 0$, 0.25, 0.75, 1.5, 2.25, 2.75 and 3.0 time-units.

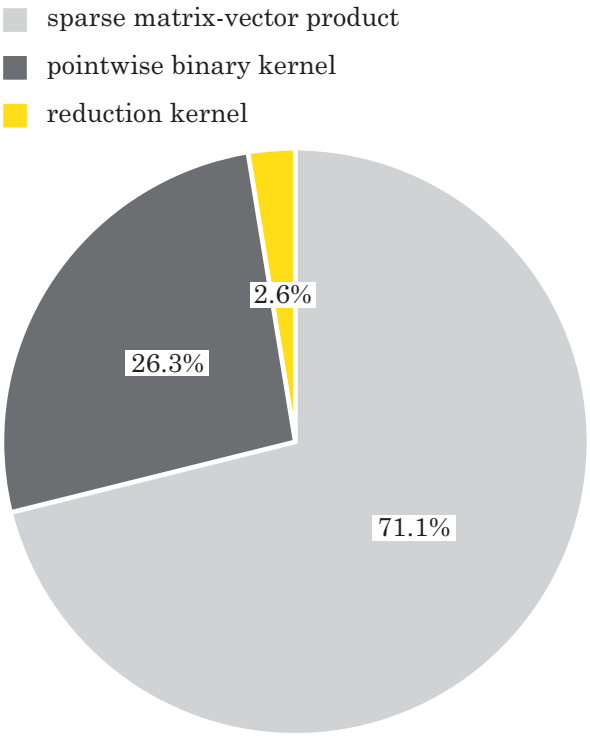

Figure 3.8: Share of the computational workload among the HPC^2 kernels on the solution of Algorithm 1

3.5 Conclusions and Future Work

A flux limiter scheme has been formulated from an algebraic perspective. This results in a compact formulation that allows for an easy implementation on different heterogeneous architectures.

Graph incidence matrices (both directed and undirected) are exploited to construct appropriate gradient ratios. The face velocity sign determines the appropriate side to pick the upstream information. After the sign operation, the remaining operations are all of them either linear or local.

This approach presents several advantages. First of all, casting a flux limiter in algebraic form enhances a higher level of analysis, which has not been considered in this paper. On the other hand, the deployment of such an algebraic form into an heterogeneous computing system reduces the number of computing kernels that need

to be ported from one architecture to the other, enhancing portability and improving code development and maintenance.

Regardless the inconsistencies that where already highlighted in sections 3.1 and 3.3, the resulting implementation provides with accurate results and collapses to the traditional approach of Sweby [4,7,9] when a homogeneous, Cartesian grid is used.

The approach developed in this work can be improved to include the effect of the non-homogeneous distance across upstream faces or its surface in the calculation of the upstream gradient.

3.6 Acknowledgments

The work has been financially supported by the *Ministerio de Economía y Competitividad*, Spain (ENE2017-88697-R and ENE2015-70672-P). N. V. is supported by a *FI AGAUR* predoctoral contract (2018FI_B1_000109). X. Á. is supported by a *FI AGAUR* predoctoral contract (2018FI_B1_00081). F. X. T. is supported by a *Ramón y Cajal* postdoctoral contract (RYC-2012-11996).

References

[1] C. Hirsch. *Numerical computation of internal and external Flows. Vol. 2: Computational Methods for Inviscid and Viscous Flows*. Wiley-Interscience, 1990.

[2] S. Godunov. A difference method for numerical calculation of discontinuous solutions of the equations of hydrodynamics. *Mat. Sb.*, 47(271):271–306, 1959.

[3] Ami Harten. High resolution schemes for hyperbolic conservation laws. *J. Comput. Phys.*, 49(3):357–393, 1983.

[4] P. K. Sweby. High Resolution Schemes Using Flux Limiters for Hyperbolic Conservation Laws. *SIAM J. Numer. Anal.*, 21(5):995–1011, oct 1984.

[5] Marsha Berger, Michael J Aftosmis, and Scott M Murman. Analysis of Slope Limiters on Irregular Grids. Technical report, 2005.

[6] Xianyi Zeng. A General Approach to Enhance Slope Limiters in MUSCL Schemes on Nonuniform Rectilinear Grids. *SIAM J. Sci. Comput.*, 38(2):A789–A813, 2016.

[7] M. S. Darwish and F. Moukalled. TVD schemes for unstructured grids. *Int. J. Heat Mass Transf.*, 46(4):599–611, 2003.

[8] Elin Olsson and Gunilla Kreiss. A conservative level set method for two phase flow. *J. Comput. Phys.*, 210(1):225–246, nov 2005.

[9] N. Balcázar, L. Jofre, O. Lehmkuhl, J. Castro, and J. Rigola. A finite-volume/level-set method for simulating two-phase flows on unstructured grids. *Int. J. Multiph. Flow*, 64:55–72, may 2014.

[10] Konstantin Lipnikov, Gianmarco Manzini, and Mikhail Shashkov. Mimetic finite difference method. *J. Comput. Phys.*, 257(PB):1163–1227, 2014.

[11] R.R. Hiemstra, D Toshniwal, R.H.M. Huijsmans, and M.I. Gerritsma. High order geometric methods with exact conservation properties. *J. Comput. Phys.*, 257:1444–1471, jan 2014.

[12] R. W. C. P. Verstappen and A. E. P. Veldman. Symmetry-preserving discretization of turbulent flow. *J. Comput. Phys.*, 187(1):343–368, 2003.

[13] F. X. Trias. *Direct numerical simulation and regularization modelling of turbulent flows on loosely coupled parallel computers using symmnetry-preserving discretizations*. PhD thesis, Universitat Politècnica de Catalunya, dec 2006.

[14] F. X. Trias, A. Gorobets, and A. Oliva. A simple approach to discretize the viscous term with spatially varying (eddy-)viscosity. *J. Comput. Phys.*, 253:405–417, 2013.

[15] Guillermo Oyarzun, Ricard Borrell, Andrey Gorobets, and Assensi Oliva. Portable implementation model for CFD simulations. Application to hybrid CPU/GPU supercomputers. *Int. J. Comut. Fluid Dyn.*, 31(9):396–411, 2017.

[16] Freddie David Witherden. *On the Development and Implementation of High-Order Flux Reconstruction Schemes for Computational Fluid Dynamics by*. PhD thesis, Imperial Collefe London, 2015.

[17] G. Oyarzun, R. Borrell, A. Gorobets, and A. Oliva. MPI-CUDA sparse matrix–vector multiplication for the conjugate gradient method with an approximate inverse preconditioner. *Comput. Fluids*, 92:244–252, 2014.

[18] R. Borrell, J. Chiva, O. Lehmkuhl, I. Rodríguez, and A. Oliva. Evolving Termofluids CFD Code Towards Peta-Scale Simulations. In *27th Int. Conf. Parallel Comput. Fluid Dyn.*, pages 1–8, 2015.

[19] X. Álvarez, A. Gorobets, F. X. Trias, R. Borrell, and G. Oyarzun. HPC2—A fully-portable, algebra-based framework for heterogeneous computing. Application to CFD. *Comput. Fluids*, 173:285–292, sep 2018.

[20] Nicolas Robidoux and Stanly Steinberg. A discrete vector calculus in tensor grids. *Comput. Methods Appl. Math.*, 11(1):23–66, 2011.

[21] Enzo Tonti. Why starting from differential equations for computational physics? *J. Comput. Phys.*, 257(PB):1260–1290, jan 2014.

[22] F. X. Trias, O. Lehmkuhl, A. Oliva, C. D. Pérez-Segarra, and R. W. C. P. Verstappen. Symmetry-preserving discretization of Navier–Stokes equations on collocated unstructured grids. *J. Comput. Phys.*, 258:246–267, feb 2014.

[23] C. Hirsch. *Numerical Computation of Internal and External Flows. Vol. 1: Fundamentals of Numerical Discretization*. Wiley-Interscience, Brussels, 1988.

[24] Stanley Osher and Sukumar Chakravarthy. High Resolution Schemes and the Entropy Condition. Technical report, 1984.

[25] A. Báez Vidal, O. Lehmkuhl, F. X. Trias, and C. D. Pérez-Segarra. On the properties of discrete spatial filters for CFD. *J. Comput. Phys.*, 326(4):474–498, dec 2016.

[26] Xavier Álvarez, Andrey Gorobets, and F. Xavier Trias. Strategies for the heterogeneous execution of large-scale simulations on hybrid supercomputers. In *Proc. 6th Eur. Conf. Comput. Mech. Solids, Struct. Coupled Probl. ECCM 2018 7th Eur. Conf. Comput. Fluid Dyn. ECFD 2018*, number June, pages 2021–2031, 2018.

[27] Xavier Álvarez-Farré, Andrey Gorobets, and F. Xavier Trias. A hierarchical parallel implementation for heterogeneous computing. Application to algebra-based CFD simulations on hybrid supercomputers. *Comput. Fluids*, 214, 2021.

4

DNS methods for vertical falling films.

Contents of this chapter are partially published in:

N. Valle, F.X. Trias, J. Castro. Energy preserving multiphase flows: application to falling films. *14th World Congress on Computational Mechanics. ECCOMAS., 2021*

And provided here self-contained.

Abstract. The Direct Numerical Simulation of multiphase flows is presented in the context of a film flowing down a vertical plate. The characteristic instabilities of this particular configuration are approached by adopting a symmetry-preserving formulation. Such and approach requires the adoption of novel discretization techniques of both convective and capillary terms, which result in a fully energy-preserving scheme.

The cases presented here approximate the working conditions of a LiBr absorption chiller. Results show the appearance of humps and instabilities, which may enhance heat and mass transfer phenomena.

The numerical simulation of multiphase flows presents several challenges from a modeling perspective, namely the capture of a moving interface and the proper calculation of curvature are relevant obstacles to include surface tension effects. In addition, the inclusion of the aforementioned within a physics-compatible framework presents a major challenge within multiphase computational methods. Namely, the imbalance between kinetic and elastic energy in the presence of surface tension is an open question and prone to numerical instabilities.

4.1 Introduction

The vertical falling film is a canonical flow configurations which is inherently unstable even at $Re = 0$. When surface tension is present, the dynamics of such a system turn even more complex and interesting. Its application is of interest for many industrial applications in which high heat and mass transfer coefficients are expected with low temperature jumps. These include heat exchangers used in desalination and gas absorbers, like HCl absorbers used in chlorination processes and, most remarkably, $H_2O - LiBr$ absorption chillers. While inherently a coupled fluid and thermal dynamic problem, this work is focused on the implementation of Direct Numerical Simulation (DNS) techniques for tackling vertical falling films hydrodynamics in a $H_2O/LiBr$ absorber. The ultimate goal is to gain understanding on the instabilities appearing on this flow as a keystone to approach the heat and mass transfer processes in subsequent steps. In this regard, while the vapor phase has little effect in the fluid dynamics, it plays a key role when considering heat and mass transfer, in addition to ruling other non-linear phenomena such as the transport of volatile surfactant.

The unstable nature of this kind of flow has captured the interest of many, although its inherently unstable behavior was not always clear. The pioneering work of the Kapitza family [1] came along with remarkable experiments and thermodynamic equilibrium theory. That said theory stated a balance between viscous dissipation and gravitational energy transfers, which suggested stability of vertical falling films at sufficiently small Reynolds numbers [2]. However, debates between Yih [3,4] and Benjamin [5] in terms of the linear stability theory of vertical falling films refuted the thermodynamic theory developed by the Kapitza's and confirmed instability of such a flow configuration at any Reynolds number [2]. A linear stability analysis of cylindrical falling films was later introduced by Solorio [6].

The characteristics of such instabilities was reported in the experiments of Nosoko et al. [7], who characterized $2D$ instabilities in falling films with a prescribed excitation frequency. C.D. Park and Nosoko [8] reported horseshoe shaped perturbations along leading capillary ripples at $Re > 40$ and also assessed its mass transfer characteristics in the range $20 < Re < 900$. Miyara et al. [9] reported mass transfer coefficient for cylindrical falling films for $0 < Re < 80$. In the context of $LiBr/H_2O$ absorption chillers, S-B. Park and Lee [10] reported heat and mass transfer enhancements by including additional surfactants, which promoted Marangoni convection in the presence. Additive enhancement in $LiBr/H_2O$ absorbers was also the focus of the work of Cheng et al. [11], who introduced a semi-empirical equation for the enhancement obtained with the respective additives. Garcia-Rivera et al. [12] also found that the inclusion of a wavy model was key to explain the experimental data. Alekseenko et al. [13] assessed $3D$ instabilities at $1.25 < Re < 4.7$, and later on the wave formation in annular gas-liquid flows [14], while the experiments of Khar-

malov [15] shed light into the transition form $2D$ to $3D$ instabilities. In the particular case of vertical films, recent studies of Akesjo [16] has focused on the development of engineered surfaces that enhance flow instabilities and promote heat and mass transfer.

In the computational front, simulations of Nave et al. [17] replicated the experiments of Nosoko et al. [8] by using a ghost fluid - level set method and showed potential to capture flows transitioning from $2D$ to $3D$. The dominant role of inertia in governing the surface waves [2] has been studied by Denner et al. [18, 19], who performed remarkable experimental and numerical work, including the development of new numerical techniques [20–22]. The dispersion of capillary waves was studied by Pradas et al. [23] and also Denner [24]. The role of capillary flow separation at increasing heat and mass transfer characteristics was assessed by Dietze and Kneer [25] from both experimental and numerical results, bolstering the role of surface tension at promoting heat and mass transfer in this flow configuration. Mass transfer enhancement at the capillary waves region was also confirmed by Bo et al. [26] in their $2D$ simulation of a $H_2O/LiBr$ absorber at $Re = 100$. Similarly, the work of Albert et al. [27] performed numerical simulations in order to asses the heat and mass transfer characteristics of falling films, which confirmed, again, the role of flow separation for the enhancement of such phenomena. The study of $3D$ structures in Dietze et al. [28] also observed flow separation. The assessment of corrugations and its impact in heat and mass transfer phenomena was also assessed by Dietze [29] for $Re = 15$.

In addition to the already mentioned complex dynamics of such a flow, $H_2O/LiBr$ absorbers operate at very low pressures ($\sim 1000\ Pa$) [30] and hence operate with a rarefied vapor. In turn, the vapor shows an extremely low density, which results in an extreme density ratio and consequently extremely delicate dynamics. The resulting working conditions are not only difficult to attain experimentally but also numerically [12].

In this context, the assessment of inertia and capillary terms, which rule the flow instabilities that promote heat and mass transfer, is of relevance for the development of new $H_2O/LiBr$ absorbers. Nonetheless, the adoption of physically inconsistent schemes is customary for both convective and capillary terms. Accentuated by the high density ratios, this leads to inaccurate results and even numerical instabilities that compromise the accurate solution of the system. This highlights, once again, the importance of physics-compatible discretizations.

While the symmetry-preserving ideas [31, 32] have been in place for quite some time for the numerical simulation of turbulent flows, the adoption of this approach to multiphase flows has lacked behind. The simulation of multiphase flows in a fully physics-compatible way implies the conservation of discrete primary quantities (i.e., mass and momentum) and also secondary ones (i.e., mechanical energy) according

to the physics described in the continuum. Two major obstacles prevent us from this: the inclusion of surface tension and the advection of a varying density flow.

Regarding the inclusion of surface tension, and its impact on momentum and energy, Fuster [33] developed on top of a Volume Of Fluid (VOF) method a discretization focusing on preserving the (skew-)symmetry of the operators involved, albeit overlooked surface tension, which is know to introduce spurious oscillations that may eventually lead to the divergence of the numerical simulation [34]. In the context of the level set method, our previous work resulted in the inclusion of curvature in an energy-preserving fashion [35], while the conservation of energy is still elusive, a well known issue for diffuse interface flows [36]. Within phase-field methods, the pioneering work of Jacqmin [37] included surface tension in a consistent way in the context of the Cahn-Hilliard equation, while Jamet et al. [38] and Jamet and Misbah [39] did the same in the Allen-Cahn framework. Phase-field methods success at capturing surface tension transfers between potential (elastic) and kinetic energy rely on taking the gradient of a surface potential, while VOF and level set methods aim at treating the usual curvature form.

The inclusion of a density-varying flow was tackled by Rudman [40] in the context of VOF by adopting a consistent mass and momentum transport scheme, which was focused on the simulation of multiphase flow with large density ratios. This approach was also adopted by Raessi and Pitch [41] and Ghods and Hermann [42] within the level-set method, while the work of Mirjalili and Mani [43] presented no only a consistent mass and momentum transport scheme, but also an energy-preserving scheme in the context of phase-field methods.

In this work, the framework of the well-known (mass) Conservative Level-Set method [44] is adopted for capturing the moving interface. Base on the energy-preserving level set method introduced in [35], we produce a fully energy-preserving method for multiphase flows by including a consistent mass and momentum transport as in Mirjalili and Mani [43]. Equipped with such a physics-compatible discretization, we target DNS of vertical falling films within the working conditions of an industrial $H_2O/LiBr$ absorption chiller.

The rest of the chapter is organized as follows: in section 4.2 the governing equations are introduced, in section 4.3 the numerical method is detailed, while in section 4.4 the cases under consideration are introduced and the results commented. Finally, in section 4.5 conclusions are drawn and future developments sketched.

4.2 Mathematical model

The subtle physical equilibrium at which the fluid system is subject calls for a careful, and thus conservative, formulation of the governing equations.

The interface separating the two phases is modeled implicitly by means of a

marker function $\theta \in [0,1]$ which can be regularized as needed, as will be discussed in next chapter. The values $\theta = 0$ indicate the liquid phase, $\theta = 1$ corresponds with the gaseous one and $\theta = 0.5$ with the interface location. For a sufficiently well-behaved θ, the interface normal is defined as

$$\hat{\eta}_i = \frac{\nabla\theta}{|\nabla\theta|} \tag{4.1}$$

while the interface curvature is defined as

$$\kappa = \nabla \cdot \hat{\eta}_i \tag{4.2}$$

Note that when the marker function is the distance function, $|\nabla\theta| = 1$ and thus $\hat{\eta}_i = \nabla\theta$.

The flow is assumed incompressible for both liquid and gaseous phases

$$\nabla \cdot \vec{u} = 0 \tag{4.3}$$

under this assumption, the marker function obeys the following transport equation

$$\frac{\partial\theta}{\partial t} + \nabla \cdot (\vec{u}\theta) = 0 \tag{4.4}$$

while the momentum transport is ruled by the conservative version of the dimensionless Navier-Stokes equations. Exploiting the Nusselt flat film solution (see Appendix B for details) we introduce Reynolds (Re) and Weber (We) numbers. Additionally, because we are concerned with the solution of both liquid and gaseous phases simultaneously, we introduce density ($\Pi_\rho = \rho_g/\rho_l$) and viscosity ($\Pi_\mu = \mu_g/\mu_l$) ratios. Accordingly, we consider the non-dimensional versions of density ($X_\rho = \rho/\rho_l \in [1, \Pi_\rho]$) and viscosity ($X_\mu = \mu/\mu_l \in [1, \Pi_\mu]$). We finally end up with the following momentum equation

$$3Re\left(\frac{\partial\left(X_\rho\vec{u}\right)}{\partial t} + \nabla \cdot \left(X_\rho\vec{u} \otimes \vec{u}\right)\right) = -\nabla p + \nabla \cdot 2X_\mu S + X_\rho\hat{g} \tag{4.5}$$

subject to capillary forces at the interface, which impose a stress discontinuity, $[\sigma]$ as

$$[\sigma]\,\hat{\eta}_i = -We\kappa\hat{\eta}_i \tag{4.6}$$

being $\sigma = -p\mathbb{I} + \mu S$ the stress tensor, $S = 1/2\left(\nabla\vec{u} + (\nabla\vec{u})^T\right)$ the strain tensor and $\hat{g} = (0, -1, 0)$.

Which introduce the following dimensionless parameters

$$Re = \frac{\rho_l u_N h_N}{\mu_l} \tag{4.7}$$

$$We = \frac{\gamma}{\rho_l u_N h_N^2} \tag{4.8}$$

being h_N the undisturbed film thickness and u_N the mean liquid velocity. Details can be found in Appendix B.

The domain under consideration is assumed to be periodic in both y and z directions, while solid walls are present in the x direction. In a symmetric setup with respect to the x mid-plane, there is a film flowing down each wall.

No-slip velocity

$$\vec{u}|_{wall} = 0 \tag{4.9}$$

and no marker flow

$$\nabla\theta \cdot \hat{n}|_{wall} = 0 \tag{4.10}$$

are prescribed at both solid walls.

The interface is initialized as in Dietze et al. [28] by prescribing a perturbation at the film surface as

$$h = h_N \left(1 + \epsilon_y cos\left(2\pi \frac{y}{\Lambda_y}\right) + \epsilon_z cos\left(2\pi \frac{z}{\Lambda_z}\right)\right) \tag{4.11}$$

where h is the perturbed film thickness, $\epsilon_y = 0.2$ and $\epsilon_z = 0.05$ are chosen according to Dietze et al. [28] and correspond with amplitude of the perturbation in the y and z directions, respectively. The wavelength Λ_y and Λ_z are sufficiently large to represent long-wave perturbations [2].

The velocity profile is initialized to the undisturbed flat falling film solution. Details can be found on Appendix B.

4.3 Numerical Method

4.3.1 Regularization

The numerical resolution of equations (4.3-4.6) aims at providing an accurate and reliable approximation. However, the adoption of an Eulerian-Eulerian framework for tracking the moving interface introduce the need of regularization to: *i)* transport sharp discontinuities within the domain and *ii)* map equations formulated in a Lagrangian framework into an Eulerian one. For these reasons, before proceeding to the discretization and numerical integration of the aforementioned equations, we need to take a regularization process which will, eventually, result in a more amenable set of equations. It is shown how this regularization preserve mass, momentum (up to capillarity) and energy equations properties.

The numerical integration of equation (4.4) requires from a proper regularization in order to avoid the appearance of spurious oscillations. This smoothing of the marker function removes the concept of sharp interface, and replaces it by a diffuse

transition region between $\theta = 0$ and $\theta = 1$. Nonetheless, the interface location can still be defined for $\theta = 0.5$.

In the Conservative Level Set (CLS) method [44], this is accomplished numerically by the use of a SUPERBBE flux limiter [45], which we adapted to our numerical platform in Chapter 3. Flux limiters add numerical dissipation in the vicinity of the interface in order to smooth it down and made it more amenable [46], and so they actually imply a dynamic regularization. The CLS method [44] regularize the initial marker function by means of a hyperbolic tangent as

$$\theta = \frac{1}{2}\left(tanh\left(\frac{r}{2\epsilon}\right) + 1\right) \tag{4.12}$$

where r is the distance function to the interface and ϵ is a smoothing parameter (in this case, $\epsilon = 0.05$), resulting in a smoothed down Heaviside step function. Olsson and Kreiss [44] introduced recompression steps into the transport of equation (4.4) in order to maintain reasonably sharp interfaces, especially when it undergoes intricate deformation.

However, the CLS method presents a major drawback: the recompression steps are not energy neutral and so are disregarded in favor of energy conservation [35]. Fortunately, the film presents a smooth deformation, and so recompression is not as critical as in flows undergoing complex interfacial deformations. Consequently, we use equation (4.12) merely for formulation purposes and let the flux limiter control the interface thickness. This fact, results in method that effectively tracks the smoothed volume fraction of the phases, resembling a smoothed version of the VOF method.

Conservation of mass

Given the sharp interface, the continuous model can flawlessly impose sharp discontinuities in physical properties. However, the use of a regularized marker implies a phase-transition zone which needs to be taken into account. While sharp approaches have been proposed in the literature [47], which provide accurate solutions locally, they sacrifice global conservation as it will be shown next.

Obtaining density as a linear function on the marker function θ

$$\rho = \rho_0 + (\rho_1 - \rho_0)\theta \tag{4.13}$$

where ρ_1 corresponds with the density of the phase indicated with $\theta = 1$ (i.e., vapor) and ρ_0 with the density of the $\theta = 0$ phase (i.e., liquid). In terms of the non-dimensional density X_ρ, we obtain:

$$X_\rho = 1 + \left(\Pi_\rho - 1\right)\theta \tag{4.14}$$

Using equation (4.13) along equation (4.4) leads to the following mass transport equation

$$\frac{\partial \rho}{\partial t} + \nabla \cdot (\vec{u}\rho) = (\rho_1 - \rho_0)\left(\frac{\partial \theta}{\partial t} + \nabla \cdot (\vec{u}\theta)\right) = 0 \tag{4.15}$$

which results in the conservation of mass within an incompressible flow ($\nabla \cdot \vec{u} = 0$), as expected. Most remarkably, it is shown how the conservation of the marker function hide the conservation of mass equation, resembling, again, a smoothed down VOF method.

Conservation of momentum

The use of the fully conservative version of the momentum equation lets the inclusion of capillary forces (disregarding gravity effects) as the only obstacle for the conservation of momentum.

The inclusion of surface tension into the momentum equation (4.5) requires a mapping from the Lagrangian frame in which equation (4.6) is formulated into the Eulerian frame of the momentum equation (4.5). Mathematically, this can be done by introducing Dirac's delta function, which does exactly this for the weak form of the equation. Following [35], we introduce the regularized Dirac's delta function δ in terms of the regularized marker function θ as

$$\delta = |\nabla \theta| \tag{4.16}$$

In this way, capillary forces in equation (4.6) can be included by means of the Continuum Surface Force (CSF) method [48] by adding

$$We\ \kappa \hat{\eta}_i \delta = We\ \kappa \nabla \theta \tag{4.17}$$

to the momentum equation

$$3Re\left(\frac{\partial \left(X_\rho \vec{u}\right)}{\partial t} + \nabla \cdot \left(X_\rho \vec{u} \otimes \vec{u}\right)\right) = -\nabla p + \nabla \cdot 2X_\mu S + X_\rho \hat{g} + We\ \kappa \nabla \theta \tag{4.18}$$

Capillary forces are inherently conservative for a closed surface, owing to its topological nature [49].

Conservation of energy

The evolution of kinetic energy $E_k = 1/2\,(\rho\vec{u}, \vec{u}))$ for multiphase flows is discussed next. We first analyze the conservation of energy in terms of the velocity field $\vec{u}$ and

the conservative equations (4.15) and (4.18) as in [43]

$$\begin{aligned}\frac{dE_k}{dt} &= \frac{1}{2}\left(\vec{u}, \frac{\partial\left(\rho\vec{u}\right)}{\partial t}\right) + \frac{1}{2}\left(\rho\vec{u}, \frac{\partial\vec{u}}{\partial t}\right) \\ &= \frac{1}{2}\left(\vec{u}, \frac{\partial\left(\rho\vec{u}\right)}{\partial t}\right) + \frac{1}{2}\left(\vec{u}, \frac{\partial\left(\rho\vec{u}\right)}{\partial t}\right) - \frac{1}{2}\left(\vec{u}, \vec{u}\frac{\partial\rho}{\partial t}\right) \\ &= \left(\vec{u}, \frac{\partial\left(\rho\vec{u}\right)}{\partial t}\right) - \frac{1}{2}\left(\vec{u}, \vec{u}\frac{\partial\rho}{\partial t}\right)\end{aligned} \tag{4.19}$$

and introducing equation (4.15) it is shown how the only contributions to kinetic energy are those arising from the momentum equation (4.18), as expected [50].

Following our previous work [35], we are left with the contribution of viscosity and surface tension to E_k. Introducing equation (4.18) into equation (4.19) we obtain

$$\frac{dE_k}{dt} = -\left(S, 2X_\mu S\right) + We\left(\vec{u}, \kappa\nabla\theta\right) + \left(\vec{u}, X_\rho\vec{g}\right) \tag{4.20}$$

We can then introduce surface energy as in [35]

$$E_p = We\left(\nabla\theta, \hat{\eta}_i\right) - \left(\vec{x}, X_\rho\vec{g}\right) \tag{4.21}$$

where $\vec{x}$ is position vector, and asses its temporal evolution as

$$\frac{dE_p}{dt} = -We\left(\vec{u}, \kappa\nabla\theta\right) - \left(\vec{u}, X_\rho\vec{g}\right) \tag{4.22}$$

where we have used the First Variation of Area [35, 51].

Finally, defining total mechanical energy as $E_m = E_k + E_p$ we can combine equations (4.20) and (4.22) to obtain the total energy equation as

$$\frac{dE_m}{dt} = \frac{dE_k}{dt} + \frac{dE_p}{dt} = -\left(S, 2X_\mu S\right) < 0 \tag{4.23}$$

which is negative-definite, as expected. Further details on the derivation on the energy-preserving level set can be found in [35]. This is quite a remarkable result as it has been shown that, despite working with a non-conservative form of the capillary term, we may still preserve the total mechanical energy within the system, resulting in an accurate, physics-compatible and stable system [35].

On the other hand, the only constrain for the inequality to hold is to provide with a positive-definite non-dimensional viscosity. This leaves room for the adoption of arbitrary interpolations on the reconstruction of viscosity. In this work we adopt a linear interpolation, which is well-suited for high viscosity and density ratios

$$\mu = \mu_0 + \left(\mu_1 - \mu_0\right)\theta \tag{4.24}$$

whose non-dimensional counterpart is

$$X_\mu = 1 + \left(\Pi_\mu - 1\right)\theta \tag{4.25}$$

while we may, eventually, adapt sharper approaches without compromising conservation.

4.3.2 Discretization

The discretization is focused on preserving the underlying mathematical structure of the space in order to attain consistent discretizations.

To do so, we proceed as in [35] by discretizing differential geometry operators from a geometrical perspective and then construct discrete vector calculus operators within a finite volume method. In terms of Mimetic Methods [52–54] this can be seen as the adoption of a low order basis. Once we obtain the discrete versions of the differential geometry operators, we construct the discrete counterparts of divergence (D), gradient (G), Laplacian (L) and convective ($\mathsf{C}(\cdot)$) operators, resulting in a classical finite volume, second order, staggered method as introduced by Harlow and Welch [32, 55]. In addition, we introduce high resolution advectin schemes ($\mathsf{C}(\mathbf{u_f})$) via flux limiters in a similar fashion [56].

After adopting proper regularization as described in section 4.3.1, we introduce the following equations for the physical properties

$$\rho_\mathbf{f} = 1 + \left(\Pi_\rho - 1\right)\theta_\mathbf{f} \tag{4.26}$$

$$\mu_\mathbf{f} = 1 + \left(\Pi_\mu - 1\right)\theta_\mathbf{f} \tag{4.27}$$

while the original set of governing equations (4.3-4.5) is discretized as

$$\mathsf{D}\mathbf{u_f} = 0_c \tag{4.28}$$

$$\frac{d\theta_\mathbf{c}}{dt} = -\mathsf{C}(\mathbf{u_f})\theta_\mathbf{c} \tag{4.29}$$

$$3Re\frac{d\left(\mathsf{P}\mathbf{u_f}\right)}{dt} = -\mathsf{C}(\mathsf{P}\mathbf{u_f})\mathbf{u_f} - \mathsf{G}\mathbf{p_c} + \mathsf{L}\mathbf{u_f} + We\,\mathsf{K_F}\mathsf{G}\theta_\mathbf{c} + \mathsf{P}[]g \tag{4.30}$$

where $\mathbf{u_f}$ stands for the staggered velocity field, $\theta_\mathbf{c}$ is the collocated marker function and $\mathbf{p_c}$ the collocated pressure, $\mathsf{P} = \mathsf{diag}\left(\rho_\mathbf{f}\right)$ is the diagonal matrix arrangement of the staggered density, and $\mathsf{K_F} = \mathsf{diag}\left(\mathsf{Y}\mathbf{k_c}\right)$ is the diagonal arrangement of the staggered curvature that was introduced in Valle et al. [35].

Conservation of mass

Despite not tracking a discrete counterpart of the mass conservation equation (4.15) explicitly, the conservation of the marker function stated in equation (4.29) together

with the linear reconstruction of density in terms of equation (4.26) yields an implicit conservation of mass equation as

$$\frac{d\rho_{\mathbf{c}}}{dt} = (\rho_1 - \rho_0)\frac{d\theta_{\mathbf{c}}}{dt} = -(\rho_1 - \rho_0)\mathsf{C}(\mathbf{u_f})\theta_{\mathbf{c}} = -\mathsf{C}(\mathbf{u_f})\rho_{\mathbf{c}} \tag{4.31}$$

which, just as in the regularized case, it is implicitly defined by means of equations (4.26) and (4.29).

As a result, mass is preserved as far as the marker function is, just as in the regularized case. Note, however, that the velocity field needs to satisfy $\mathsf{D}\mathbf{u_f} = 0$, which is not easy to achieve in general at the discrete level, as it will be discussed in section 4.3.3.

Conservation of momentum

The discretization of linear momentum stated in equation (4.30) preserves momentum in virtue of the original conservative formulation.

Nonetheless, the inclusion of the capillary term does pose a challenge regarding conservation of linear momentum.

Conservation of energy

Finally, following the regularization introduced in section (4.3.1), we aim at preserving total mechanical energy at the discrete level. To do so, we first derive the evolution of discrete kinetic energy as in equation (4.19) by including equations (4.30) and (4.31), the former requiring the use of the isometric cell-to-face interpolation operator Π in order to match dimensions. After rearranging terms, we obtain

$$\begin{aligned}\frac{d\mathbf{E_k}}{dt} =& -(\mathbf{u_f}, \mathsf{C}(\mathsf{P}\mathbf{u_f})\mathbf{u_f}) + (\mathbf{u_f}, \mathsf{G}\mathbf{p_c}) + (\mathbf{u_f}, \mathsf{L}\mathbf{u_f}) + We\,(\mathbf{u_f}, \mathsf{K_F}\mathsf{G}\theta_{\mathbf{c}}) + (\mathbf{u_f}, \mathsf{P}[]g) \\ &+ \frac{1}{2}(\mathbf{u_f}, \mathsf{U}\Pi\mathsf{C}(\mathbf{u_f})\rho_{\mathbf{c}})\end{aligned} \tag{4.32}$$

where $\mathsf{U} = diag\,(\mathbf{u_f})$ is the diagonal arrangement of the staggered velocity field. We have also included the implicit version of the mass transfer equations, even when, as it was discussed above, this equation is not explicitly computed.

Subsequently, the evolution of discrete potential energy equation is obtained in analogous way as in equation (4.22)

$$\frac{d\mathbf{E_p}}{dt} = -We\,(\mathbf{u_f}, \mathsf{K_F}\mathsf{G}\theta_{\mathbf{c}}) - (\mathbf{u_f}, \mathsf{P}\mathbf{g}) \tag{4.33}$$

where we have adopted an energy-preserving discretization of the capillary terms as we did in [35].

Finally, we are now able to assess the evolution of discrete mechanical energy as we did in equation (4.23) by including equations (4.32) and (4.33). After rearranging, we obtain

$$\frac{d\mathbf{E_m}}{dt} = -\left(\mathbf{u_f}, \mathsf{C}(\mathsf{P}\mathbf{u_f})\mathbf{u_f}\right) + \frac{1}{2}\left(\mathbf{u_f}, \mathsf{U}\Pi\mathsf{C}(\mathbf{u_f})\rho_\mathbf{c}\right) + \left(\mathbf{u_f}, \mathsf{L}\mathbf{u_f}\right) < 0 \tag{4.34}$$

where the pressure terms has vanished given that $\mathsf{D}\mathbf{u_f} = 0$, as shown in [32].

We are, however, left with the two first convective terms in equation (4.34) which should, in virtue of its convective nature, ideally vanish.

From this point onward, we follow Mirjalili and Mani [50] to show how the adoption of a consistent mass and momentum transport and a smart interpolation strategy results in an energy-consistent discretization. To do so, we proceed first by noting that the momentum convective operator is not skew-symmetric due to $\mathsf{DP}\mathbf{u_f} \neq 0$. However, a closer look to the convective operator shows that, due to the mimetic structure adopted for the construction of $\mathsf{C}(\cdot)$, it is skew-symmetric except for the diagonal term, which corresponds with half the staggered divergence of the flow, $1/2 diag\left(\Pi\mathsf{DP}\mathbf{u_f}\right)$, where the $1/2$ factor arise from the skew-symmetric operator applied to the transported velocity field [32]. Note that, owing to $\mathsf{D}\mathbf{u_f} = 0$, this results in a purely skew-symmetric operator when density is constant, as in Verstappen and Veldman [32]. Exploiting this fact, we can decompose $\mathsf{C}(\mathsf{P}\mathbf{u_f})$ as

$$\mathsf{C}(\mathsf{P}\mathbf{u_f}) = \overline{\mathsf{C}(\mathsf{P}\mathbf{u_f})} + \frac{1}{2} diag\left(\Pi\mathsf{DP}\mathbf{u_f}\right) \tag{4.35}$$

where we introduce a purely skew-symmetric operator, $\overline{\mathsf{C}(\mathsf{P}\mathbf{u_f})}$, which results into an energy neutral operator.

Introducing equation (4.35) into equation (4.34) we obtain

$$\frac{d\mathbf{E_m}}{dt} = \frac{1}{2}\left(\mathbf{u_f}, diag\left(\Pi\mathsf{DP}\mathbf{u_f}\right)\mathbf{u_f}\right) + \frac{1}{2}\left(\mathbf{u_f}, \mathsf{U}\Pi\mathsf{C}(\mathbf{u_f})\rho\right) + \left(\mathbf{u_f}, \mathsf{L}\mathbf{u_f}\right) \tag{4.36}$$

then, exploiting $Ab = diag(a)b = diag(b)a = Ba$ to rearrange $diag\left(\Pi\mathsf{DP}\mathbf{u_f}\right)\mathbf{u_f} = \mathsf{UDP}\mathbf{u_f}$ first and $\mathsf{P}\mathbf{u_f} = \mathsf{U}\rho_\mathbf{f}$ later, we obtain

$$\frac{d\mathbf{E_m}}{dt} = \frac{1}{2}\left(\mathbf{u_f}, \mathsf{U}\Pi\mathsf{DU}\rho_\mathbf{f}\right) + \frac{1}{2}\left(\mathbf{u_f}, \mathsf{U}\Pi\mathsf{C}(\mathbf{u_f})\rho_\mathbf{c}\right) + \left(\mathbf{u_f}, \mathsf{L}\mathbf{u_f}\right) \tag{4.37}$$

We then introduce the definition $\mathsf{C}(\mathbf{u_f}) = \mathsf{DU}\Psi$ introduced in [35, 56], where Ψ contains the high resolution cell-to-face interpolation, to yield

$$\frac{d\mathbf{E_m}}{dt} = \frac{1}{2}\left(\mathbf{u_f}, \mathsf{U}\Pi\mathsf{DU}\rho_\mathbf{f}\right) + \frac{1}{2}\left(\mathbf{u_f}, \mathsf{U}\Pi\mathsf{DU}\Psi\rho_\mathbf{c}\right) + \left(\mathbf{u_f}, \mathsf{L}\mathbf{u_f}\right) \tag{4.38}$$

from where we can infer the proper cell-to-face interpolation for the discrete density field as

$$\rho_{\mathbf{f}} = \Psi \rho_{\mathbf{c}} \tag{4.39}$$

in order to cancel out the convective contributions to the discrete mechanical energy and yield the desired equation

$$\frac{d\mathbf{E_m}}{dt} = (\mathbf{u_f}, \mathsf{L}\,\mathbf{u_f}) < 0 \tag{4.40}$$

Note, however, that $\rho_{\mathbf{c}}$ is actually not computed. Nonetheless, in virtue of the linear relationship between θ and ρ stated in equation (4.13), the relation can be expressed in terms of the marker function at the faces $\theta_{\mathbf{f}}$, which is needed for the integration of equation (4.29) and thus can be reused as

$$\rho_{\mathbf{f}} = \rho_0 + (\rho_1 - \rho_0)\theta_{\mathbf{f}} \tag{4.41}$$

stating an explicit relationship between the advection of the marker function and the reconstruction of density. This was previously introduced in the literature, along with other specific techniques, as consistent mass and momentum transport [40–42]. The reader is referred to Mirjalili and Mani [50] for a thoughtful review on this topic.

In summary, we have developed a consistent discretization that can easily preserve mass, momentum (up to surface tension) and energy, as it can be seen in table 4.1.

	$\mathsf{C}(\mathbf{u_f})\theta_{\mathbf{c}}$	$\mathsf{C}(\mathsf{P}\mathbf{u_f})\mathbf{u_f}$	$\mathsf{G}\mathbf{p_c}$	$\mathsf{L}\,\mathbf{u_f}$	$We\,\mathsf{K_F}\mathsf{G}\theta_{\mathbf{c}}$	$\mathsf{P}[]g$
mass	✓	n/a	n/a	n/a	n/a	n/a
momentum	n/a	✓	✓	✓	x	✓
energy	n/a	✓	✓	✓	✓	✓

Table 4.1: Summary of terms involved in the discretization and whether their discretization obeys the expected behavior regarding mass, momentum and energy.

4.3.3 Integration

The adoption of a fully conservative formulation removed an explicit equation for velocity, preventing us form directly adopting a classical Fractional Step Method (FSM) [57–59] for the pressure-velocity decoupling. However, following the original work of Rudman [40], the adoption of the FSM method can proceed with slight modifications. We adopt the LU decomposition approach introduced by Perot [58] in order to show the integration procedure of an explicit time integration scheme and the modification with respect to the classical FSM followed by Rudman [40].

Next we will highlight the most relevant modifications to the classical FSM. First, following the conservative nature of the governing, equations, we will integrate in time discrete momentum i.e., considering $(\mathsf{P}\mathbf{u_f})$ as variable on its own. Second, we will use the new density and momentum fields in order to obtain a new velocity field which is consistent with the former two. Finally, to ease the algebraic manipulation, we will apply the Laplace transform ($\mathcal{L}$) to the semi-discretized. Namely, we will use

$$\frac{d}{dt}f(t) \underset{\mathcal{L}^{-1}}{\overset{\mathcal{L}}{\longleftrightarrow}} sf(s) \tag{4.42}$$

$$\int_0^t f(\tau)d\tau \underset{\mathcal{L}^{-1}}{\overset{\mathcal{L}}{\longleftrightarrow}} \frac{1}{s}f(s) \tag{4.43}$$

to handle time derivative and time integration in an entirely algebraic way. Needles to say, we will recover the differential formulation after we are done with the algebraic manipulation To sum up, the semi-discretized equations (4.29) and (4.30) can be compiled together with the velocity-momentum expression and the usual divergence-free constrain $\mathsf{D}\mathbf{u_f} = 0$ to result in a linear system of equations $Ax = b$ as the following one

$$\begin{pmatrix} s & 0 & 0 & 0 \\ 0 & s & 0 & \mathsf{G} \\ 0 & \mathsf{I_f} & -\mathsf{P} & 0 \\ 0 & 0 & \mathsf{D} & 0 \end{pmatrix} \begin{pmatrix} \theta_\mathbf{c} \\ \mathsf{P}\mathbf{u_f} \\ \mathbf{u_f} \\ \mathbf{p_c} \end{pmatrix} = \begin{pmatrix} -\mathsf{C}(\mathbf{u_f})\theta_\mathbf{c} \\ \mathsf{R}(\rho_\mathbf{f}{}^n, \mathbf{u_f}{}^n, \mathbf{p_c}{}^n) \\ 0_f \\ 0_c \end{pmatrix} \tag{4.44}$$

where $\mathsf{R}(\rho_\mathbf{f}{}^n, \mathbf{u_f}{}^n, \mathbf{p_c}{}^n) = -\mathsf{C}(\mathsf{P}^n\mathbf{u_f}{}^n)\mathbf{u_f}{}^n - \mathsf{L}\mathbf{u_f}{}^n + We\mathsf{K}^n\mathsf{G}\theta_\mathbf{c}{}^n + \mathsf{P}^n[]g$ corresponds with the right hand side of equation (4.30) without the pressure term. Note the role of the Laplace transform in the first and second rows, which reads as time derivatives of $\theta_\mathbf{c}$ and $(\mathsf{P}\mathbf{u_f})$, respectively. The third row of the matrix impose the match between the velocity ($\mathbf{u_f}$) and momentum (($\mathsf{P}\mathbf{u_f}$)) at the next time level, while the last one enforce the incompressibility constraint to ($\mathbf{u_f}$). Note that the left hand side is evaluated at time level $n+1$, while the right hand side is evaluated at n. In an explicit setup as the one described here, this implies that the density field used for the momentum transport (2nd row) is evaluated at time level n, whereas the density field used to impose the divergence-free velocity field is evaluated at time level $n+1$. We can then perform an LU decomposition as

$$\begin{pmatrix} s & 0 & 0 & 0 \\ 0 & s & 0 & \mathsf{G} \\ 0 & \mathsf{I_f} & -\mathsf{P} & 0 \\ 0 & 0 & \mathsf{D} & 0 \end{pmatrix} = \begin{pmatrix} s & 0 & 0 & 0 \\ 0 & s & 0 & 0 \\ 0 & \mathsf{I_f} & -\mathsf{P} & 0 \\ 0 & 0 & \mathsf{D} & -\frac{1}{s}\mathsf{D}\mathsf{P}^{-1}\mathsf{G} \end{pmatrix} \begin{pmatrix} \mathsf{I_c} & 0 & 0 & 0 \\ 0 & \mathsf{I_f} & 0 & \frac{1}{s}\mathsf{G} \\ 0 & 0 & \mathsf{I_f} & \frac{1}{s}\mathsf{P}^{-1}\mathsf{G} \\ 0 & 0 & 0 & \mathsf{I_c} \end{pmatrix} \tag{4.45}$$

where the role of s in L and $1/s$ in U can be read, after undoing the Laplace transform, as "take the derivative of" and "perform the time integration on" whatever

variable results from the algebraic manipulation, respectively. From here, the modified FSM algorithm follows by the usual solution of the system by LU inversion. Namely, we take a predictive step

$$\begin{pmatrix} s & 0 & 0 & 0 \\ 0 & s & 0 & 0 \\ 0 & \mathsf{D}\mathsf{P}^{-1} & -\frac{1}{s}\mathsf{D}\mathsf{P}^{-1}\mathsf{G} & 0 \\ 0 & -\mathsf{I}_\mathsf{f} & \frac{1}{s}\mathsf{G} & \mathsf{P} \end{pmatrix}^{-1} \begin{pmatrix} \theta_\mathbf{c} \\ \mathsf{P}\mathbf{u}_\mathbf{f} \\ \mathbf{u}_\mathbf{f} \\ \mathbf{p}_\mathbf{c} \end{pmatrix}^{\star} = \begin{pmatrix} -\mathsf{C}(\mathbf{u}_\mathbf{f})\theta_\mathbf{c} \\ \mathsf{R}(\rho_\mathbf{f}{}^n, \mathbf{u}_\mathbf{f}{}^n, \mathbf{p}_\mathbf{c}{}^n) \\ 0_f \\ 0_c \end{pmatrix} \tag{4.46}$$

and subsequently a corrective one

$$\begin{pmatrix} \mathsf{I}_\mathsf{c} & 0 & 0 & 0 \\ 0 & \mathsf{I}_\mathsf{f} & 0 & \frac{1}{s}\mathsf{G} \\ 0 & 0 & \mathsf{I}_\mathsf{f} & \frac{1}{s}\mathsf{P}^{-1}\mathsf{G} \\ 0 & 0 & 0 & \mathsf{I}_\mathsf{c} \end{pmatrix}^{-1} \begin{pmatrix} \theta_\mathbf{c} \\ \mathsf{P}\mathbf{u}_\mathbf{f} \\ \mathbf{u}_\mathbf{f} \\ \mathbf{p}_\mathbf{c} \end{pmatrix} = \begin{pmatrix} \theta_\mathbf{c} \\ \mathsf{P}\mathbf{u}_\mathbf{f} \\ \mathbf{u}_\mathbf{f} \\ \mathbf{p}_\mathbf{c} \end{pmatrix}^{\star} \tag{4.47}$$

Undoing the Laplace transforms for the time derivatives terms, we realize that we can actually re-define pressure to include the time integration involved in both predictor and corrector steps, resulting in a way simpler manipulation. We summarize the resulting algorithm as were we have we have re-stated the computation of the

Algorithm 1 Integration of the governing equations along a Fractional Step Method as in [40]

1	Integrate	$\frac{d\theta_\mathbf{c}}{dt}$	$= -\mathsf{C}(\mathbf{u}_\mathbf{f})\theta_\mathbf{c}{}^n$	$\rightarrow \theta_\mathbf{c}{}^{n+1}$
2	Integrate	$\frac{d(\mathsf{P}\mathbf{u}_\mathbf{f})}{dt}$	$= \mathsf{R}(\rho_\mathbf{f}{}^n, \mathbf{u}_\mathbf{f}{}^n, \mathbf{p}_\mathbf{c}{}^n)$	$\rightarrow (\mathsf{P}\mathbf{u}_\mathbf{f})^\star$
3	Solve	$\mathsf{P}^{n+1}\mathbf{u}_\mathbf{f}{}^\star$	$= (\mathsf{P}\mathbf{u}_\mathbf{f})$	$\rightarrow \mathbf{u}_\mathbf{f}{}^\star$
4	Solve	$\mathsf{D}\mathsf{P}^{-1}\mathsf{G}\mathbf{p}_\mathbf{c}{}^{n+1}$	$= \mathsf{D}\mathbf{u}_\mathbf{f}{}^\star$	$\rightarrow \mathbf{p}_\mathbf{c}{}^{n+1}$
5	Correct	$\mathbf{u}_\mathbf{f}{}^{n+1}$	$= \mathbf{u}_\mathbf{f}{}^\star - \frac{1}{dt}\mathsf{P}^{-1}\mathsf{G}\mathbf{p}_\mathbf{c}$	$\rightarrow \mathbf{u}_\mathbf{f}{}^{n+1}$
6	Update	$(\mathsf{P}\mathbf{u}_\mathbf{f})^{n+1}$	$= \mathsf{P}^{n+1}\mathbf{u}_\mathbf{f}{}^{n+1}$	$\rightarrow (\mathsf{P}\mathbf{u}_\mathbf{f})^{n+1}$

$(\mathsf{P}\mathbf{u}_\mathbf{f})^{n+1}$ in the equivalent form of step 6 to reassert that the new momentum field is consistent with the divergence-free velocity and density fields.

Time integration is performed with a 3rd order Runge-Kutta method for step 1 and a 2nd order Adams-Bashforth one for step 2. The solver used in step 4 is a Preconditioned Conjugate Gradient (PCG) method preconditioned with P in order to reduce the condition number of the system. Steps 3, 5 and 6 are trivial element-wise manipulations.

4.4 Preliminary results

With the aforementioned discretization in mind, we showcase the proposed DNS discretization of the system with the simulation of three industrially relevant falling films.

While actual absorbers consist of long tubes in which the film develops, we focus on the fluid dynamics of a rather simple wave, which can be seen as considering a single region within the absorber.

Because the physics we target are inherently fluid- and thermal dynamic, we need to estimate the physical parameters of the working liquid-gas pair to a constant value. Namely, we impose the conditions at the inlet of the absorber, which is where most of the heat transfer takes place. Regarding the discretization domain, instead of imposing symmetry, we set up a symmetric layout consisting of two films falling down parallel walls.

For the liquid phase three typical working fluids will be considered. Pure water (H_2O) at saturation temperature will set the base case; while two industrial liquid/absorbent pairs at $50°C$ will also be considered: the classical $H_2O/LiBr$ solution and the commercial $H_2O/Carrol$; where *Carrol* is a mixture of mainly $LiBr$ and ethylene glicol in a $4/5$ mass ratio. A summary of the working conditions can be found in table 4.2.

While liquid and vapor properties are well defined for pure H_2O, the liquid properties strongly depend on the absorbent (i.e., $LiBr$ or *Carrol*) mass fraction, which is adjusted in order for the solution to exhibit the same saturation pressure (i.e., an equivalent mass transfer potential). While typical absorption chillers operate under negative pressures (i.e., $\sim$ 1220 Pa absolute pressure) we will stick to atmospheric vapor phases.

Density and viscosity for both phases are then obtained from temperature, pressure and, for the liquid phase solely, absorbent concentration. Lacking better conditions, surface tension properties are taken at equilibrium conditions between pure water and steam, i.e., regardless pressure and absorbent concentration.

Finally, the Reynolds number will be set at $Re = \{150, 200\}$ to define typical falling film dynamics involved in $LiBr$ absorption chillers.

Introducing the Kapitza number

$$Ka = \frac{\gamma}{\rho_l^{1/3} \mu_l^{4/3}} \tag{4.48}$$

we obtain a dimensionless number that is fixed with the physical properties of the working liquid, while the density (Π_ρ) and viscosity (Π_μ) ratios provide with the information regarding the vapor phase. In this manner, the liquid-gas pair properties can be fully described by Ka, Π_ρ and Π_μ, while Re is left as the solely variable con-

id	fluid	$T(^\circ C)$	X_{abs}	Ka	$\Pi_\rho(\times 10^{-3})$	$\Pi_\mu(\times 10^{-3})$
A	H_2O	9.9	0.00	2420	0.60	9.37
B	$H_2O/LiBr$	50.0	0.60	443	0.35	2.45
C	$H_2O/Carrol$	50.0	0.67	150	0.35	1.10

Table 4.2: Estimated fluid properties dimensionless groups. Because thermal properties are estimated at a characteristic state, values are rounded to ease its handling.

trolling the fluid dynamics of the system. With this in mind, we obtain the following table estimating the physical properties group for the 3 working fluids.

The computational domain is a $[10h_N \times \Lambda_y \times \Lambda_z]$ box with periodic boundaries in both y and z directions, where $\Lambda_y = \Lambda_x = 100h_N$, which correspond with the length of a long-wave perturbation. We will denote x, y and z directions as wall-normal, stream-wise and span-wise, and N_x, N_y and N_z the number of nodes in the x, y and z directions. The formulation in terms of the Nusselt scaling as presented in section 4.2 allows for a unified interface resolution regardless of the Reynolds number. The mesh is refined in the vicinity of the flat film thickness and coarsened at the center of the box, where the gas phase is expected. It is therefore symmetrical with respect to the wall-normal mid-plane. The following expression gives the refinement introduced in the x axis

$$
\begin{aligned}
x &= L_x \left(0.5 f_x \left(1 + \frac{sinh\left(\alpha\left(\frac{i}{N_r} - 0.5\right)\right)}{sinh\left(\frac{\alpha}{2}\right)} \right) \right) && \forall i \in [0, N_r] \\
x &= L_x \left(f_x + 0.5(1-2f_x) \left(1 + \frac{tanh\left(\beta \frac{i-N_r}{N_x - 2N_r} - 0.5\right)}{tanh\left(\frac{\beta}{2}\right)} \right) \right) && \forall i \in [N_r, N_x - N_r] \\
x &= L_x \left((1-f_x) + 0.5 f_x \left(1 + \frac{sinh\left(\alpha \frac{i-N_x+N_r}{N_r} - 0.5\right)}{sinh\left(\frac{\alpha}{2}\right)} \right) \right) && \forall i \in [N_x - N_r, N_x]
\end{aligned}
\tag{4.49}
$$

where $L_x = 10$, $f_x = 0.2$ is the fraction of L_x refined close to the wall, while $N_r = N_x/3$ is the number of nodes introduced in the refinement regions. Parameters $\alpha = 2$ and $\beta = 2$ control the smoothness of the refinements.

The numerical methods and algorithms introduced in this work have been implemented in the framework of the in-house platform TermoFluids [60].

Results shown in figures 4.4 and 4.4 show the impact of the decreasing Kapitza number into the dynamics of the surface. As it can be seen, the stabilizing effect of surface tension fades as the Kapitza number is reduced, thus enhancing the appear-

ance of larger humps and complex instabilities.

In this regard, results show the appearance of a leading depression before the arrival of the wave tip, which drains fluid in the z direction, which contributes to the appearance of $3D$ structures as shown in [28]. This depression is more pronounced in the low Kapitza cases due to the stabilizing effect that capillary force plays in the development of surface deformations. While the stiffer case A presents a less marked curvature, it also presents more undulations on the film surface. This results in the appearance of a more dispersed velocity field on top of the film surface. Conversely, lower Kapitza numbers result in more acute film deformations, which, on the other hand, contribute to smaller, but also more coherent, flow patterns.

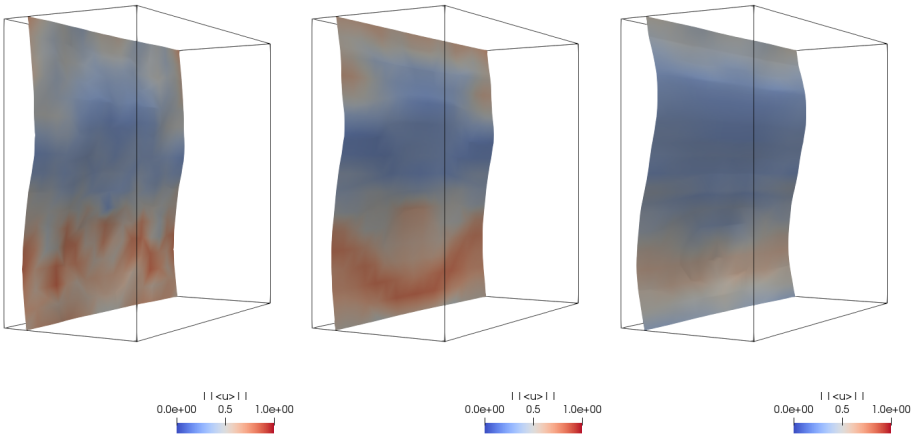

Figure 4.1: Velocity magnitude on the film surfaces for cases A, B and C at $Re = 150$ after $T = 100$.

Regarding the shape of the film interface, it can be observed how case B produces a more abrupt hump, showing a marked preceding wave rise and a also a central delay on wave maximum, pushing the flow in the z direction and thus revealing the incipient formation of a horseshoe pattern. On the other hand, milder surface effects in case C result in a smoother undulation, which show smaller z axis flow which is mainly in the y direction. These effects are intensified with the increase of the Reynolds number, as it can be seen for case B at $Re = 200$. In that situation, the wave is rolling on top of itself thus increasing the hump height an resulting into a growing large scale instability. On the other hand, the high Kapitza case presented in case A shows milder velocity fields at higher Reynolds numbers, which may caused by an

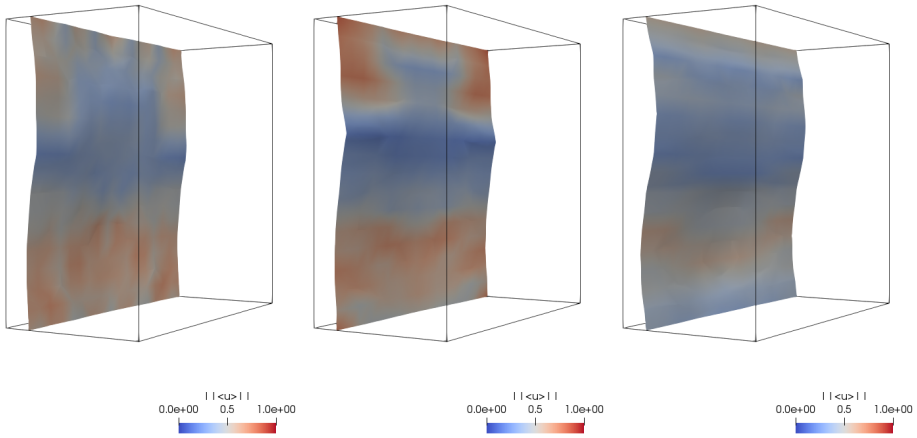

Figure 4.2: Velocity magnitude on the film surfaces for cases A, B and C at $Re = 200$ after $T = 100$.

intensified momentum diffusion at the interface due to the high frequency pattern that the undulations on top of the surface form.

Figures 4.4 and 4.4 show an increasing intensity of the wavy behavior along with and increased Reynolds number, as expected. They also reveal a flatter interface for the high Kapitza case, while cases B and C show the clear appearance of the wave pattern.

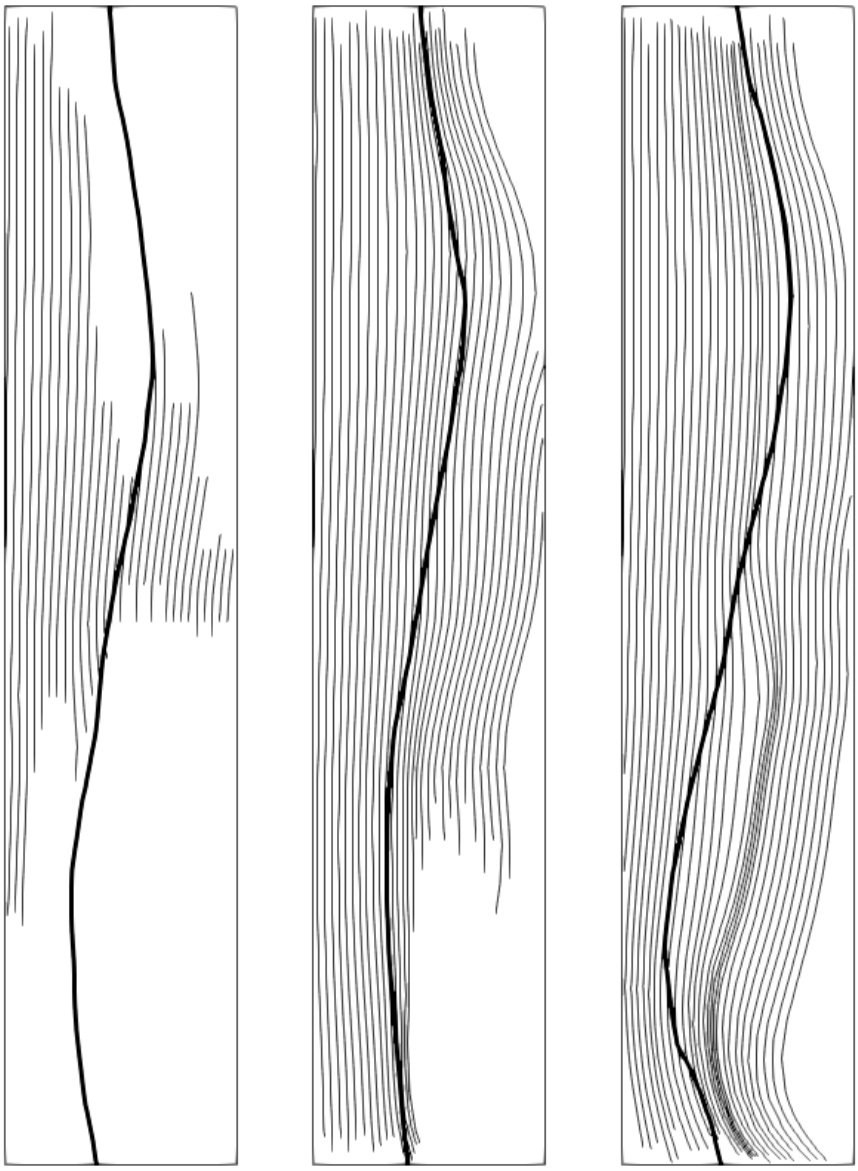

Figure 4.3: Streamlines for cases A, B and C at $Re = 150$ after $T = 100$ for the $x - y$ mid-plane.

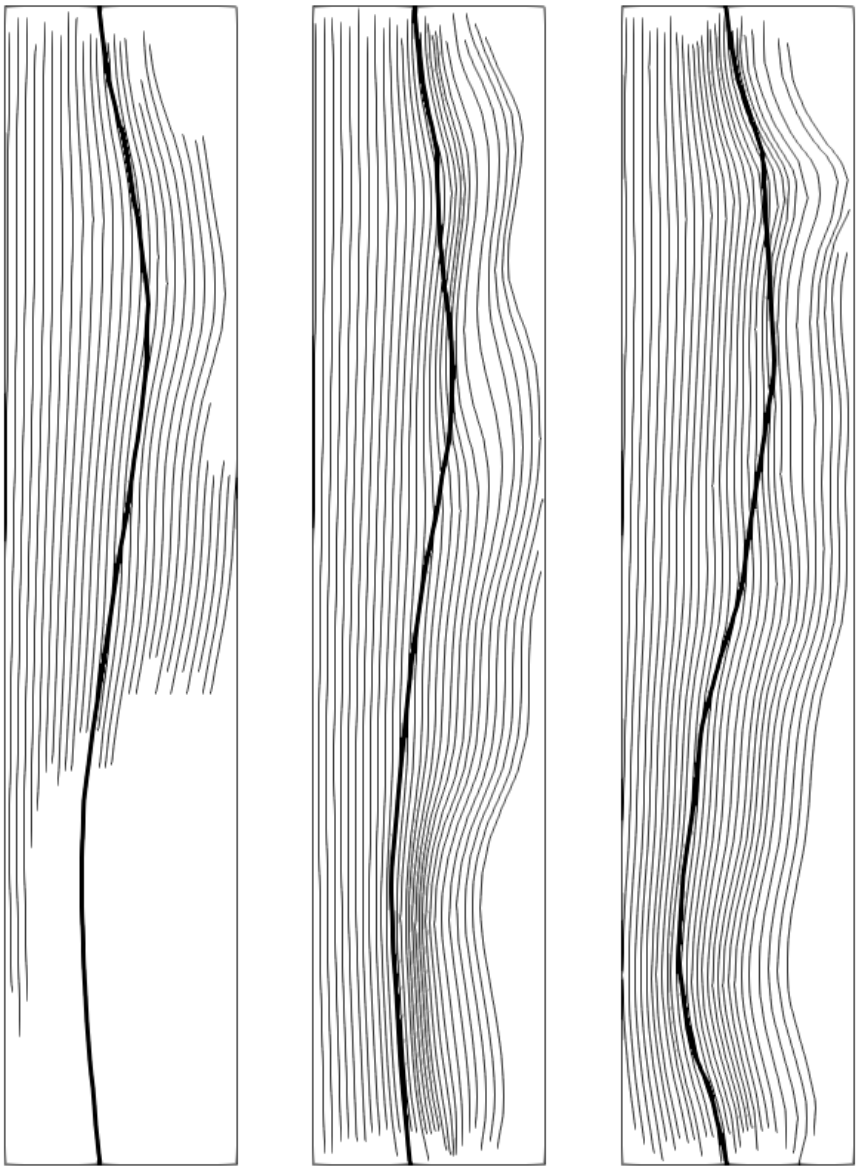

Figure 4.4: Streamlines for cases A, B and C at $Re = 200$ after $T = 100$ for the $x - y$ mid-plane.

4.5 Conclusions

The method has been deployed in the DNS of vertical falling films under extreme density ratios, which pose a major numerical challenge and at the same time are of industrial relevance.

Results are in accordance with the expected behavior of such films and reported in both experimental and numerical literature. In this regard, it is shown capillary forces stabilizing effect on the film dynamics. Accordingly, reducing surface tension (e.g., by adding surfactants) is observed to enhance instability of the system.

A fully mass and energy-preserving scheme has been developed in the context of the conservative level set method. Extending our previous work on the energy-preserving inclusion of curvature [35] and adopting the ideas presented in Mirjalili and Mani [43] for the discretization of the convective terms, we have succeed at presenting a formulation which is mathematically consistent. The aforementioned merits benefit from the adoption of our heavily algebraic-based formulation both for the discretization of the terms comprising the discrete equations and the formulation of the modified FSM proposed by Rudman [40], as it simplifies the analysis of the new method properties; revealing the close connection between consistent mass and momentum transfer and the conservation of energy.

In summary, such a consistency requires the adoption of the same discretization for the mass flux at the faces (either it is implicitly or explicitly computed) and the adoption of a pressure-velocity splitting scheme which enforce the consistency between density and momentum fields.

While we succeeded at the formulation of a fully mass conservative and energy-preserving scheme, the conservation of linear momentum is still unclear [36]. However, as it was already commented in [35] while the lack of conservation of total momentum is an undesired property, the adoption of an energy-preserving scheme provides a bound on total energy and thus a bound on the system variables, which in turn provides with enhanced stability. Nonetheless, the conservation of linear momentum is an active line of research that deserves further discussion.

References

[1] P.L. Kapitza and S.P. Kapitza. Wave flow of thin layers of a viscous fluid. In D. Ter Haar, editor, *Collect. Pap. P.L. Kapitza*, volume 2, pages 662–708. Pergamon, 1965.

[2] S. Kalliadasis, C. Ruyer-Quil, B. Scheid, and M. G. Velarde. *Falling Liquid Films*, volume 176. Springer, London, 2012.

[3] Chia-Shun Yih. Stability of two-dimensional parallel flows for three-dimensional disturbances. *Q. Appl. Math.*, 12(4):434–435, 1955.

[4] Chia-Shun Yih. Stability of liquid flow down an inclined plane. *Phys. Fluids*, 6(3):14, 1963.

[5] T. Brooke Benjamin. Wave formation in laminar flow down an inclined plane. *J. Fluid Mech.*, 2(06):554, aug 1957.

[6] Francisco J. Solorio. Linear stability of a cylindrical falling film. *J. Fluid Mech.*, 183:365–377, 1987.

[7] T. Nosoko, P.N. Yoshimura, T. Nagata, and K. Oyakawa. Characteristics of two-dimensional waves on a falling liquid film. *Chem. Eng. Sci.*, 51(5):725–732, 1996.

[8] C. D. Park and T. Nosoko. Three-Dimensional Wave Dynamics on a Falling Film and Associated Mass Transfer. *AIChE J.*, 49(11):2715–2727, 2003.

[9] Akio Miyara, Tomoki Yamamoto, Toru Iemura, and Takashi Shimada. Gas absorption by wavy falling liquid film formed on inner surface of vertical tubes. *J. Therm. Sci.*, 12(1):57–61, 2003.

[10] Sung-bum Park and Huen Lee. Heat and Mass Transfer of the New LiBr-Based Working Fluids for Absorption Heat Pump. *Society*, pages 1378–1385, 2002.

[11] Wen Long Cheng, Kouichi Houda, Ze Shao Chen, Atsushi Akisawa, Peng Hu, and Takao Kashiwagi. Heat transfer enhancement by additive in vertical falling film absorption of H2O/LiBr. *Appl. Therm. Eng.*, 24(2-3):281–298, 2004.

[12] E. García-Rivera, J. Castro, J. Farnós, and A. Oliva. Numerical and experimental investigation of a vertical LiBr falling film absorber considering wave regimes and in presence of mist flow. *Int. J. Therm. Sci.*, 109:342–361, 2016.

[13] S. V. Alekseenko, V. A. Antipin, V. V. Guzanov, S. M. Kharlamov, and D. M. Markovich. Three-dimensional solitary waves on falling liquid film at low Reynolds numbers. *Phys. Fluids*, 17(12):1–4, 2005.

[14] Sergey V. Alekseenko, Andrey V. Cherdantsev, Mikhail V. Cherdantsev, Sergey V. Isaenkov, and Dmitriy M. Markovich. Study of formation and development of disturbance waves in annular gas–liquid flow. *Int. J. Multiph. Flow*, 77:65–75, dec 2015.

[15] S. M. Kharlamov, V. V. Guzanov, A. V. Bobylev, S. V. Alekseenko, and D. M. Markovich. The transition from two-dimensional to three-dimensional waves in falling liquid films: Wave patterns and transverse redistribution of local flow rates. *Phys. Fluids*, 27(11), 2015.

[16] A. Akesjo. *Hydrodynamics and Heat Transfer in Vertical Falling Films with Smooth and Modified Heat-Transfer Surfaces – An Experimental and Numerical Investigation*. PhD thesis, Chalmers University of Technology, 2018.

[17] J.-C. Nave, X. D. Liu, and Sanjoy Banerjee. Direct Numerical Simulation of Liquid Films with Large Interfacial Deformation. *Stud. Appl. Math.*, pages 153–177, 2010.

[18] Fabian Denner, Marc Pradas, Alexandros Charogiannis, Christos N. Markides, Berend G. M. van Wachem, and Serafim Kalliadasis. Self-similarity of solitary waves on inertia-dominated falling liquid films. *Phys. Rev. E*, 93(3):033121, mar 2016.

[19] Fabian Denner, Alexandros Charogiannis, Marc Pradas, Christos N. Markides, Berend G.M. Van Wachem, and Serafim Kalliadasis. Solitary waves on falling liquid films in the inertia-dominated regime. *J. Fluid Mech.*, 837:491–519, feb 2018.

[20] Fabian Denner and Berend G.M. van Wachem. Numerical methods for interfacial flows with high density ratios and high surface tension, 2014.

[21] Fabian Denner and Berend G.M. van Wachem. Compressive VOF method with skewness correction to capture sharp interfaces on arbitrary meshes. *J. Comput. Phys.*, 279:127–144, 2014.

[22] Fabian Denner and B.G.M. van Wachem. TVD differencing on three-dimensional unstructured meshes with monotonicity-preserving correction of mesh skewness. *J. Comput. Phys.*, 298:466–479, 2015.

[23] Marc Pradas, Dmitri Tseluiko, and Serafim Kalliadasis. Rigorous coherent-structure theory for falling liquid films: Viscous dispersion effects on bound-state formation and self-organization. *Phys. Fluids*, 23(4), 2011.

[24] Fabian Denner. Frequency dispersion of small-amplitude capillary waves in viscous fluids. *Phys. Rev. E*, 94(2), 2016.

[25] Georg F. Dietze and Reinhold Kneer. Flow separation in falling liquid films. *Front. Heat Mass Transf.*, 2(3), 2011.

[26] Shoushi Bo, Xuehu Ma, Hongxia Chen, and Zhong Lan. Numerical simulation on vapor absorption by wavy lithium bromide aqueous solution films. *Heat Mass Transf. und Stoffuebertragung*, 47(12):1611–1619, 2011.

[27] Christoph Albert, Holger Marschall, and Dieter Bothe. Direct numerical simulation of interfacial mass transfer into falling films. *Int. J. Heat Mass Transf.*, 69:343–357, 2014.

[28] Georg F. Dietze, W. Rohlfs, K. Nährich, R. Kneer, and B. Scheid. Three-dimensional flow structures in laminar falling liquid films. *J. Fluid Mech.*, 743:75–123, 2014.

[29] Georg F. Dietze. Effect of wall corrugations on scalar transfer to a wavy falling liquid film. *J. Fluid Mech.*, pages 1098–1128, 2018.

[30] Keith E Herold, Reinhard Radermacher, and Sanford A Klein. *Absorption chillers and heat pumps*. CRC press, 2016.

[31] R. W. C. P. Verstappen and A. E. P. Veldman. Direct numerical simulation of turbulence at lower costs. *J. Eng. Math.*, (c):143–159, 1997.

[32] R. W. C. P. Verstappen and A. E. P. Veldman. Symmetry-preserving discretization of turbulent flow. *J. Comput. Phys.*, 187(1):343–368, 2003.

[33] D. Fuster. An energy preserving formulation for the simulation of multiphase turbulent flows. *J. Comput. Phys.*, 235:114–128, 2013.

[34] M. Magnini, B. Pulvirenti, and J. R. Thome. Characterization of the velocity fields generated by flow initialization in the CFD simulation of multiphase flows. *Appl. Math. Model.*, 40(15-16):6811–6830, 2016.

[35] N. Valle, F. X. Trias, and J. Castro. An energy-preserving level set method for multiphase flows. *J. Comput. Phys.*, 400:108991, 2020.

[36] Junseok Kim. A continuous surface tension force formulation for diffuse-interface models. *J. Comput. Phys.*, 204(2):784–804, 2005.

[37] David Jacqmin. Calculation of Two-Phase Navier–Stokes Flows Using Phase-Field Modeling. *J. Comput. Phys.*, 155(1):96–127, oct 1999.

[38] Didier Jamet, David Torres, and J U Brackbill. On the Theory and Computation of Surface Tension: The Elimination of Parasitic Currents through Energy Conservation in the Second-Gradient Method. *J. Comput. Phys.*, 182:262–276, 2002.

[39] D. Jamet and C. Misbah. Toward a thermodynamically consistent picture of the phase-field model of vesicles: Curvature energy. *Phys. Rev. E - Stat. Nonlinear, Soft Matter Phys.*, 78(3):1–8, 2008.

[40] Murray Rudman. A volume-tracking method for incompressible multifluid flows with large density variations. *Int. J. Numer. Methods Fluids*, 28(2):357–378, 1998.

[41] Mehdi Raessi and Heinz Pitsch. Consistent mass and momentum transport for simulating incompressible interfacial flows with large density ratios using the level set method. *Comput. Fluids*, 63:70–81, 2012.

[42] S Ghods and M Herrmann. A consistent rescaled momentum transport method for simulating large density ratio incompressible multiphase flows using level set methods. *Phys. Scr.*, T155:014050, 2013.

[43] Shahab Mirjalili and Ali Mani. Consistent, energy-conserving momentum transport for simulations of two-phase flows using the phase field equations. *J. Comput. Phys.*, 1:109918, 2020.

[44] Elin Olsson and Gunilla Kreiss. A conservative level set method for two phase flow. *J. Comput. Phys.*, 210(1):225–246, nov 2005.

[45] P. K. Sweby. High Resolution Schemes Using Flux Limiters for Hyperbolic Conservation Laws. *SIAM J. Numer. Anal.*, 21(5):995–1011, oct 1984.

[46] Ami Harten. On a Class of High Resolution Total-Variation-Stable Finite-Difference Schemes. *SIAM J. Numer. Anal.*, 21(1):1–23, feb 1984.

[47] Ronald P. Fedkiw, Tariq Aslam, Barry Merriman, and Stanley Osher. A Non-oscillatory Eulerian Approach to Interfaces in Multimaterial Flows (the Ghost Fluid Method). *J. Comput. Phys.*, 152(2):457–492, 1999.

[48] J.U Brackbill, D.B Kothe, and C Zemach. A continuum method for modeling surface tension. *J. Comput. Phys.*, 100(2):335–354, jun 1992.

[49] Denis Blackmore and Lu Ting. Surface Integral of its Mean Curvature Vector. *SIAM Rev.*, 27(4):569–572, 1985.

[50] Shahab Mirjalili and Ali Mani. Consistent, energy-conserving momentum transport for simulations of two-phase flows using the phase field equations. 2019.

[51] Theodore Frankel. *The Geometry of Physics*. Cambridge University Press, Cambridge, 3 edition, 2012.

[52] Jasper Kreeft. *Mimetic Spectral Element Method*. PhD thesis, Delft Technical University, 2013.

[53] R.R. Hiemstra, D Toshniwal, R.H.M. Huijsmans, and M.I. Gerritsma. High order geometric methods with exact conservation properties. *J. Comput. Phys.*, 257:1444–1471, jan 2014.

[54] Konstantin Lipnikov, Gianmarco Manzini, J. David Moulton, and Mikhail Shashkov. The mimetic finite difference method for elliptic and parabolic problems with a staggered discretization of diffusion coefficient. *J. Comput. Phys.*, 305:111–126, 2016.

[55] Francis H. Harlow and J. Eddie Welch. Numerical calculation of time-dependent viscous incompressible flow of fluid with free surface. *Phys. Fluids*, 8(12):2182–2189, 1965.

[56] N. Valle, X. Álvarez, F. X. Trias, J. Castro, and A. Oliva. Algebraic implementation of a flux limiter for heterogeneous computing. In *Tenth Int. Conf. Comput. Fluid Dyn.*, Barcelona, July, 2018.

[57] Alexandre Joel Chorin. Numerical solution of the Navier-Stokes equations. *Math. Comput.*, 22:745–762, 1968.

[58] J. Blair Perot. An Analysis of the Fractional Step Method. *J. Comput. Phys.*, 108(1):51–58, 1993.

[59] J. L. Guermond, P. Minev, and Jie Shen. An overview of projection methods for incompressible flows. *Comput. Methods Appl. Mech. Eng.*, 1(44-47):6011–6045, 2006.

[60] Termo Fluids S.L. http://www.termofluids.com/.

5

Conclusions

The dynamics of a vertical falling films has been captured by means of DNS. Special effort has been put to lay down a mathematical model and a computational setup which are physically consistent, robust, and stable; providing with reliable results.

A priory analysis of falling film have revealed an intense and interesting nonlinear behavior, producing intricate flow patterns which are relevant to many industrial applications. In particular, the role of capillary forces shaping the film interface also has consequences on the development of the flow pattern on the surface.

Spurred by such an industrially relevant, physically complex, mathematically unstable and computationally demanding case; and inspired by the rich experience of the ones that preceded us, we have succeeded at developing a new energy-preserving scheme that is numerically robust for all working conditions and computationally efficient. In this regard, the adoption of an algebraic approach has shown to provide with two synergistic effects: on the one hand, the adoption of an algebraic language has enabled the analysis and design of novel methods for the computation of surface tension and convection; on the other hand, the expression of the resulting scheme in algebraic terms has enabled its deployment into parallel and heterogeneous architectures.

During the development of the numerical techniques required for the physics-compatible simulation of multiphase flows, remarkable issues have been encountered that deserve further attention on future research.

The elliptic nature of the incompressible constrain in the Navier-Stokes equations results in the unavoidable need to solve a discrete Poisson equation. While this can, in principle, be done with arbitrary precision for any working conditions, in practice the use of an exact method becomes unaffordable when it comes to solve the discrete system of equations and thus the adoption of approximate solvers (e.g. Krylov methods) is customary.

Solver performance

In this regard, the presence of particularly high density ratios in the system $\mathsf{D}\mathsf{P}^{-1}\mathsf{G}\mathbf{p_c} = \mathsf{D}\mathbf{u_f}^{\star}$ result in an ill-conditioned system of equations, as the condition number grows with Π_ρ. For the Krylov-like solvers used in this work, this degrades its convergence properties severely, resulting in longer computational runs and, eventually,loss of quality of the solution. While a precondition strategy has tried to compensate for this situation by using $\mathsf{P_c}$ to precondition the system, the convergence rate of the solver has room for improvement. The addition of extra preconditioners may enhance the seed of the iterative method, while the overall computational cost must be assessed to ensure a net gain of this approach.

Numerical resilience

The approximate solution of the Poisson equation, implies that the divergence-free condition only holds approximately at the discrete level (i.e., $\mathsf{D}\mathbf{u_f} \approx 0$). This compromises most of the developments concerning mass, momentum and energy conservation, namely due to the transport and surface tension terms, as it was stated in chapters 2 and 4.

While single phase flow simulations can correct this inconsistency by imposing at the discrete level a skew-symmetric convective operator in the momentum equation, by removing the diagonal terms of $\mathsf{C}(u)$. However, the adoption of similar approach to multiphase flows require of additional variations which make it impractical.

First of all, the convective operator of the momentum equation for multiphase flows is already know to contain terms at the diagonal. This fact is actually exploited to come up with a solution that effectively preserve kinetic energy by matching this diagonal terms with the mass fluxes used to compute the mass conservation equation, the later being legitimately non divergence-free. The problem has moved then precisely to the mass conservation equation which, as it was mentioned before, is implicitly computed by means of the marker function transport equation. While we can enforce the divergence-free marker function convective operator, this collisions with the energy-preserving computation of curvature detailed in chapter 2 by breaking the $\mathsf{D}\mathsf{U}\Psi$ pattern for the high-resolution scheme used in $\mathsf{C}(\mathbf{u_f})$, by virtue of which we match $\Psi = -\mathsf{Y}^{\mathsf{T}}$.

High resolution schemes

The advection of sharp discontinuities boils down to the adoption of high resolution schemes, as has been discussed in chapter 3. While this is a classical problem in the numerical methods community, and despite the developments and tremendous

amount of research devoted to this topic, progress in the development of compact and arbitrarily compact schemes remain exiguous.

While the primary role of high resolution schemes is to transport sharp interfaces, which it is on its own a topic of interest for the numerical multiphase flow community; its secondary role is intimately related with the calculation of curvature, which is mathematically conceptualized by the First Variation of Area principle and implemented trough the adoption of the proper cell-to-face interpolation, as stated in chapter 2. In addition, chapter 2 shown as well that the adoption of numerical artifacts that sharpen interfaces by including additional terms, namely recompression, result in the artificial addition of surface energy if they do not match the $\mathsf{D}\mathsf{U}\Psi$ form, which leads us, again, to the high-resolution cell-to-face interpolation. Overall, this reasserts the interest in the design of high resolution schemes not only from the stability and boundedness perspectives, as it customary, but also from a wider, geometric-aware perspective.

Momentum conservation

The inclusion of surface tension in the simulation of multiphase flows is almost as essential as the simulation of the interface itself. As can be stated from the rich physics that rely on the capillary forces that have been reported in this and other works, its inclusion has a relevant impact on the system dynamics.

Owing to its inherently surface nature, capillary forces are conservative when acting on a closed surface, while boundaries should be included when they are not, giving rise to the appearance of contact angle effects. While this condition is flawlessly formulated in the continuum, preserve this property at the discrete level is way more challenging.

Despite all the effort put on the achievement of a detailed and accurate physics-compatible framework, the conservation of linear momentum in the surface tension term is actually elusive in this work. While this is usual for most diffuse interface models [1], particularly when adopting CSF methods [2], notable exceptions overcoming the CSF framework are motivated from the phase-field community [3], which we may see as an interesting variation of the CLS method. Nonetheless, the adoption of discrete models which are formally different from the continuous ones (i.e., removing curvature calculations) results into an interesting disquisition.

Closure

The deployment of massive supercomputers promise plenty of computational resources, but come along increased cost for the simulations carried over in such massive computers. This is a game changer on the way we look at multiphase flow simulations as, similarly to what the single phase turbulence community realized

years ago, the performance of more expensive simulations is accompanied by higher expectations about the reliability of the results. In this context, the development of techniques for the simulation of multiphase flows is slightly turning into the adoption of more physics-motivated techniques, which promise not only better stability and robustness, but also higher fidelity results.

As all development shifts, this clashes with the historic inertia of many numerical techniques which, just as we try do today, where suited to the computational resources at the time of its development. Nonetheless, far from an inconvenience, this must serve as a stimulating challenge and to enrich present development with pioneers experience, which must be acknowledged, studied, questioned and revisited once and again.

This work is rooted from a dual perspective. On the one hand, the research embraced the computational challenge from the very beginning and saw it as an opportunity to adopt a novel mathematical framework, which in turn boosted the development of new discretization schemes that lead to the tackling of stimulating industrial challenges. Conversely, the resolution of a technically relevant problem required of the adoption of a physics-compatible discretization, which in turn required of a robust mathematical framework, which resulted to be very favorable to the deployment of the resulting algorithm in massive supercomputers.

References

[1] Junseok Kim. A continuous surface tension force formulation for diffuse-interface models. *J. Comput. Phys.*, 204(2):784–804, 2005.

[2] J.U Brackbill, D.B Kothe, and C Zemach. A continuum method for modeling surface tension. *J. Comput. Phys.*, 100(2):335–354, jun 1992.

[3] Shahab Mirjalili and Ali Mani. Consistent, energy-conserving momentum transport for simulations of two-phase flows using the phase field equations. *J. Comput. Phys.*, 1:109918, 2020.

Appendix A

Inner products

Inner products are bilinear maps from a vector space to its base field (i.e., $(\cdot,\cdot)_{\mathsf{S}} : S \times S \to \mathbb{K}$). Inner products can be defined over both continuum and discrete spaces as

$$(f,g)_{\mathsf{S}} = \int_S fg dS \quad \forall f,g \in S \tag{A.1}$$

This definition can be readily applied to discrete fields, yielding the definition of inner products for discrete vectors within metric spaces as

$$(\mathbf{f_s},\mathbf{g_s})_{\mathsf{S}} = \mathbf{f_s}^T \mathsf{M}_{\mathsf{S}} \mathbf{g_s} \tag{A.2}$$

where M_{S} takes over the role of integrating in space, whereas the transpose of the first element provides with the appropriate order to perform the subsequent products and sums. This can be seen by expressing f and g as a finite sum of piecewise defined base functions.

Within this framework, we can define skew-symmetry as the property of operators satisfying

$$(\phi, A\psi) = -(A\phi,\psi) \quad \forall \phi,\psi \in S \quad A : S \to S \tag{A.3}$$

where, in the discrete setting, A must be a skew-symmetric matrix. Similarly, we can define duality as

$$(\phi, A\psi) = (A^*\phi,\psi) \quad \forall \phi \in S \psi \in T \quad A : T \to S \quad A^* : S \to T \tag{A.4}$$

By using the aforementioned definitions and the well-known Gauss-Ostrogradsky theorem, it provides with

$$(f, \nabla\cdot\vec{g}) = \int_\Omega f \nabla\cdot\vec{g} = -\int_\Omega \nabla f\cdot\vec{g} + \int_{\partial\Omega} f\vec{g}\cdot\hat{n} \tag{A.5}$$

where we can see that, assuming that there are no contributions from the boundary, the usual relation $(f,\nabla\cdot\vec{g}) = -(\nabla f,\vec{g})$ holds as usual. However, if there is a discontinuity in either f or $\vec{g}$ as a consequence of, say, an interface (Γ) in the domain, this

prevents us from using equation (A.5) directly, but rather first in both sub-domains separately and then sum them together. This results in an explicit expression as

$$(u, \nabla \cdot \vec{v}) = \int_{\Omega} u \nabla \cdot \vec{v} = \int_{\partial\Omega} u\vec{v} \cdot \hat{n} + \int_{\Gamma} [u\vec{v}] \cdot \hat{n} - \int_{\Omega} \nabla u \cdot \vec{v} \tag{A.6}$$

where the discontinuity is now explicitly included in the system. Note then that for a discrete system, the aforementioned gradient-divergence duality is

$$(\mathbf{u_s}, \mathsf{D}[s]v)_{\mathsf{S}} = -(\mathsf{G}\mathbf{u_s}, [s]v)_{\mathsf{S}} + \int_{\Gamma} [\mathbf{u_s}[s]v] \tag{A.7}$$

where the extra rightmost term captures the corresponding jump of the variables under consideration. Note that a proper approximation of Γ is required in order to obtain accurate solutions.

Appendix B

Modified Nusselt Flat Film scaling

The most elementary solution of falling films date back to Nusselt [1], who developed an analytic solution for laminar, steady, flat falling films by neglecting the accompanying phase inertia. This was used as the reference flow used to scale the Navier-Stokes equations and result into a dimensionless form. However, the inclusion of the gas phase under the same scaling is straightforward and provides insight into the role of density and viscosity ratios in the system.

The plan of the presentation is as follows: first a review of the Nusselt flat film solution is presented; subsequently, a new version considering both liquid and gaseous phases is developed.

Because for the original Nusselt solution we are only interested in the liquid phase, we depart from the incompressible Navier-Stokes equations for a single phase

$$\nabla \cdot \vec{u} = 0 \tag{B.1}$$

$$\rho \left(\frac{\partial \vec{u}}{\partial t} + (\vec{u} \cdot \nabla) \vec{u} \right) = -\nabla p + \mu \nabla^2 \vec{u} + \rho \vec{g} \tag{B.2}$$

$$[\sigma] \hat{\eta}_i = -\gamma \kappa \hat{\eta}_i \tag{B.3}$$

and assume a fully developed vertical (y component) laminar flow to yield

$$0 = \mu \nabla^2 u_y + \rho g_y \tag{B.4}$$

Under these assumptions, the velocity profile results in a semi-parabolic vertical velocity component which is a function of the wall-normal direction x only

$$u_y(x) = \frac{g_y}{2\nu} x \left(2h_N - x\right) \tag{B.5}$$

where h_N is the thickness of the film, also known as the Nusselt thickness. The integral of the velocity profile along such a film thickness provides with the average flat film velocity

$$u_N = \frac{1}{h_N}\int_0^{h_N} u_y(x)dx = \frac{g_y h_N^2}{3\nu} \tag{B.6}$$

Because the problem is ruled by an imbalance between viscous stresses and gravity acceleration, characteristic scales should consider them also. Hence can now introduce viscous-gravity scales, namely the viscous length

$$l_\nu = \left(\frac{\nu^2}{g}\right)^{1/3} \tag{B.7}$$

and viscous time scales

$$t_\nu = \left(\frac{\nu}{g^2}\right)^{1/3} \tag{B.8}$$

These allow to define the following reference values in order to obtain a non-dimensional version of equations (B.1) and (B.2)

$$\vec{x} = h_N\vec{X} \qquad t = t_\nu\frac{l_\nu}{h_N}\tau \qquad \vec{u} = \frac{h_N^2}{t_\nu l_\nu}\vec{U} \qquad p = \rho g h_N P \tag{B.9}$$

where capital letters are introduced to distinguish non-dimensional variables from its dimensional counterparts.

Introducing equations (B.9) into equations (B.1-B.3), we finally obtain:

$$\nabla\cdot\vec{U} = 0 \tag{B.10}$$

$$3Re\left(\frac{\partial\vec{U}}{\partial t} + \left(\vec{U}\cdot\nabla\right)\vec{U}\right) = -\nabla P + \nabla^2\vec{U} + \hat{g} \tag{B.11}$$

$$\left[-P\mathbb{I} + \nabla\vec{U}\right]\hat{\eta}_i = -We\kappa\hat{\eta}_i \tag{B.12}$$

Which is the typical dimensionless form used for falling films. Finally, we introduce the dimensionless density and viscosity of both liquid and gas phases, both referenced to the liquid properties

$$X_\rho = \frac{\rho}{\rho_l} \qquad X_\rho = \frac{\mu}{\mu_l} \tag{B.13}$$

which take the values $X_\rho = 1$ and $X_\mu = 1$ for the liquid phase and $X_\rho = \frac{\rho_g}{\rho_l} = \Pi_\rho$ and $X_\mu = \frac{\mu_g}{\mu_l} = \Pi_\mu$ for the gas phase, where Π_ρ and Π_μ are the gas/liquid density

and viscosity ratios, respectively. In this manner, we can modify the dimensionless momentum equation (B.11) to consider both gas and liquid phases

$$3Re\left(\frac{\partial\left(X_\rho\vec{U}\right)}{\partial t}+\nabla\cdot\left(X_\rho\vec{U}\otimes\vec{U}\right)\right)=\nabla\cdot\Sigma+X_\rho\hat{g} \tag{B.14}$$

subject to the definition of stress as

$$\Sigma=-P\mathbb{I}+X_\mu S \tag{B.15}$$

where S corresponds with the dimensionless form of the strain tensor. Note that due to the variability of X_μ, the usual Laplacian formulation of the viscous term can not be used. This induce a reformulation the jump conditions as

$$[\Sigma]\,\hat{\eta}_i=-We\kappa\hat{\eta}_i \tag{B.16}$$

for the same reason. Finally, the divergence (B.10) equation close the resulting system in terms of Re, We, Π_ρ and Π_μ.

References

[1] S. Kalliadasis, C. Ruyer-Quil, B. Scheid, and M. G. Velarde. *Falling Liquid Films*, volume 176. Springer, London, 2012.